

## INFORMATION TO USERS

This manuscript has been reproduced from the microfilm master. UMI films the text directly from the original or copy submitted. Thus, some thesis and dissertation copies are in typewriter face, while others may be from any type of computer printer.

**The quality of this reproduction is dependent upon the quality of the copy submitted.** Broken or indistinct print, colored or poor quality illustrations and photographs, print bleedthrough, substandard margins, and improper alignment can adversely affect reproduction.

In the unlikely event that the author did not send UMI a complete manuscript and there are missing pages, these will be noted. Also, if unauthorized copyright material had to be removed, a note will indicate the deletion.

Oversize materials (e.g., maps, drawings, charts) are reproduced by sectioning the original, beginning at the upper left-hand corner and continuing from left to right in equal sections with small overlaps. Each original is also photographed in one exposure and is included in reduced form at the back of the book.

Photographs included in the original manuscript have been reproduced xerographically in this copy. Higher quality 6" x 9" black and white photographic prints are available for any photographs or illustrations appearing in this copy for an additional charge. Contact UMI directly to order.

# UMI

A Bell & Howell Information Company  
300 North Zeeb Road, Ann Arbor MI 48106-1346 USA  
313/761-4700 800/521-0600



## **NOTE TO USERS**

**The original manuscript received by UMI contains pages with indistinct print. Pages were microfilmed as received.**

**This reproduction is the best copy available**

**UMI**



ISOSPIN EFFECT IN HEAVY-ION REACTIONS AT INTERMEDIATE  
ENERGIES

by

Lin-Bo Yang

A thesis submitted in partial fulfillment of the  
requirements for the Doctor of Philosophy  
degree in Physics in the  
Graduate College of The  
University of Iowa

May 1999

Thesis supervisor: Professor Edwin Norbeck

**UMI Number: 9933432**

---

**UMI Microform 9933432  
Copyright 1999, by UMI Company. All rights reserved.**

**This microform edition is protected against unauthorized  
copying under Title 17, United States Code.**

---

**UMI**  
300 North Zeeb Road  
Ann Arbor, MI 48103

Graduate College  
The University of Iowa  
Iowa City, Iowa

CERTIFICATE OF APPROVAL

---

PH.D. THESIS

---

This is to certify that the Ph.D. thesis of

Lin-Bo Yang

has been approved by the Examining Committee  
for the thesis requirement for the Doctor of  
Philosophy degree in Physics  
at the May 1999 graduation.

Thesis committee: E. Norbeck  
Thesis supervisor

Yasar Onel  
Member

James C. Eberhardt  
Member

Rob D. Merlino  
Member

M Hall Reis  
Member

## ACKNOWLEDGEMENTS

Upon attaining this goal of my doctorate degree, I must reflect back upon what brought me to this point. So I devote this space to acknowledge those who have made this reality, although these few words cannot possibly convey the proper gratitude for what has been given to me. The Lord God has been good to me, for I find myself in most fortunate circumstances. Even at times when I have failed to recognize this, I was always able to return. That the word “we” is used throughout the remainder of this manuscript is no mistake, rather it serves as a reminder of the collective contribution of the following people to achieve this end.

I do not know how to begin to express my gratitude to my wife and son, to whom this work is dedicated. Together we have overcome the many challenges to achieve this dream in the hope of a better life for our family. We wish to express our deepest heartfelt gratitude for the unconditional love and support given to us by our parents and our siblings.

I will always be deeply indebted to Prof. Edwin Norbeck for giving me the opportunity to become both a scientist and an engineer. It is Prof. Edwin Norbeck who gave me a chance to learn how to build complicated detector arrays. Prof. Norbeck has continued to stand by me through my graduate career. Had it not been for Prof. Norbeck, I would not have written the words upon this page and I would not even have had an opportunity to obtain a Ph.D. His ideas were the seeds that became this document, and every page bears his imprint. It was also Prof. Norbeck who encouraged me to gradually build up my strong background in computer science.

I am truly grateful for his unflagging support, his invaluable guidance and patience. Thank God for Prof. Edwin Norbeck.

Prof. Duane Ingram at Rock Valley College also gave me a lot of guidance and helped to build detectors and electronics. He also showed me how to pilot an airplane and how to enjoy life. I enjoyed working with him for several summers, as well as in test runs and real experiments in National Superconducting Cyclotron Laboratory (NSCL) at Michigan State University.

Eugene Ruth, Michael Fountain and Evan Clemmens in the machine shop of the Department of Physics and Astronomy at University of Iowa have also given me tremendous help in building our big nuclear detector array. They were always behind me whenever I had a mechanical problem with our Iowa Forward Array.

I would like to thank the members of the  $4\pi$  group at NSCL whose tenure coincided with my stint in the group. Thanks to those who have made the physics tape used in this thesis, Gary Westfall, Skip Vander Molen, Robert Pak, Nathan Stone, Omar Bjarki and Dan Megestro.

To the rest of the staff at NSCL, it has indeed been a pleasure working together with them. I never cease to be amazed at the help I have received from all departments at the lab to complete a project or experiment. In particular I must mention Dennis Swan and John Yurkon whose technical expertise made the design, fabrication and upgrade of the  $4\pi$  Array possible.

I am truly fortunate not only to count among my fellow graduate students, but also to be in the same research group as Yun-Wu Cheng. Yun-Wu has been the older brother I never had, and the friendship we have built together is best thing I take with me when I leave the nuclear lab at the University of Iowa. He is expert on C/C++, X window/Motif, Visual C++/MFC and Macintosh OS. It was he who made the

graphical interface for our BUU calculation available and it was he who made the PC graphical interface using Visual C++/MFC. I also thank him for encouraging me to convert everything in VAX/VMS to UNIX as early as possible. System Manager Scott Alandorf helped me to debug the VAX/VMS code so I could run the  $4\pi$  Array Fortran programs in our Dec Alpha/UNIX.

Finally, I'd like to thank my young son for reminding me what really matters in life. It is always my pleasure to show him and teach him about my hardware toys in my laboratory. Especially, it is fun to let him listen to the Wolf Howl in the Internet in my office while I am writing this thesis!

## TABLE OF CONTENTS

	Page
LIST OF TABLES . . . . .	vii
LIST OF FIGURES . . . . .	viii
CHAPTER	
1 INTRODUCTION . . . . .	1
2 FACILITIES AND EXPERIMENTS . . . . .	5
2.1 NSCL Cyclotron Facility . . . . .	5
2.2 The $4\pi$ Array . . . . .	7
2.2.1 Overview of $4\pi$ Array . . . . .	7
2.2.2 Ball Phoswiches . . . . .	9
2.2.3 Bragg Curve Counters . . . . .	10
2.2.4 Multiwire Proportional Counter (MWPC) . . . . .	12
2.2.5 High Rate Array (HRA) . . . . .	13
2.2.6 Maryland Forward Array . . . . .	15
2.2.7 Zero Degree Detector . . . . .	17
2.2.8 $4\pi$ Electronics . . . . .	18
2.2.9 $4\pi$ Vacuum and Gas Handling System . . . . .	20
2.2.10 $4\pi$ Data Acquisition System . . . . .	21
2.2.11 $4\pi$ Data Analysis and Physics Data . . . . .	22
2.3 Experiment and Data . . . . .	24
3 EVIDENCE OF ISOSPIN DEPENDENCE OF IMFS . . . . .	27
3.1 Introduction to Isospin Dependence of IMFs . . . . .	27
3.2 Evidence in $^{58}\text{Fe} (^{58}\text{Ni}) + ^{58}\text{Fe} (^{58}\text{Ni})$ . . . . .	28
3.3 Calculation of Impact Parameter . . . . .	29
3.4 Statistical Error . . . . .	31
4 ODD-EVEN ANOMALY . . . . .	32
4.1 Introduction to Odd-Even Effect . . . . .	32
4.2 Odd-Even Effect In Heavy-Ion Reactions . . . . .	33
4.3 Theoretical Calculations . . . . .	36
5 CONCLUSIONS . . . . .	39
6 FURTHER EXPERIMENTS WITH THE IOWA FORWARD ARRAY . . . . .	41
6.1 Discussion of Further Experiments . . . . .	41
6.2 Introduction to the Iowa Forward Array . . . . .	41
6.2.1 Silicon $\Delta E$ Detectors . . . . .	41

6.2.2	CsI(Tl) Scintillators and Photodiodes . . . . .	42
6.2.3	Preamplifiers . . . . .	43
6.2.4	Shaping Amplifiers . . . . .	45
6.2.5	Timing Circuits . . . . .	45
6.2.6	Pulser Array . . . . .	46
6.2.7	Silicon Detector Power Supply . . . . .	46
6.2.8	Supporting Frame . . . . .	47
6.2.9	Experiment Using the IFA . . . . .	47
REFERENCES	. . . . .	97

## LIST OF TABLES

Table		Page
1	Mean angles for the ball phoswiches. . . . .	48
2	Mean angles for the NSCL High Rate Array phoswiches. . . . .	49
3	Energy thresholds for the ball phoswiches. . . . .	50
4	Energy thresholds for the NSCL High Rate Array phoswiches. . . . .	50
5	Energy thresholds for the Iowa Forward Array. . . . .	51

## LIST OF FIGURES

Figure		Page
1	Map of the experimental facility in NSCL. . . . .	52
2	Mechanical drawing of the frame of the main $4\pi$ ball. . . . .	53
3	NSCL $4\pi$ Array. It consists of 20 regular hexagonal modules and 12 regular pentagonal modules. Each of the hexagonal (pentagonal) modules is instrumented with six (five) light particle detectors, one Bragg curve spectrometer, and one low pressure multiwire counter. . . . .	54
4	Side view of a hexagonal $4\pi$ ball module, revealing three independent layers of plastic and gas detectors. . . . .	55
5	Schematic drawing of a Bragg Curve Counter. Cutaways show the Frisch grid and field shaping grid. . . . .	56
6	Schematic diagram of the MSU $4\pi$ Bragg Curve Counter (BCC). . . . .	57
7	Exploded view of a hexagonal Multiwire Proportional Counter. . . . .	58
8	Arrangement of the High Rate Array detectors in the exit weldment of the ball. . . . .	59
9	The High Rate Array (HRA). . . . .	60
10	A typical two-dimensional histogram of the integrated signal in the fast ( $\Delta E$ ) plastic versus the integrated signal in slow (E) plastic for an HRA detector. . . . .	61
11	The Maryland Forward Array (MFA) as it attaches onto the frame of the HRA. . . . .	62
12	Assembly diagram of the ZDD, showing location of PMT's and light guides. The beam enters from the lower right. . . . .	63
13	Mechanical drawing of the ZDD chamber. Above: Top view, with beam entering from the top of the page. Below: Rear view, looking upstream. This also shows the goniometer, used for positioning of the detector. . . . .	64
14	The ball electronics. . . . .	65
15	The signals and the gates of the fast/slow plastic telescope. . . . .	66
16	Phoswich timing diagram. . . . .	67
17	Bragg curve gas system. . . . .	68
18	Front-end data acquisition system. . . . .	69
19	Average number of IMF's vs multiplicity in $^{58}\text{Fe} + ^{58}\text{Fe}$ and $^{58}\text{Ni} + ^{58}\text{Ni}$ at 75 A MeV. . . . .	70
20	Average number of IMF's vs charged particle multiplicity in $^{58}\text{Fe} + ^{58}\text{Fe}$ and $^{58}\text{Ni} + ^{58}\text{Ni}$ at 75 A MeV. . . . .	71
21	IMFs vs transverse energy for $^{58}\text{Fe} + ^{58}\text{Fe}$ and $^{58}\text{Ni} + ^{58}\text{Ni}$ at 75 A MeV. . . . .	72
22	Calculation of impact parameter $b$ from transverse energy spectrum. . . . .	73
23	Average number of IMF's vs impact parameter $b$ in $^{58}\text{Fe} + ^{58}\text{Fe}$ and $^{58}\text{Ni} + ^{58}\text{Ni}$ at 75 A MeV. . . . .	74

24	Average number of IMFs versus charged particle multiplicity in $^{58}\text{Fe} + ^{58}\text{Fe}$ and $^{58}\text{Ni} + ^{58}\text{Ni}$ at 45 A MeV with much lower statistics (130k events). . . . .	75
25	Average number of IMFs versus charged particle multiplicity in $^{58}\text{Fe} + ^{58}\text{Fe}$ and $^{58}\text{Ni} + ^{58}\text{Ni}$ at 75 A MeV with 130k events. . . . .	76
26	Average number of IMFs versus charged particle multiplicity in $^{58}\text{Fe} + ^{58}\text{Fe}$ and $^{58}\text{Ni} + ^{58}\text{Ni}$ at 105 A MeV with 130k events. . . . .	77
27	IMF energy spectra at $5.4^\circ$ for 75 A MeV $^{58}\text{Ni} + ^{58}\text{Ni}$ and $^{58}\text{Fe} + ^{58}\text{Fe}$ . Beam velocity fragments have energy 75 A MeV, shown by the dashed line. . . . .	78
28	Number of IMFs as a function of Z for $^{58}\text{Ni} + ^{58}\text{Ni}$ and $^{58}\text{Fe} + ^{58}\text{Fe}$ obtained by integrating the energy spectra starting at 30 A MeV (see Fig. 27). . . . .	79
29	Excess of even-Z over odd-Z fragments as a function of Z calculated from the data shown in Fig. 28. $\delta(Z)$ is defined in Eq. (4.1). . . . .	80
30	Yield ratios of beam-velocity fragments as a function of Z for 75 A MeV $^{58}\text{Ni} + ^{58}\text{Ni}$ and $^{58}\text{Fe} + ^{58}\text{Fe}$ . . . . .	81
31	Yield ratios as a function of Z for sources of $^{58}\text{Ni}$ and $^{58}\text{Fe}$ calculated for each of four classes of emitted fragments. . . . .	82
32	Excess of even-Z over odd-Z fragments as a function of Z shown by $\delta(Z)$ as defined in Eq. (4.1). Solid lines are full calculations, case 4). Dashed lines are for bound states only, case 3). . . . .	83
33	Odd-even effect at $^{58}\text{Ni} + ^{58}\text{Ni}$ and $^{58}\text{Fe} + ^{58}\text{Fe}$ for 45, 75, 105 A MeV. . . . .	84
34	Individual $\Delta E$ -E detector telescope. . . . .	85
35	Arrangement of the three rings, each consisting of 20 CsI(Tl) crystals. They are front, middle and rear rings of CsI(Tl) crystals. . . . .	86
36	Front ring and middle ring $\Delta E$ detectors. The arrangement of two, two-segment detectors in the mount for one side of the ring closest to the target is shown at the upper left. At the lower right, the outline of a four-segment detector for one side the middle ring is shown. The dark strip at the bottom of the detector is an extension of the guard ring structure which will be used to attach the detector to its mount. . . . .	87
37	Middle ring $\Delta E$ detectors showing wire connections. . . . .	88
38	Diagram of attachment between photodiode and CsI(Tl). More than 90% of backside area of CsI(Tl) is covered by the photodiode. . . . .	89
39	$^{241}\text{Am}$ $\alpha$ -particle spectra from CsI(Tl) with entrance windows of aluminized Mylar and aluminum leaf. Aluminum leaf gives better energy resolution. . . . .	90
40	Schematic of the preamplifier. . . . .	91
41	Schematic of the shaping amplifier. . . . .	92
42	Schematic of the test-pulser circuit . . . . .	93
43	Schematic of the linear current to voltage converter circuit used in the power supply. . . . .	94
44	Forward array supporting frame. The whole structure is made of aluminum. . . . .	95
45	Z-lines obtained from the experiment of $^{58}\text{Fe}(^{58}\text{Ni}) + ^{58}\text{Fe}(^{58}\text{Ni})$ from 5 MeV/nucleon to 105 MeV/nucleon in March 1998. Vertical axis is $\Delta E$ and horizontal axis is E. The figure shows some of the isotope resolution. The set of three curves near the middle is $^{7,9,10}\text{Be}$ . . . . .	96

## CHAPTER 1

### INTRODUCTION

In the past several years, isospin [1] dependences in heavy-ion reactions at intermediate energies have been focused on the studies of collective transverse flow [2], balance energy [3] and multifragment production [4, 5, 6, 7]. It was found that the more neutron-rich system exhibits larger flow values; the more neutron-rich system also exhibits higher balance energies at all measured impact parameters. These two conclusions are in agreement with the predictions of a Boltzmann-Uehling-Uhlenbeck (BUU) transport model [8, 9, 10, 11] that incorporates an isospin-dependent mean field and isospin-dependent nucleon-nucleon scattering cross sections.

However isospin dependences of multifragment production are not well understood. In particular, this is the first study of isospin dependences of the odd-even effects in heavy-ion reactions at intermediate energies.

Multifragment production from heavy-ion collisions at intermediate and high energies provides us with the means to investigate nuclear matter under conditions of energy and density far removed from the ground-state configuration. The phenomenon of multi-fragmentation wherein fragments with charge greater than  $Z = 3$  are emitted with large multiplicities from heavy-ion reactions has been the focus of many measurements [12]. Some of the central issues that surround the multi-fragmentation process are the attainment of thermal and chemical equilibrium of hot nuclear matter prior to the production of fragments, and the dynamics and time scales involved in the fragment emission process. A vast majority of the measurements in

this field have concentrated on the issue of the fragmentation dynamics and time scales, and on the question of thermal equilibration. With the advent of radioactive beam facilities, the influence of the isospin degree of freedom in heavy-ion collisions is being addressed [13]. The isospin degree of freedom thus becomes an important probe in the study of the dynamical aspects of the formation and decay of hot nuclear matter in heavy-ion collisions [14].

Previous measurements of multifragment production with isotopic resolution from very mass-asymmetric reactions of light ions on heavy targets of varying isotopic composition showed that the  $N/Z$  (number of neutrons/number of protons) ratio of the target is reflected in the  $N/Z$  composition of the intermediate mass fragments (IMFs) emitted in such reactions [15, 16, 17]. Such measurements were recently extended to less mass-asymmetric heavy-ion reactions [18]. In these measurements, a transition was observed in the emission of fragments, from a low energy regime where the  $N/Z$  degree of freedom was equilibrated prior to emission, to a higher energy regime where the  $N/Z$  degree of freedom was not equilibrated prior to emission.

A recent study of fragment emission in the reaction  $^{124,136}\text{Xe} + ^{112,124}\text{Sn}$  observed from the isospin composition of light charged particles that light fragments from a mid-velocity region were substantially more neutron rich when compared to fragments from the projectile velocity region [6]. It was suggested that the fragments were emitted from the rupture of neutron-rich neck-like structures formed in these heavy-ion reactions. Recent model calculations have demonstrated evidence for neutron-rich neck regions [19], and evidence for the dependence of the  $N/Z$  ratio of the neck region on the  $N/Z$  of the entrance channel [20].

On the theoretical front, much progress has been made in the development of models that treat the formation of hot nuclear matter in heavy-ion collisions in

a dynamical way. Model calculations based on the quantum molecular-dynamics (QMD) approach [21] and the BUU mean-field approach have been developed and utilized to describe the reaction dynamics in heavy-ion collisions at intermediate energies. Basically BUU model is a transport equation which includes the quantum mean field Time-Dependent Hartree-Fock (TDHF) approximation, two-body hard collisions, and Pauli blocking [22]. The BUU model is treated in a full microscopic description. The isospin term has been introduced into the BUU model by accounting for the difference in the nucleon-nucleon scattering cross section and in the nuclear potential [23]. These models take into account the dynamics in the collision phase of the reactions and these calculations are carried out to a certain time step in the reaction, resulting in a distribution of nucleons. A second stage of the calculation involves identifying excited clusters and free nucleons from this distribution, and subsequently the decay of the identified hot clusters to nuclear fragments based on the assumption of thermal and statistical equilibrium. The measurement of fragments with isotopic resolution from heavy-ion collisions should thus provide a sensitive tool for studying the validity of the assumptions made in the dynamical and statistical stages of these model calculations.

A different approach using percolation models has proven useful in the simulation of multifragment production [24, 25]. With these models, fragmentation is described by first distributing a set of points or sites, each representing a nucleon, on a three-dimensional lattice, which represents the bonds between the sites. More details about these models are given in Sec. 3.1.

In this work we present data on IMF production from the mass-symmetric reactions of  $^{58}\text{Fe} + ^{58}\text{Fe}$  and  $^{58}\text{Ni} + ^{58}\text{Ni}$  with isotopic resolution only for hydrogen. The only difference between the two reactions is that the ratio  $N/Z = 1.23$  for  $^{58}\text{Fe}$

+  $^{58}\text{Fe}$  while  $N/Z = 1.07$  for  $^{58}\text{Ni} + ^{58}\text{Ni}$ .

For these mass-symmetric reaction pairs we have observed the isospin dependence of IMF production as a function of charged particle multiplicity and impact parameter. Further study of the isospin dependence of IMF production shows that for beam velocity fragments at  $6^\circ$  with  $Z$  from 3 to 15 the more proton-rich Ni reaction produces more even- $Z$  IMFs than the Fe reaction. The ratio (number of IMFs from  $^{58}\text{Ni} + ^{58}\text{Ni}$ )/(number of IMFs from  $^{58}\text{Fe} + ^{58}\text{Fe}$ ) as a function of  $Z$  is about 10% larger for even  $Z$  values for  $Z = 3$  to 15.

In this thesis we first describe the facilities at the National Superconducting Cyclotron Laboratory (NSCL). The NSCL  $4\pi$  Array system is described in detail so the reader can understand how the two sets of data,  $^{58}\text{Ni} + ^{58}\text{Ni}$  and  $^{58}\text{Fe} + ^{58}\text{Fe}$ , were generated. This is also the first thesis which describes all of the  $4\pi$  detector arrays.

The Iowa Forward Array (IFA) is completed and has been used in one large experiment. This experiment also studies  $^{58}\text{Fe}$  and  $^{58}\text{Ni}$  beams on  $^{58}\text{Fe}$  and  $^{58}\text{Ni}$  targets. The differences are a larger energy range, 5 to 105 A MeV, and isotopic resolution up to  $Z = 8$  for laboratory polar angles ( $\theta_{lab}$ ) from  $3^\circ$  to  $18^\circ$ . The data analysis has been started but much work remains. After building the IFA the author regrets that he will not be available to finish the data analysis. That task can be the Ph.D thesis of another graduate student.

## CHAPTER 2

### FACILITIES AND EXPERIMENTS

#### 2.1 NSCL Cyclotron Facility

This chapter describes facilities and experiments at the National Superconducting Cyclotron Laboratory (NSCL) that were part of the research done for this thesis.

The NSCL is located on the campus of Michigan State University (MSU) in East Lansing, Michigan. The NSCL faculty and students are members of MSU's Department of Physics and Astronomy or Department of Chemistry. The NSCL is supported by the Division of Physics of the National Science Foundation's Directorate for Mathematical and Physical Sciences. The NSCL is a national user facility devoted primarily to basic nuclear science research and accelerator and instrumentation R&D, with a modest effort to support a broad program of applied and cross-disciplinary research.

In 1961, the National Science Foundation (NSF) funded construction of a 50 MeV cyclotron, which became the world's first high resolution isochronous cyclotron using new single-turn extraction techniques developed at MSU. In 1978, construction of the National Superconducting Cyclotron Laboratory (NSCL) as a national user facility was recommended by the NSF/DOE Nuclear Science Advisory Committee (NSAC). In 1982, the first beam was extracted from the K500, the world's first superconducting cyclotron, designed and constructed at the NSCL. The nuclear science program with the K500 was initiated with a modest array of equipment, largely

carried over from the K50, and was carried out without disrupting construction of the larger K1200 cyclotron. In 1988, the first beam was extracted from the K1200 cyclotron, and an interim research program was initiated with a 92 inch scattering chamber and a partially completed  $4\pi$  Array installed in series on a temporary beam line. Concurrently, the remaining superconducting beam transport system was completed. In October 1990, the full experimental program began, after an eight-month shutdown for the installation of the superconducting beam transport system and the A1200 beam analysis system. Since then, the reliability of K1200 operation has improved steadily to better than 90%, even while a large variety of beams and energies have been developed and extracted.

Since 1990 the K1200 cyclotron has provided the particle beams for all of the nuclear science research at the NSCL. This cyclotron can accelerate ions of any element. In 1995, 81 different beams were delivered for a total of 5115 hours of beam on target for the year. The beam energy can be selected within the range from 5 MeV/nucleon to 200 MeV/nucleon. The radio frequency (rf) system provides the accelerating potential; its frequency range is 9 MHz to 26.5 MHz. The magnet provides an azimuthally varying field whose average value at the extraction radius of 1 m is between 3 and 5 Tesla.

The useful beam intensity ranges from about  $10^{12}$  particles/sec down to approximately 10 particles/sec. The high intensity limit is from either external radiation limits or from heating of the electrostatic deflector in the extraction system. For many interesting ions the intensity is limited by the output of the ion source. The cyclotron usually accelerates single atoms, but it also works with molecules, e.g.  $\text{H}_2^+$  is accelerated to provide protons. The particles are fed continuously from the electron

cyclotron resonance (ECR) ion source to the center axis of the cyclotron and are delivered as a continuous beam from the accelerator. In cyclotron language, continuous means a beam pulse for each rf cycle. The beam pulses can be made shorter than 1.0 ns. As they leave the ion source the particles are accelerated by a DC voltage of 7 to 20 kV and are transported to the midplane of the cyclotron. They follow a spiral path inside as they gain energy from the rf system, making approximately 700 to 800 turns and traveling about 3 km.

The NSCL has received funding for an upgrade that will increase the intensity of beams and will also extend the maximum energy of heavy beams. For example, uranium would be available at 90 MeV/nucleon, while the limit with the present facility is about 25 MeV/nucleon. The K500 cyclotron will accelerate ions of lower charge state, and high intensity, to an energy (less than 20 MeV/nucleon) suitable for injection into the K1200. When injected into the K1200, the ions pass through a thin foil and lose many electrons, emerging with a charge that is 2.5 times larger. This combination of accelerators will increase the intensity by 100 to 1000 and will make possible research using rare radioactive beams.

Figure 1 shows the present experimental layout of the National Superconducting Cyclotron Laboratory (NSCL) along with the  $4\pi$  Array.

## 2.2 The $4\pi$ Array

### 2.2.1 Overview of $4\pi$ Array

For the past ten years the  $4\pi$  Array [26] has been one of the most active nuclear detector arrays in the world. The  $4\pi$  Array is designed to detect all charged particles emitted from intermediate energy nucleus-nucleus collisions. Using low pressure multiwire counters (MWPCs), Bragg curve counters (BCCs) and fast/slow plastic

scintillator telescopes (FS's), particles ranging from protons to fission fragments can be detected with nearly  $4\pi$  solid angle.

The geometry of the device is a truncated icosahedron consisting of 20 hexagonal faces and 12 pentagonal faces. Two of the pentagonal faces are used for entrance and exit of the beam. Figure 2 is mechanical drawing of the frame of the main  $4\pi$  ball. Each face is instrumented with one subarray consisting of six (five) FS's, one BCC, and one MWPC for each hexagonal (pentagonal) face. Each of the 170 fast-slow phoswiches is composed of a 3-mm thick fast plastic  $\Delta E$  detector and a 25-cm thick slow E detector. The forward five hexagonal BCC have been subdivided into six separate counters by separating the anode into six triangular sections. This geometry provides a total of 170 light-particle detectors, 55 intermediate-mass-fragment detectors, and 30 fission-fragment detectors. The modular construction allows one to use the Array as a topology filter for other detectors by simply removing one of the subarrays and replacing it with a specialized detector.

Three detector arrays that supplement the  $4\pi$  Array are available. (1) A 45-element High-Rate Forward Array has been installed in the exit pentagonal face. This array, like the ball, consists of a layer of fast plastic followed by a block of slow plastic. It is close-packed and covers the polar angles ( $\theta$ ) from 3 to  $18^\circ$ . (2) A 16-element detector (MFA or Maryland Forward Array) covering the polar angles from  $1.5$  to  $3.0^\circ$  is available. This detector consists of an annular silicon detector backed by fast-slow plastic detectors. (3) A 16-element fast-fast plastic detector covering the polar angles from  $0.5$  to  $1.5^\circ$  called the Zero Degree Detector, is also operational.

The  $4\pi$  Array is instrumented with a computer-controlled gas handling system for the 60 gas counters. In addition, fast programmable hardware triggering and secondary software triggering is provided. The data acquisition system consists of a

fast ECLine bus readout system capable of very high data rates. The data acquisition system's front-end has been upgraded to a 5-node transputer-based parallel processing system. This system can process data at rates up to 20 Kiloevents/sec or tape speeds (560 kbytes/sec) and filter data at real-time speeds.

The vacuum vessel holds a vacuum of  $2 \times 10^{-5}$  Torr. An arm that picks a target from an 8-holder external carousel, with the capability to transfer targets under vacuum, is provided. Figure 3 shows the relative size of  $4\pi$  Array.

### 2.2.2 Ball Phoswiches

The outermost detectors in the  $4\pi$  Array are a set of phoswich scintillators. These detectors will stop all but the most energetic light ions.

The 170 phoswich detectors of the ball are made up of a thin fast-plastic  $\Delta E$  detector (to measure the rate of energy loss), followed by a large slow-plastic E detector (to stop the charged particle and measure its total energy). The light output from both elements is recorded via a single photo-tube. The detectors are organized into 30 modules. Twenty of them are hexagons and 10 are pentagons. The phoswich detectors in the main ball are truncated triangular pyramids which are sub-divisions of either hexagons ( $60^\circ, 60^\circ, 60^\circ$ ) or pentagons ( $72^\circ, 54^\circ, 54^\circ$ ) The angular coverage ranges from  $18^\circ$  to  $162^\circ$  in  $\theta$  and  $360^\circ$  in  $\phi$ . The energy thresholds range from 17 MeV for protons to 593 MeV for oxygen. These thresholds are dependent on the Bragg curve gas pressure. The fast-plastic  $\Delta E$  detectors are made of BC412, thickness is 3 mm, rise time is 1 ns, decay time is 3.3 ns. The slow-plastic  $\Delta E$  detectors are made of BC444, thickness is 25 cm, rise time is 20 ns, decay time is 180 ns. Solid angles subtended by the ball phoswiches are  $6 \times 65.96$  (msr) for ball hexagons and  $5 \times 49.92$

(msr) for ball pentagons. When a charged particle impinges on the scintillator elements of the phoswiches, light is produced, which is collected by the PMT and turned into a current pulse. The fast and slow plastic have different decay times so that their individual contributions to this current pulse can be electronically separated. This is called the  $\Delta E$ -E method because the fast component of this signal is a measure of the energy loss in transmission through the thin fast plastic, while the slow component is a measure of the total energy deposited in the thick slow plastic. Figure 4 shows side view of a hexagonal  $4\pi$  ball module, revealing three independent layers of plastic and gas detectors. Table 1 shows the mean angles for the ball phoswiches.

### 2.2.3 Bragg Curve Counters

The Bragg Curve Counters (BCC) [27] are effectively ionization chambers mounted on the front of each of the 30 ball modules. The overall length of the counter is 15 cm and the entrance window for a hexagon module is 10 cm across from side to side. Because of the large dimensions, it is important to include radial field shaping strips on the inside surfaces of the walls. The walls are made from 6.4mm thick G10 fiberglass-epoxy laminate. The pressure window is a  $900 \mu\text{g}/\text{cm}^2$  Kapton foil. This is supported by a grid of wires, 0.024 inches in diameter and of approximately 1 cm spacing. The separation (drift space) between cathode and Frisch grid is 14 cm. The Frisch grid is made from  $12.5 \mu\text{m}$  gold-plated tungsten wires with 0.5 mm spacing. The back plane of the BCC is the front surface of the scintillator telescope, which lies 1 cm behind the Frisch grid.

An evaporated aluminum layer on the face of the plastic modules serves as an anode. The five modules at the most forward angle have their anodes subdivided into six elements. The Bragg curves have their electric field lines shaped to be parallel

with the particles trajectory. The anode is shielded from space charge effects with a Frisch grid. In this way, the range of particles which are stopped within the detector can be measured. The BCC takes advantage of the fact that the maximum specific ionization of a stopping ion is proportional to the atomic number of the particle. By measuring the maximum of the ionization process, one obtains the charge  $Z$  of the particle. The integral of the ionization is a measure of the energy  $E$ . The  $Z$  of an ion that stops in the BCC can also be determined from the time delay of the leading edge of the BCC signal.

The electrons liberated by the ionization drift to an anode which is shielded from induced charge by the Frisch grid. Since the electric field is parallel to the path of the particle, the charge is measured as a function of time, and thus the complete energy-loss distribution of the stopping ion may be obtained.

The BCCs are operated in one of two modes; either as an ion chamber and thus a  $\Delta E$  detector for particles that stop in the  $\Delta E$  plastic or in "Bragg" mode where the  $E$  and  $Z$  of stopping particles are detected. In the former case low pressure (150 torr) heavy freon ( $C_2F_6$  gas) is used for best results and in the latter high pressure (500 torr) P5 gas (95% argon, 5% methane) is used. The operating voltages for P5 gas are -1000V on the cathode and +120V on the anode. For  $C_2F_6$  gas, the cathode is run at -500V and the anode at +100 V. The voltages have a pronounced effect on the signal shape and therefore the ability to measure the  $Z$  of the ion. The Bragg peak signal from the anode is split and analyzed with separate amplifiers having short and long shaping times. The short shaping time (differentiation) gives a measure of the peak amplitude, while from the long shaping time (integration) one obtains the total energy.

Heavy ions with as little as 100 keV/nucleon will penetrate the BCC entrance

foil, but in order to give a usable signal, a good fraction of the Bragg peak must occur within the chamber. Thus the lower identification threshold is about 1 MeV/nucleon for heavy ions. Heavy ions in the range  $A = 20-30$  with energies above about 7 MeV/nucleon will “punch-through” the BCC into the backing scintillator. This, of course, is a function of the gas and the gas pressure. If the ions stop in the fast plastic, they may be identified by a plot of the energy lost in the BCC against the light output from the fast plastic (a  $\Delta E-E$  plot) Figure 5 shows schematic drawing of a Bragg Curve Counter. Cutaways show the Frisch grid and field shaping grid. Figure 6 shows schematic diagram of the MSU  $4\pi$  Bragg Curve Counter (BCC).

#### 2.2.4 Multiwire Proportional Counter (MWPC)

The Multiwire Proportional Counter (MWPC) is a low pressure gas detector which makes use of the double amplification process discovered by Breskin [28]. It is essentially a development of the Parallel Plate Avalanche Counter (PPAC) by placing a plane of anode wires between two cathode foils. Detectors of this type form the inner layer of the  $4\pi$  Array. They are mounted on the target side of the  $4\pi$  Bragg Curve Counters.

The total thickness of the counter is 1.6 cm. The distance from target to the center of the MWPC is 15 cm; the solid angle subtended is about 300 msr. The anode is a plane of gold plated tungsten wires, 12  $\mu\text{m}$  in diameter, in the center of the detector. The wire spacing is 1 mm. These wires are connected to the high voltage and provide the fast timing signal. The two cathodes are at ground potential and are located 3.2 mm on either side of the anode plane. Each cathode plane consists of a polypropylene foil stretched to about 75  $\mu\text{g}/\text{cm}^2$ . The cathode foils are coated with a resistive strip of Nichrome (Ni/Cr 80/20%). The Nichrome strip is

in turn coated with 5 mm-wide Al strips, perpendicular to the Nichrome strip. The resistance between the end contacts of the cathode foils is typically in the range of 4 to 10 k $\Omega$ . For the hexagonal MWPC's, the orientation of one striped cathode (say the  $X$ ) is 60° with respect to the second ( $Y$ ). From each cathode, the position is calculated by the data acquisition software with the charge division method; *viz.*  $X = L/(L + R)$  and  $Y = U/(U + D)$ , where  $L, R, U$  and  $D$  stand for the Left, Right, Up, and Down signals. Note that, because the stripes on the two foils are not perpendicular to each other, these pairs of signals do not give positions in Cartesian co-ordinates as the names may suggest. The pressure windows are 0.3 mil (7.6  $\mu\text{m}$ ) Kapton foils. The MWPC is designed to operate at 5 torr of isobutane. A typical anode operating voltage is 510 V. At 5 torr pressure, the breakdown voltage is about 530 V. The Z threshold of the MWPC's would be reduced by using iso-octane gas and a slightly higher anode voltage. Figure 7 shows exploded view of a hexagonal Multiwire Proportional Counter.

### 2.2.5 High Rate Array (HRA)

In 1993 the MSU  $4\pi$  Array was upgraded with the High Rate Array (HRA) [29]. The HRA is a close-packed configuration of 45 phoswich detectors spanning laboratory polar angles ( $\theta_{lab}$ ) from 3°-18°. The array has acceptable granularity, minimum dead area, high data rate capability (individual HRA detector count rates  $\approx$  25,000 events/sec) and excellent resistance to radiation damage. The HRA is to be utilized in experiments with high count rates, such as flow or coincidence runs, and is meant to be complementary to other high resolution forward arrays used in the  $4\pi$  Array that employ silicon detectors. Table 2 shows the mean angles for the NSCL High Rate Array phoswiches.

The HRA consists of three pentagonal rings of 10, 15, and 20 fast/slow plastic counters. A 45 detector design was chosen so that no additional electronics would be necessary, because the HRA replaced a forward array with this many detectors. The only investment was in scintillator plastic and the mechanical support structure. The individual detectors are fast/slow plastic counters which measure  $\Delta E$ ,  $E$  and time by the same technique presently used for the phoswiches in the rest of  $4\pi$  Array. The detectors are painted with an epoxy based paint pigmented with  $\text{TiO}_2$  to reduce cross talk and are glued together in five wedges of nine detectors, effectively minimizing dead area. The front of the array is covered with  $1.5 \mu\text{m}$  Mylar to increase light collection efficiency, and is positioned as close to the target as would allow a 2 inch diameter photo-tube to be optically coupled onto the back of each detector. Design and fabrication of the HRA was carried out entirely at NSCL. Simulated events were run through a software replica of the HRA to determine the positions and sizes of the 45 HRA elements that provide the optimal granularity for these generated events, and minimize the probability for double hits in each detector. The simulation results indicate that the overall design of 10-15-20 (numbers of scintillators counting from the ring closest to the beam axis) is least susceptible to double hits and therefore considered the most suitable for the energy range of interest in high rate experiments. The HRA subtends all solid angle between the the Maryland Forward Array and detectors of the main Ball resulting in about 90% geometric efficiency for the entire Array. The HRA provides charge resolution up to  $Z = 18$  and mass resolution for  $Z = 1$ . Figure 8 shows arrangement of the High Rate Array detectors in the exit weldment of the ball. Figure 9 shows an overview of High Rate Array (HRA). Figure 10 shows a typical two-dimensional histogram of the integrated signal in the fast ( $\Delta E$ ) plastic versus the integrated signal in slow ( $E$ ) plastic for an HRA detector. Table 3 shows

the energy thresholds for the ball phoswiches. Table 4 shows the energy thresholds for the NSCL High Rate Array phoswiches.

### 2.2.6 Maryland Forward Array

The Maryland Forward Array [30] is designed for the study of peripheral intermediate energy heavy-ion collisions. Its low angle converge provides for the detection of relatively heavy projectile-like fragments normally missed by the rest of the  $4\pi$  Array.

MFA consists of a segmented phoswich-silicon detector array covering laboratory polar angles ( $\theta_{lab}$ ) from  $1.5^\circ$  to  $3.0^\circ$  when used with the HRA. A ring shaped silicon strip detector (designs from Micron Semiconductor Limited) is the entrance detector for this array. The  $300 \mu\text{m}$  of silicon that is the active region of the detector is read on the ohmic side using sixteen segments, which provide an electronic pulse height proportional to the energy deposited in the silicon by an incident particle, as well as the azimuthal angle for the hit in  $22.5^\circ$  bins. The junction side is read by sixty-four concentric strips. The correlation of the pulse heights in the strips with those from the segments allows the additional assignment of the polar angles of the hits in  $\sim 0.9^\circ$  bins.

The silicon detector is positioned directly in front of the phoswich part of the MFA, which is divided azimuthally into sixteen optically decoupled fast/slow plastic detectors. The correlation of the pulse heights from the silicon detector and the fast plastic of the MFA phoswich detectors allow the measurement of the charge, kinetic energy, and angles of large and/or slowly moving fragments which may stop in the fast plastic, while the correlation of the fast and slow plastic gives similar information for generally lighter and faster particles. The plastic phoswich array

consists of 16 individual detectors. Each phoswich is made of a 1-mm thick fast-plastic scintillator (BC400) glued to a 10 cm thick slow-plastic scintillator (BC444) followed by a Hamamatsu R1924 photo-multiplier tube which is optically coupled to the scintillator through a light guide.

The silicon detector is fully depleted for a voltage drop across the detector of 22.5 V, for which the capacitance of the detector is  $\sim 117\text{pF/segment}$  or  $\sim 29\text{pF/strip}$ . Positive voltage is applied to each of the sixteen (ohmic side) segments in a daisy chain from a single voltage supply. The silicon detector is over-biased to a voltage of 30V during data collection to insure a good charge collection. At this voltage, the total leakage current is very stable at approximately  $55\ \mu\text{A}$ , or  $3.4\ \mu\text{A/segment}$ .

The signals from both sides of the silicon detector travel through about two meters ( $\sim 216\ \text{pF}$ ) of shielded ribbon cable to NSCL built preamps, which have a full scale for signals equivalent to energy depositions on the order of 10 GeV (about a factor of five larger than the energy deposited in the detector by 50 MeV/nucleon  $^{129}\text{Xe}$  nuclei). The energy resolution of the detector is compromised somewhat by the large capacitance of the signal cables relative to the detector capacitance. The preamps are mounted directly onto the  $4\pi$  Array back plate. The RC time constant of the preamps is  $100\ \mu\text{sec}$ , which allows maximum average count rates of approximately  $\sim 2\ \text{kHz}$ . During data collection, the particle rates per channel were limited to about 250 Hz. A PPAC with 16 segments to match the 16 segments of the MFA was made to be used in front of the MFA. It worked well with five torr of iso-octane gas, but it has not yet been used in an experiment. Figure 11 shows The Maryland Forward Array (MFA) as it attaches onto the frame of the HRA.

### 2.2.7 Zero Degree Detector

The Zero Degree Detector (ZDD) [31] is a part of the MSU  $4\pi$  Array, which covers the laboratory polar angles between  $0.56^\circ$  and  $1.55^\circ$ . It consists of two layers of fast scintillating plastic and can resolve fragment charges and energies via two methods. In the first, fragments which pass through the first thin layer are identified via  $\Delta E/E$  measurements. In the second, slower fragments which stop in the first layer can be identified via  $\Delta E/\text{Time-of-Flight (TOF)}$  measurements.

There were several motivations for building such a detector. The mere fact of its small-angle coverage is valuable for identifying projectile-like fragments, and there is also the increased angular coverage. More importantly, it is anticipated that the data from this detector will provide valuable information relating to the impact parameter of triggered events.

The ZDD has the following detector and signal processing features:

1. Fast scintillating plastic for both  $\Delta E$  and E layers
2. Separated read-out of both layers
3. Adiabatic light-guides for the  $\Delta E$  readout
4. High-speed photo-multiplier tubes (PMTs)
5. Negative high voltage bias for the PMT
6. Specialized high-power voltage dividers to drive the PMTs

First, the ZDD could not be made from fast and slow scintillating plastic, as is the majority of the  $4\pi$  Array. Typical slow-plastic light emission times are on the order of hundreds of nanoseconds. Both the  $\Delta E$  and E layers are made of equally fast scintillating plastic (NE 104,  $\tau = 1.9$  ns) to avoid the overlap of light signals from separate events. Second, once the choice is made to use  $\Delta E$  and E layers with equally fast plastic, the signals can not be resolved if they are read out through the

same PMT, as is done with a phoswich. Thus each layer was given a dedicated PMT, resulting in 16 PMTs for the eight-fold segmented array. Third, the light emitted from the  $\Delta E$  plastic must be collected from its edge, requiring an adiabatic light-guide to couple the thin plastic to the PMTs. Fourth, fast PMTs (XP2262B) were chosen for optimal signal transit time (31 ns) and minimal time spread (3.5 ns). Fifth, the PMTs were operated in the negative HV bias mode to avoid the capacitive coupling inherent in positive HV bias designs. And finally, specialized high-power voltage dividers were designed, prototyped, and constructed for these PMTs to allow processing of near 1 V output signals at a rate of up to 500 kHz.

A dedicated chamber was also designed for the ZDD, since there was insufficient space for an additional detector in the existing  $4\pi$  ball. This chamber was given the added feature that the ZDD could be moved inside the chamber without breaking vacuum, through the use of a goniometer.

Figure 12 is the assembly diagram of the ZDD, showing the location of the PMT's and light guides. The beam enters from the lower right. Figure 13 shows the mechanical drawing of the ZDD chamber. Above: Top view, with the beam entering from the top of the page. Below: Rear view, looking upstream. This also shows the goniometer used for positioning of the detector.

### 2.2.8 $4\pi$ Electronics

The data acquisition electronics is based on a modified version of the LeCroy ECLine electronics and is part of a permanent setup at NSCL. Because of this, the ADC/TDC hardware available for additional detectors is restricted to the following list. The advantages, however, are high data rates and minimal setup time. Following are some of the major electronics.

The LeCroy FERAs (Fast Encoding Readout ADC) are commercial current integrating ADCs produced by LeCroy (module 4300). Its advantages are its conversion speed ( $\sim 10 \mu\text{s}$ ), zero suppression, channel density (16) and fast read out mode (ECLine).

The SILENA 4418/v ADC is a commercial peak sensing ADC. Its advantages are its conversion speed ( $4 \mu\text{s}/\text{channel}$ ), zero suppression and fast read out mode (ECLine). Its disadvantages are that its channel density is only 8, it is expensive, it requires a  $1 \mu\text{s}$  rise-time and the fact that it triggers on the first peak it registers. Gating and clearing the SILENA is generally done via the ECLine command bus from a LeCroy Driver (LeCroy 4301).

The LeCroy FERET (Time-to-FERA converters, module 4303) is a commercial time to charge converter to supply time signals compatible with a FERA ADC. The module has 16 channels and can be operated in either common-start or common-stop mode.

The discriminators are primarily Phillips Scientific with some LeCroy 4413. Functionally the two types are the same. The purpose of the discriminators is to generate signals for timing, multiplicity and pattern logic. Each device in the  $4\pi$  detector is assigned a channel in the bank of discriminators.

The Octal Constant Fraction Discriminators (OCFDs) are commercial modules produced by EG&G. In the  $4\pi$  system, one OCFD is used for timing, another is used for the master trigger.

There are several possible ways of triggering the  $4\pi$  system. The experimenter has a choice of three standard phoswich triggering schemes, and these triggers are produced in a similar manner with discriminator outputs and summers:

1. "Ball" multiplicity,

2. "High Rate Array" multiplicity,
3. "System" multiplicity.

Having generated one of these triggering signals, a coincidence must be made with the live-time signal from the computer hardware. If the computer is busy handling previous events there will be no live-time signal and the event will be ignored. If the coincidence is made, a *Master.Live* signal is generated. This signal is fanned out many times. One output flags the computer to read the event, another goes to a scaler, others go to the individual gate generators that create the various gates for the banks of FERAs and SILENAs. Figure 14 shows the Ball Electronics. Figure 15 shows the signals and the gates of the fast/slow plastic telescope. Figure 16 shows the phoswich timing diagram.

#### 2.2.9 $4\pi$ Vacuum and Gas Handling System

A Pfeiffer combination roughing and turbo pump is used to evacuate the  $4\pi$  vacuum chamber. The pumps operate at the rate of 2000 liters per second and achieve pressures in the ball down to about  $8 \times 10^{-6}$  Torr. The controls for the pumps and valves are on the panel terminal in the experiment vault.

The gas handling system is composed of two parts; one is the ON/OFF valves for pressurizing, venting, etc., and the other part is for regulation of the pressure. The ON/OFF section is handled by a FERMI system digital output board through OPTO-22 I/O modules. The regulation is done at base level with a commercial system developed by MKS. This system is interfaced to the FERMI system, such that, in normal operation, the FERMI system is used to set the pressure through the MKS controllers which operate in "external" mode. In case of problems with the interface, the MKS system can be used stand-alone ("internal" mode) to set the

pressure directly.

The gas handling system is primarily for MWPC and BCC. Both the MWPC and the Bragg curve detectors have similar systems. Each detector has an in and an out valve with five detectors combined to make a subsystem. Each subsystem is independently controlled. Pressure control for each system is done via a commercial (MKS) unit with each unit controlled via an in-house control system. The individual valves are also controlled via the in-house system. Layered on top of these systems is software that allows the user to control individual valves or globally set the system or subsystems to particular configurations along with setting the pressures. The in-house system is networked which in turn allows for remote monitoring and control. Figure 17 shows the design of the gas handling system.

#### 2.2.10 $4\pi$ Data Acquisition System

The  $4\pi$  data acquisition system [32] consists of three major parts: frontend, data routing, data storage.

The frontend electronics are based on a multi-node transputer farm capable of real-time filtering and high data rates. Little or no software setup is required for an experiment. Currently data rates are restricted by the secondary storage devices (500-550 kbytes/sec) or event rates which are restricted to the ADC dead-time plus 180 n sec/data-word.

For data routing, by using the standard NSCL data routing system, data buffers can be routed to multiple sinks, usually workstations, for online analysis.

Data storage can be done with either 8mm tapes up to 500 kbytes/sec or TZ85 taping devices up to 550 kbytes/sec. There are plans to do the initial storage on large volume hard drives.

A VME based system is used for data acquisition. The system hardware consists of two Motorola 68020 CPUs for control and acquisition along with a CAMAC branch driver, an Ethernet interface and three ECLine interfaces. This configuration also allows for multiple CAMAC branches, CPUs, and multiple data destinations as required. A UNIX based SUN clone (with node name fourpi.nscl.msu.edu) as a host system is linked to a VME transputer board. The links are transputer links not Ethernet links. Run control must be run from the host but it does not have to be at the main console. The transputer code is down-loaded to the transputer from the host via link0 and all communications transact over this link to/from a host resident program call ISERVER. Data is transferred back via link1 to host based memory. There must be a program to receive this data which is generally TRANSRC. A routing program (ROUTER) is then started to send buffers to one or more consumers such as TAPE. Taping is done on the host. Note that buffers can be routed over Ethernet to other workstations for displays, etc. The major restriction to this speed are the long (30 meter) links ( $\approx$  kb/sec) and the tape drive. Figure 18 shows the front-end data acquisition system.

#### 2.2.11 $4\pi$ Data Analysis and Physics Data

Data analysis consists of two parts: on-line analysis and off-line analysis.

For on-line analysis, data can be viewed with either XSARA or PIPAW while the experiment is going so that experiment parameters can be adjusted and problems can be recognized and corrected. The histogramming program, XSARA, is a NSCL product and was developed to deal with the large number of parameters ( $\sim$ 500) to be read in the  $4\pi$  Array. XSARA was modified from its old version such that the zero-suppressed parameters from each event are stored in a list, and a loop over

parameters in this list is used to check conditions and increment histograms. In addition, the binning of histograms through a parameter list allows the possibility of multiply occurring parameters within a given event. This in turn leads to histograms that may be incremented multiple times within a given event. Recently PIPAW, a modified version of PAW, has been written by Gary Westfall and used in several experiments.

Off-line analysis is a huge amount of work! Due to the complexity of the detection system and the large number of individual devices, a highly structured routine must be used. This routine proceeds as follows: first, the raw data words which were written to tape during the experiment, are *sorted* and accumulated in spectra which are associated with the appropriate detectors; second, pattern recognition and determination of the conformal mapping operations necessary to *match* the observed spectra to a master template. This procedure is responsible for the gain matching of the individual detector responses to a calibrated particle identification template; third, conversion of the raw data tapes into reduced and translated tapes which contain values of *physics interest*; and finally, *checking* and verification to assure that no errors have been introduced. At the completion of these four steps, the raw data provided by the acquisition system will have been translated into new *physics tapes*. After having completed the reduction of the data and the creation of the new set of *physics tapes*, the data can be analyzed for the content of interest to the physics community.

The buffer structure (8192 bytes/buffer) of the physics tapes is as following:

/ Buffer Header / Event 1 / Event 2 / ... / Event N /

Buffer Header: The first 6 words of the buffer make up the header and contain the following information:

Word 1: Buffer Type: 1. Data Buffer 2. Begin-of-Run Buffer (which also contains data ) 3. End-of-Run Buffer (which also contains data)

Word 2: Run Buffer

Word 3: Physics Buffer sequence number

Word 4: Number of events contained in this buffer

Word 5: Position of the last word in the buffer

Word 6: A running total of the normalization information

The event structure is as following:

/ Event Header / Detector 1 / Detector 2 / ... / Detector N / Event Header:  
one word, the event multiplicity (number of detectors which fired)

Detector Structure: Each detector contains 6 data words:

Word 1:  $Z$ , the charge of the detected fragment

Word 2:  $A$ , the mass number of the detected fragment

Word 3:  $\theta$ , polar angle in degrees

Word 4:  $\phi$ , the azimuthal angle in degrees

Word 5:  $E$ , the particle's energy in MeV

Word 6:  $I$ , the detector ID number

It should be noted that all the physics tapes of the  $4\pi$  system have been written in VMS with Fortran (PHYTAP.FOR). The thesis author is the first person to write his own code in C so that data generated by the VMS operating system can be read in a Unix platform.

### 2.3 Experiment and Data

The University of Iowa was a primary collaborator in the experiment at the National Superconducting Cyclotron Laboratory (NSCL) that studied  $^{58}\text{Fe} + ^{58}\text{Fe}$

and  $^{58}\text{Ni} + ^{58}\text{Ni}$  at beam energies of 45, 55, 65, 75, 85, 95, 105 MeV/nucleon. The experiments were carried out using heavy-ion beams from the K1200 cyclotron. The  $^{58}\text{Fe}$  ( $^{58}\text{Ni}$ ) beams were focused directly onto  $^{58}\text{Fe}$  ( $^{58}\text{Ni}$ ) isotopically pure targets ( $\approx 5.0 \text{ mg/cm}^2$ ) thickness at the center of the  $4\pi$  Array. Beam intensities were approximately 100 pA. The experiment ran for more than one hundred hours. Event characterization was accomplished with the MSU  $4\pi$  Array comprised of the main ball and the High Rate Array (HRA).

Data were taken with a minimum bias trigger that required at least one hit in the HRA (HRA-1 data), and a more central trigger in which at least two hits in the main ball (Ball-2 data) were required.

Raw data were recorded and analyzed using standard NSCL  $4\pi$  routines as described before. The final output is *physics tapes*.

At the time we got the physics tapes, VAX/VMS was still available at Iowa, but VAX/VMS was on the verge of vanishing. We had a good DEC Alpha running Unix with several disk/tape drives. In order to analyze the physics tapes of  $^{58}\text{Fe} + ^{58}\text{Fe}$  and  $^{58}\text{Ni} + ^{58}\text{Ni}$  the author completely rewrote the analyzing code into a different language (C). There are many disadvantages running Fortran rather than C in Unix partly because C is a native language of Unix and widely available in Unix workstations without license restrictions. In addition, there are many more C people in the computer science community than Fortran people.

The thesis author has successfully written a C routine that can be used to analyze any MSU  $4\pi$  Array physics tapes while he was upgrading the  $4\pi$  Array hardware. The graphical program used is PGPLOT which is a free ware downloaded from California Institute of Technology.

After finishing building detectors, doing experiments, obtaining physics tapes,

and setting up analyzing tools, we are now ready to make physics discoveries.

## CHAPTER 3

### EVIDENCE OF ISOSPIN DEPENDENCE OF IMFS

#### 3.1 Introduction to Isospin Dependence of IMFs

Multi-fragmentation is defined as the simultaneous emission of three or more fragments with  $Z \geq 3$ . It has been known that hot nuclear systems formed in intermediate energy nucleus-nucleus collisions sometimes decay with the production of several intermediate mass fragments (IMFs) characterized by  $3 \leq Z_{imf} \leq 20$ . A near-universal correlation has previously been observed between the average number of emitted IMFs and the charged-particle multiplicity. The universality seen in these instances was interpreted as due to a decay mechanism, independent of the production of the decaying system.

Recently isospin dependence on the formation of intermediate mass fragments has been reported in which the scaling of the average number of emitted intermediate mass fragments and the charged particle multiplicity were examined. Recent experiments have also demonstrated an isospin dependence in nucleus-nucleus collisions [2, 3, 5, 6]. In particular, increasingly neutron-rich systems seem to show enhancements in the multifragment production [7].

Percolation models have proven successful in the simulation of multi-fragmentation reactions [24, 25]. In these models, fragmentation is described by first distributing a set of points or sites, each representing a nucleon on a three-dimensional lattice, which represents the bonds between the sites. In the case of a simple rectangular lattice,

each site is connected to six nearest neighbors, however, it has been shown that the model is to a large degree independent of the lattice structure [33]. In the second step, some lattice bonds are randomly broken with a probability that in non-isospin dependent percolation models is the only free parameter. The remaining connected clusters are identified with the fragments of the reaction, the bond-breaking probability with the excitation energy per nucleon [34].

The percolation models can be modified by including isospin degrees of freedom, i.e. the lattice is comprised of protons and neutrons instead of just nucleons. However, an attempt to simulate this observed enhancement by using a percolation model was unsuccessful [5].

One of the main discrepancies between the experimental results and the models is in  $\langle N_{imf} \rangle$  vs  $N_c$ , where  $\langle N_{imf} \rangle$  is the average number of emitted intermediate mass fragments, and  $N_c$  is the charged-particle multiplicity. The discrepancies found between the data and the percolation models indicate that effects outside of the percolation theory are important. The nuclear structure of the fragments as well as sequential feeding might play a role. The role of pre-equilibrium emission, which may not only effect the sorting axis but as well determines the N/Z composition of the fragmenting system, seems to be most important.

Below we present our data showing the isospin dependence in mass-symmetric reactions.

### 3.2 Evidence in $^{58}\text{Fe}$ ( $^{58}\text{Ni}$ ) + $^{58}\text{Fe}$ ( $^{58}\text{Ni}$ )

We have examined intermediate mass fragment (IMF) production in the heavy-ion reactions  $^{58}\text{Fe} + ^{58}\text{Fe}$  and  $^{58}\text{Ni} + ^{58}\text{Ni}$  at 45, 75, and 105 A MeV. The IMF production at  $E/A = 45, 75, \text{ and } 105$  MeV is found to depend on the isospin of the

reacting system. The IMF production is higher in the neutron-rich system only for lower multiplicity while it is higher in the proton-rich system for higher multiplicity. In other words, qualitatively speaking, the average IMF is higher in the neutron-rich system only for more peripheral collisions while it is higher in the proton-rich system for more central collisions.

We have also performed the BUU simulation with the interface written by Yun-Wu Cheng [22] and reported the result to the physics community. Some other group at NSCL is investigating this result by a modified percolation model. Figure 19 shows the average number of IMFs versus multiplicity (including neutron etc.) in  $^{58}\text{Fe} + ^{58}\text{Fe}$  and  $^{58}\text{Ni} + ^{58}\text{Ni}$  at 75 A MeV (The slow plastic has some efficiency for detecting neutrons). Figure 20 shows the average number of IMFs versus charged particle multiplicity in  $^{58}\text{Fe} + ^{58}\text{Fe}$  and  $^{58}\text{Ni} + ^{58}\text{Ni}$  at 75 A MeV.

### 3.3 Calculation of Impact Parameter

The impact parameter  $b$  of a nucleus-nucleus collision is classically defined by the distance between the straight line trajectories of the centers of the two nuclei before their interaction.

From straightforward geometrical considerations, theoretical models predict that the size of the dense nuclear-matter zone produced in heavy-ion collisions at intermediate energies depends strongly on the impact parameter. It is thus essential to sort out the collisions according to their centrality. The impact parameter, which characterizes the initial state, is not directly measurable; it is thus necessary to find an observable strongly correlated with it. A simple observable is the multiplicity of detected particles, which has been used extensively by many groups working in this field. Intranuclear cascade (INC) [35] calculations confirm the hypothesis of a strong

correlation between impact parameter and multiplicity of emitted participant nucleons. Nevertheless, this selection of centrality by means of the multiplicity gives only a qualitative ordering of the collisions according to their impact parameter.

Total transverse kinetic energy can also be used as a measure of the impact parameter. The total transverse kinetic energy of identified particles,  $E_t$  is defined as

$$E_t = \sum_i E_i \sin^2 \theta_i = \sum_i (p_i \sin \theta_i)^2 / 2m_i \quad (3.1)$$

It has been shown that impact parameter selection derived from the total charged particle multiplicity,  $N_c$ , and the total transverse energy  $E_t$  are similar, with some differences occurring at large impact parameters where fluctuations appear to become a limiting factor [36, 37, 38].

In our selection of impact parameter, we have used the total transverse energy. We first make a graph of the transverse energy spectrum for  $^{58}\text{Fe} + ^{58}\text{Fe}$  and  $^{58}\text{Ni} + ^{58}\text{Ni}$  at 75 A MeV. From conservation of particles or from intuition from classical mechanics we have

$$\left(\frac{b}{b_{max}}\right)^2 = \frac{A_t}{A_{max}} \quad (3.2)$$

where  $A_{max}$  total number of events under the whole spectrum.  $A_t$  is the total number of events greater than  $E_t$ .

$$b = b_{max} \times \sqrt{\frac{A_t}{A_{max}}} \quad (3.3)$$

The figures use  $b/b_{max}$  as the impact parameters. This can be converted to a length by using  $b_{max} = 9$  fm, the result given by our BUU code.

This gives the impact parameter  $b$  for any given event as a function of total transverse energy  $E_t$ . We set up a table so we can map transverse energy to impact parameter. For each event we assign an impact parameter though this method. Figure 21 shows IMFs vs transverse energy for  $^{58}\text{Fe} + ^{58}\text{Fe}$  and  $^{58}\text{Ni} + ^{58}\text{Ni}$  at 75 A

MeV. Figure 22 shows calculation of impact parameter  $b$  from the transverse energy spectrum. Figure 23 shows average number of IMFs versus impact parameter  $b$  in  $^{58}\text{Fe} + ^{58}\text{Fe}$  and  $^{58}\text{Ni} + ^{58}\text{Ni}$  at 75 A MeV.

### 3.4 Statistical Error

During the process of studying the isospin effect in heavy ion reactions we have analyzed the following data.

At 75 A MeV for each of the reactions  $^{58}\text{Fe} + ^{58}\text{Fe}$  and  $^{58}\text{Ni} + ^{58}\text{Ni}$ , we use 109988 buffers or about 13 million events. They are all events with a ball-2 trigger. At 45 A MeV and 105 A MeV we used 1099 buffers or about 130K events for each run. They are also ball-2 trigger. We have an additional run for 105 A MeV  $^{58}\text{Ni} + ^{58}\text{Ni}$  of the same size with an HRA-1 trigger.

From the graphical analysis we see that the average differences in the number of IMFs between  $^{58}\text{Fe} + ^{58}\text{Fe}$  and  $^{58}\text{Ni} + ^{58}\text{Ni}$  at 75 A MeV are about 10%. The same analysis with only 130k events still gives about 10% with a standard error  $\delta = 1/\sqrt{130000} \ll 1\%$ . The statistical errors are smaller than the symbols.

Figure 24 shows average number of IMFs vs charged particle multiplicity in  $^{58}\text{Fe} + ^{58}\text{Fe}$  and  $^{58}\text{Ni} + ^{58}\text{Ni}$  at 75 A MeV with much lower statistics (130k events). Figure 25 shows average number of IMFs vs charged particle multiplicity in  $^{58}\text{Fe} + ^{58}\text{Fe}$  and  $^{58}\text{Ni} + ^{58}\text{Ni}$  at 45 A MeV with 130k events. Figure 26 shows average number of IMFs vs charged particle multiplicity in  $^{58}\text{Fe} + ^{58}\text{Fe}$  and  $^{58}\text{Ni} + ^{58}\text{Ni}$  at 105 A MeV with 130k events.

From the figures we find the same conclusion even with smaller statistics. When we compared the graphs for 105 A MeV with the two different trigger mechanisms, we found that the type of trigger makes no significant difference.

## CHAPTER 4

### ODD-EVEN ANOMALY

#### 4.1 Introduction to Odd-Even Effect

When excited heavy nuclear systems break up, the yield of even- $Z$  products often exceeds the yield of the adjacent odd- $Z$  products. This odd-even effect is, however, not universal and is not well understood. We list here some of the situations in which the effect is seen and some in which it is not seen.

The odd-even effect has been observed in fission [39, 40], in low-energy heavy-ion reactions ( $^{35}\text{Cl} + ^{24}\text{Mg}$  at  $E/A = 8$  MeV) [41], and in the breakup of GeV/nucleon heavy projectiles [42, 43, 44, 45]. Zeitlin *et al.* [42] find an enhancement for even- $Z$  projectile-like fragments from 1.05 A GeV  $^{56}\text{Fe}$  on a variety of targets from hydrogen to lead. The magnitude of the effect does not depend on the target mass. Cummings *et al.* [43] and Webber *et al.* [44] report similar results. For some of the high energy studies the magnitude of the odd-even effect is found to be related to isospin. Knott *et al.* [45] find large odd-even effects for  $^{40}\text{Ca}$  on liquid hydrogen at  $E/A = 357$  to 763 MeV and similar large effects with  $T_z = 0$  beams of  $^{32}\text{S}$  and  $^{36}\text{Ar}$ . For the  $T_z = -2$  beams,  $^{40}\text{Ar}$  and  $^{52}\text{Cr}$ , the effect is smaller, about the same as Zeitlin *et al.* [42] found for  $T_z = -2$   $^{56}\text{Fe}$ . For  $T_z = -1$   $^{58}\text{Ni}$  the odd-even effect is intermediate when compared to  $T_z = 0$  and  $-2$  beams. Data by Yennello *et al.* [46] show the effect in the breakup of Ag by  $^3\text{He}$  at energies of 0.9 and 3.6 GeV for IMFs with  $Z = 3$  to 11. They find the excess of even- $Z$  values to increase with energy. Within the accuracy

of their data the odd-even effect is independent of the angle of the detector.

The odd-even effect is also found for  $^{58}\text{Fe} + ^{58}\text{Ni}$  at 30 A MeV for IMFs at  $11^\circ$  and the results compared with models [4]. No odd-even effect is seen at  $40^\circ$ . Al. Raduta and Ad. Raduta [47] fit  $^{40}\text{Ar} + ^{45}\text{Sc}$  at  $E/A = 35$  to 115 MeV with a statistical model that includes level densities and binding energies. Their calculations show a small, energy-independent odd-even effect. Their overall fit to the data is good, although the accuracy of the data [48] is not good enough to show an odd-even effect.

No odd-even effect is seen for  $^{40}\text{Ca} + ^{40}\text{Ca}$  at  $E/A = 35$  MeV [49] in either projectile-like fragments or intermediate-velocity fragments. This is surprising because  $^{40}\text{Ca}$  has  $T = 0$  and the energy is in the range for which a strong effect is seen in the mass 58 reactions. The effect is also not seen in the projectile fragmentation of  $^{129}\text{Xe}$  at 790 A MeV for  $Z$  values near 50 [50] or in central  $^{84}\text{Kr} + ^{197}\text{Au}$  collisions at  $E/A = 35$  to 400 MeV [51].

In our work we will show how the odd-even effect is influenced by the isospin difference between  $^{58}\text{Fe} + ^{58}\text{Fe}$  and  $^{58}\text{Ni} + ^{58}\text{Ni}$ .

## 4.2 Odd-Even Effect In Heavy-Ion Reactions

To explore more fully this odd-even effect and its possible relationship to isospin we have measured the yields of IMFs for two sets of reaction pairs  $^{58}\text{Fe} + ^{58}\text{Fe}$  and  $^{58}\text{Ni} + ^{58}\text{Ni}$ . These differ only in the values of the ratio  $N/Z$ , 1.23 for  $^{58}\text{Fe}$  and 1.07 for  $^{58}\text{Ni}$ . The experiment measures the final products from the decay of excited projectile fragments. We will show that these products exhibit an odd-even effect for both reactions, at a magnitude similar to that that found in reference [4]. In this work, however, we extend the study to a comparison of the ratio of the yields for the two  $N/Z$  systems. For each  $Z$  we measure the ratio of the yield of fragments from the

Ni projectile to the yield of fragments from the Fe projectile. These measurements provide new and interesting results.

Beams of  $^{58}\text{Ni}$  and  $^{58}\text{Fe}$  at  $E/A = 45, 75$  and  $105$  MeV from the K1200 cyclotron at the National Superconducting Cyclotron Laboratory were focused onto isotopically pure  $^{58}\text{Ni}$  and  $^{58}\text{Fe}$  targets at the center of the Michigan State University  $4\pi$  Array [52]. The  $4\pi$  Array measures charged particles over most of the sphere. For this analysis, data from the entire Array is used for determining impact parameters. The IMFs discussed here were measured in a ring of ten phoswich detectors that completely covered the laboratory angles from approximately  $3^\circ$  to  $8^\circ$  (centered at  $5.4^\circ$ ). The threshold energies of the detectors ranged from 100 MeV for Li to 1080 MeV for P ( $Z = 15$ ). Additional experimental detail is given in Ref. [53] which made use of the same data.

Figure 27 shows IMF energy spectra for  $Z = 3$  to  $9$  from an equal number ( $14 \times 10^6$ ) of Ni and Fe events for a beam energy of  $75 A$  MeV. To exclude most IMFs that are not spectator fragments the impact parameter is required to be between  $1/3$  to  $2/3$  of the maximum value. The impact parameter is assumed to be inversely correlated to the transverse energy of the light charged particles ( $Z = 1$  and  $2$ ). Leaving the IMFs out of the transverse energy calculation helps suppress autocorrelations. The kinetic energy spectra in figure 27 show peaks corresponding to velocities slightly less than the beam velocity—as is expected for spectator fragments. For  $Z = 10$  to  $15$  the spectra are similar to those for  $A = 7$  to  $9$ . The fluctuations for the smaller  $Z$  values are the result of aliasing in the conversion of fragment energy to  $E/A$ . The statistical uncertainties are smaller than the symbols. There are systematic errors caused by uncertainty in the  $Z$  separation for individual detectors.

The larger number of even- $Z$  fragments from  $^{58}\text{Ni} + ^{58}\text{Ni}$  can be seen in figure 27,

but the odd-even effect for both reactions and the larger effect for Ni is shown more clearly by summing the energy spectra, figure 28. To avoid uncertainties related to the low energy cutoff of the detectors, the sums are started at 30 A MeV.

The excess of even-Z IMFs can be quantified using a formula developed as part of similar studies of fission fragments. The quantity  $\delta$  in Eq. (1) [54, 39] is a measure of the local deviation from a Gaussian-like distribution for four consecutive Z values, the initial value and  $Z + 1$ ,  $Z + 2$  and  $Z + 3$ , centered at  $Z + \frac{3}{2}$ :

$$\delta(Z) = \frac{1}{8}(-1)^{Z+1} \{ \ln Y(Z+3) - \ln Y(Z) - 3 [\ln Y(Z+2) - \ln Y(Z+1)] \} \quad (4.1)$$

In this equation  $Y(Z)$  are the yields for particular values of Z (the points in figure 28). A positive  $\delta$  implies an excess of even-Z fragments relative to odd-Z fragments. The resulting  $\delta$  values are plotted in figure 29. This figure shows an excess of even-Z fragments for both Ni and Fe with a larger excess for Ni. The negative  $\delta$  for  $Z = 3$  is caused by the large cross section for making Li ( $Z = 3$ ) in the low energy part of the  $E/A = 30$  to 110 MeV range, see figure 27.

Figure 30 shows the ratio of the Ni points to the Fe points in figure 28. On average the yield from the Ni system is slightly greater than from the Fe system, but a striking, new odd-even effect appears here. These fluctuations here are quite uniform over the entire range  $Z = 3$  to 15. The irregularity at  $Z = 7$  and 13 may be due to small errors in separating the IMFs by Z. Uncertainties become magnified in such a differential view of the data, but the statistical uncertainties are still smaller than the symbols. In most experiments there is a systematic change in detector efficiency as a function of Z. This does not occur here for  $Z = 3$  to 15 because the entire peak in the energy spectra (see figure 27) is used.

The magnitude of the ratio of the odd-even effect is independent of beam energy from  $E/A = 45$  to 105 MeV. Figure 29, showing  $\delta$  vs Z, and figure 30 look about the

same if they are replotted with data from either 45 or 105 A MeV. This constancy occurs in spite of the fact that the number of IMFs per event and the steepness of the yield as a function of  $Z$  both increase with beam energy. The systematic uncertainties are larger at 45 and 105 A MeV. At 45 A MeV some of the spectator fragments have an energy below the threshold energy of the detector; at 105 MeV the  $Z$  resolution is less certain.

### 4.3 Theoretical Calculations

To examine a possible basis for the observed behavior, Prof. W.A. Friedman at the University of Wisconsin has performed a series of exploratory calculations for us using the Expanding-Evaporating Source (EES) model [55]. In this model, fragments are statistically emitted from an excited source which is allowed to expand under the opposing influences of thermal pressure and a restoring nuclear force. The rates of emission are determined by the properties of the emitted fragments and those of the source. These rates are provided by Weisskopf detailed-balance and are governed by the conditions of the source including entropy, energy, and density. The exact properties of the emitted fragments are included and the binding energy of the instantaneous source is characterized by a schematic liquid-drop description. The species to be emitted are provided by input files for each calculation. This flexibility of the model provides a means for testing the influences of different aspects of a reaction.

In general, the yields of a given isotope depend on two general properties, binding energies and statistical weights. To explore these aspects separately Friedman performed four separate classes of calculations, all for initial sources of  $^{58}\text{Ni}$  and  $^{58}\text{Fe}$  at initial excitation energies of 7.5 A MeV. These calculations differed only by the

fragments considered for emission with the following different cases studied: Case 1) included the bound ground states of isotopes up to  $Z = 9$ , with the artificial assumption that each has zero spin, and thus equal statistical weights. This case tests the influence of binding energy alone. Case 2) includes the bound ground states of the previous case but with the proper spins and hence different degeneracy factors. Case 3) includes the same species as the previous two, but also includes the bound excited states of each species. Including these provides a change in the effective statistical weight for each isotope. Finally, in case 4) (the most complete case) the low-lying known resonances are added for each of the isotopes in addition to the bound states. After the primary yield is calculated the particle unstable decays are taken into consideration in providing the final yields.

The results of the predictions of these calculations for the ratio of yields by  $Z$ , for initial sources of  $^{58}\text{Ni}$  relative to  $^{58}\text{Fe}$  are shown in figure 31. With increasing completeness the general yields for Ni and Fe are brought closer to equality. i.e., the magnitudes of the ratios decrease toward unity. The odd-even oscillations develop when the bound-state statistical weights are added, and persist with the inclusion of the unbound resonances.

In all of the calculations the isotope distributions for each  $Z$  are biased toward the lighter masses for Ni and toward the heavier masses for the Fe initial sources. This is expected from the differences in the  $N/Z$  ratios. Two consequences of this biasing are seen in two aspects of the calculated ratios. First, the Ni yields are biased toward proton rich isotopes which have a greater probability for charged-particle decay. Hence for  $Z = 3$  and  $Z = 4$  this feature provides a relative downward shift in the calculated ratios for case 4). Before the charged-particle decay the odd-even fluctuations continue to  $Z = 3$  and  $Z = 4$  in a manner similar to that seen for the

higher  $Z$  values.

Second, the neutron rich isotopes are numerous and readily populated. These provide substantial additional weight from neutron unstable resonances which do not alter the charge of the fragment. Thus the yield from the the neutron rich Fe is increased relative to the Ni. This brings down the general scale of the ratios toward unity but does not greatly change the even-odd fluctuations. Since the number of proton rich isotopes above the most stable isotope varies with  $Z$ , this decay feature, i.e., charged-particle versus neutron, may be related to the general odd-even effect in each case separately.

Finally, values of  $\delta(Z)$  were explored in the final two cases, 3) and 4). Here a surprising result was found as seen in figure 32. The values of  $\delta(Z)$  for the most complete calculations are similar to the experimental results shown in figure 29., i.e., Fe and Ni have positive  $\delta(Z)$  due to an enhancement of even- $Z$  over odd- $Z$  fragments, with Ni having the larger values. For the case including only the bound states, however, the values for  $\delta(Z)$  are negative, reflecting the relative enhancement of odd- $Z$  fragments (opposite to case 4)). This difference occurs despite the fact that the ratio of Ni yields to Fe yields for the two cases show a very similar odd-even effect. This observation suggests that the odd-even fluctuations in the ratio can be independent of the even-odd fluctuations in yields from a single type of source.

## CHAPTER 5

### CONCLUSIONS

Intermediate mass fragment (IMF) production is different for the reaction pair  $^{58}\text{Fe} + ^{58}\text{Fe}$  and  $^{58}\text{Ni} + ^{58}\text{Ni}$  for which the only difference is the ratio  $N/Z$ , 1.23 for Fe and 1.07 for Ni. The average IMF production is higher in the more neutron-rich system for lower multiplicity while it is higher in the more proton-rich system for higher multiplicity. In other words, average IMF production is higher in the more neutron-rich system for more peripheral collisions, those with larger impact parameter  $b$ , while the IMF production is higher in the proton-rich system for smaller impact parameters.

We have not only observed the odd-even effect in the yields of both sets of targets and projectiles, we have also found another odd-even effect in the ratio of the yields from the two different sources having different isospin,  $^{58}\text{Fe}+^{58}\text{Fe}$  and  $^{58}\text{Ni}+^{58}\text{Ni}$ . The ratio of the number of fragments from the Ni reaction to the number from the Fe reaction is about 10% larger for even- $Z$  fragments ( $Z = 3$  to 15). This 10% enhancement occurs for energies from 45 to 105 A MeV. The illustrative calculations suggest that this odd-even effect can be qualitatively explained in the context of statistical calculations. The results depend, however, on quite detailed aspects of the various emitted fragments, including the low energy density of bound and unbound states, their spin degeneracies, as well as simple systematic features of the binding energy. In addition, the results are affected by the detailed bias in mass for each  $Z$ , which is strongly influenced by the isospin of the source. There is some indication

that the difference in the number of charged-particle unstable and neutron-unstable isotopes may contribute to both odd-even effects and may permit the isospin of the source to influence these effects.

## CHAPTER 6

### FURTHER EXPERIMENTS WITH THE IOWA FORWARD ARRAY

#### 6.1 Discussion of Further Experiments

The study of isospin effects in nuclear reactions by examining the dependence of several physical observables on the isospin of the projectile and target nuclei could be furthered if the forward array had isotopic resolution for the IMFs. The Iowa Forward Array (IFA) has this capability. The development of the IFA was a major part of the author's graduate research. Here we show how the IFA is constructed.

#### 6.2 Introduction to the Iowa Forward Array

##### 6.2.1 Silicon $\Delta E$ Detectors

The  $\Delta E$  detectors in the IFA are  $300\mu\text{m}$  silicon diodes. All silicon  $\Delta E$  detectors are made from 100 mm diameter silicon wafers. Semiconductor Processing Inc. provided us with wafers that are of uniform thickness to within  $\pm 1.0\ \mu\text{m}$ . Such exceptional flatness is essential for good isotopic resolution. The remaining processes were performed by Detection Technology Inc. in Finland, based on our design. The silicon  $\Delta E$  detectors were designed to match the front ends of CsI(Tl) crystals.

The 60 silicon  $\Delta E$  detectors are combined into larger, segmented detectors with two segments for the front ring and four segments for the middle and rear rings. This allows a larger solid angle to be covered by the silicon by eliminating some of the dead area around the edges. The frames that hold the silicon are only along the outside

edge of the silicon.

There is a 50  $\mu\text{m}$  guard ring around the outside and between the segments. Leaving the guard ring floating dramatically reduces leakage current. The leakage current is about 100 nA on the average at room temperature (20°C) at 50 V. Cross talk between adjacent detectors is less than 1/10000.

The outputs of the  $\Delta E$  detectors are connected to preamplifiers by short (less than 8 cm) ribbon cables. A bias voltage of 45 V is applied to the silicon detectors so that they are totally depleted. The energy threshold is determined by the thickness of the 300 $\mu\text{m}$  silicon detectors.

Figure 34 shows the individual  $\Delta E$ -E detector telescopes. Figure 35 shows the arrangement of the three rings of 60 CsI(Tl) crystals, labeled as front, middle and rear. Figure 36 shows the front ring and middle ring  $\Delta E$  detectors. The arrangement of two, two-segment detectors in the mount for one side of the ring closest to the target is shown at the upper left. At the lower right, the outline of a four-segment detector for one side of the middle ring is shown. The dark strip at the bottom of the detector is an extension of the guard ring structure which is used to attach the detector to its mount. Figure 37 displays middle ring  $\Delta E$  detectors showing the wire connections. Table 5 shows the energy thresholds for the Iowa Forward Array.

### 6.2.2 CsI(Tl) Scintillators and Photodiodes

The E detectors are 6 cm long CsI(Tl) scintillating crystals with photodiode read-out. They are assembled into rugged rings with almost no dead area. The details of the design and construction is given in a publication [56] and an M.S. [57] thesis. A brief summary is given below.

The CsI(Tl) crystals were grown by Hilger Corp., in England. They were grown

in the direction that the particles pass through the crystal in order to get the best energy resolution. Before Hilger machined the crystals to the final shapes they sent them to us for inspection. We used an ultra violet lamp (360 nm) and a  $\gamma$ -ray source ( $^{137}\text{Cs}$ ) to test for homogeneity and overall efficiency.

We coated the long sides of the finished crystals with a special 0.05 mm thick uniform white epoxy layer. One layer of 0.7  $\mu\text{m}$  thick aluminum leaf (from a local art supply store) was put between adjacent crystals as they were cemented together into rings. The same type of aluminum leaf was used to provide a reflective layer on the target end of the rings. Air bubbles between the leaf and the  $\text{CsI}(\text{Tl})$  crystals were removed by suitable application of vacuum.

Instead of using silicon gel as reported in our paper [56], we now use the two part GE RTV-615 as the optical coupling material for better mechanical strength. To protect the silicon photodiodes against possible impurities in the RTV, they were spin-coated [58] with an acrylic conformal coating (Humiseal 1B12 from Chase Corporation). The curing time of GE RTV-615 at room temperature is several hours, and it also depends on the portion of hardener.

Figure 38 shows the photodiode attached to the  $\text{CsI}(\text{Tl})$ . More than 90% of the backside area of the  $\text{CsI}(\text{Tl})$  is covered by the photodiode. Figure 39 shows  $^{241}\text{Am}$   $\alpha$ -particle spectra from  $\text{CsI}(\text{Tl})$  with entrance windows of aluminized mylar and aluminum leaf. Aluminum leaf is thinner and gives better energy resolution.

### 6.2.3 Preamplifiers

The IFA preamplifiers are made primarily from a low noise chip by InterFET. Because of the special mechanical structure of the IFA, there is no suitable commercial preamplifier available. The preamplifier circuit must be custom made. We also need

excellent energy resolution and a large dynamic range.

We met these needs by developing a high performance preamplifier that is compact and cost only \$30 dollars per channel. It is a modified version suggested by Interfet Corporation in 1994. Figure 40 shows the schematic of the preamplifier.

The preamplifier uses the IPA3A(B) preamp chip of Interfet, supplemented by Elantec EL2001 700MHz buffer amplifier, calibration network, and biasing resistor. To minimize noise, the length of the connection from the photodiodes and the  $\Delta E$  silicon diodes to the preamplifier board is limited to 15 cm. The connection is made by twisted pairs using 0.100 inch 2 pin connectors. Output signals from the preamps are transmitted using 20 meter long coaxial cables. Similar cables carry pulser signals to the preamplifier boards in order to perform calibration and cross-talk measurements.

In the diagram, resistor  $R_2$  is chosen to provide sufficient biasing current (12mA-15mA) through the  $V_{dd}$  input of the preamplifier. The value of resistor  $R_6$  determines the swing of the output voltage and should be in the range  $2k\Omega - 5k\Omega$  for negative swing and  $0.5k\Omega-1.2k\Omega$  for positive swing. The 3mA current source  $I_1$  is used to provide stable DC current through Open Source Output (OSO) of the integrated preamplifier. The capacitor and resistor in the feedback  $R_5C_4$  circuit of the preamplifier determine the time constant and the gain of the circuit. The gain is inversely proportional to the capacitance  $C_4$ . For a gain of 10mV/MeV, the calculated value of the feedback capacitor is about 4pF with 3.66 eV needed to produce one electron-hole pair.

To minimize noise it is desirable to have the value of the resistor  $R_5$  as high as possible, but too large a value can limit the counting rate.  $R_5$  also provides DC coupling between the output and input stages to prevent DC voltage drift. The practical value of the resistor  $R_5$  is in the range of 10 M $\Omega$  to 100 M $\Omega$ . To reduce

crosstalk via DC power supply lines, all amplifier channels are decoupled from the power supply by RC circuits.

A solid ground plane on the opposite side of the board is used to reduce the crosstalk even further. Indeed the measured crosstalk between channels on the same preamplifier board is about 1/10000.

Because the preamplifiers are in vacuum, care must be taken to select cables that will not damage the vacuum system. Some cables contain plasticizer with a high vapor pressure.

#### 6.2.4 Shaping Amplifiers

The shaping amplifiers for the IFA are made primarily of several fast operational amplifiers, AD847JN. Figure 41 shows the schematic of the shaping amplifiers. Although the shaping amplifiers are of a standard design, the values of the components are based on intensive computer simulation and calculation. Pulse shaping is achieved by passing the signal through a sequence of filters designed to provide the desired transfer function. The basic filter designs are CR and RC circuits which behave as high and low pass filters respectively. The CR and RC time constants are chosen to be the same in order to optimize the signal to noise ratio [59, 60].

On one shaper board there are two shaping amplifiers with time constants of  $2\mu\text{s}$  and  $1.3\mu\text{s}$  respectively. This allows charged particle identification by comparing the height and tail of the pulses.

#### 6.2.5 Timing Circuits

The timing units signal from the shaper amplifiers are made of two fast bipolar transistors with positive feedback [59]. The fast NPN transistors, BFR90, are made by Motorola. The bottom part of figure 41 shows a schematic of the timing circuit.

The value of the feedback resistor plays a critical role in the behavior of the circuit. In the circuit it is 15.2 k $\Omega$ . It is an extremely sensitive circuit. Although some software simulation packages show that a tiny input will generate a huge output, the circuit does not actually trigger on noise. In fact, the circuit works very well. When the input signal is small, the output is proportional to the input with a rise time of about 100ns. With large inputs the circuit saturates.

### 6.2.6 Pulser Array

A simple circuit was made to distribute eight test-pulse signals to the 120 preamps. Each test signal is fanned out to a particular preamp on each of the 15 sides (three rings, each with five sides). This arrangement allows the pulser signals to be used to check for crosstalk between preamps on the same circuit board. The circuit consists of an 8 $\times$ 15 array of NPN emitter followers (MPS918 made by Motorola). Figure 42 shows the schematic of the test-pulser circuit.

### 6.2.7 Silicon Detector Power Supply

If money were unlimited we would use a computer controlled power supply with 120 modules. It is not desirable to connect many silicon diodes in parallel with no means of knowing if one of them has developed a large leakage current. Our compromise between these two extremes is a circuit that takes the voltages from a small number of commercial power supplies and distributes them as needed to the 120 diodes. The circuit also prepares a graph of leakage current versus detector number that can be continuously displayed on an oscilloscope or a computer. The cost of the circuit is only about ten US dollars per channel. Essentially it consists of current-to-voltage converters, multiplexing units, and a low-frequency TTL clock. Figure 43 shows the circuit diagram for one of the 120 channels of the current to

voltage converter unit. More details of the circuit will be given in a forthcoming publication.

### 6.2.8 Supporting Frame

Figure 44 shows the aluminum frame that supports the IFA. Because of the large number of unusual angles made necessary by the pentagonal cone available for the IFA in the  $4\pi$  Array, conventional machining of the parts would have been prohibitively expensive. It was machined for a reasonable cost on a computer-controlled milling machine. The supporting frame was carefully assembled and properly aligned. It fits the pentagonal cone of the  $4\pi$  Array very well.

### 6.2.9 Experiment Using the IFA

The IFA has been used in a major experiment (96012) at NSCL. The primary goal of the experiment is to use isotope ratios to measure nuclear temperature. The 200 hour long experiment in March 1998 used beams of  $^{58}\text{Fe}$  and  $^{58}\text{Ni}$  at energies from 5 to 105 A MeV on targets of  $^{58}\text{Fe}$  and  $^{58}\text{Ni}$ . During the experiment all IFA detectors and electronics performed reliably. Figure 46 shows Z-lines obtained from one of the detectors. Vertical axis is  $\Delta E$  and horizontal axis is E. The figure shows some of the isotope resolution with a gap for the non-existent  $^8\text{Be}$ . The set of three curves near the middle is  $^{7,9,10}\text{Be}$ . The detector gave isotope resolution up to oxygen.

This experiment provided excellent data, but its analysis is beyond the scope of this thesis.

Module	A		B		C		D		E		F	
	$\theta$	$\phi$										
1	23.1	342.0	32.3	5.6	46.0	356.3	51.7	342.0	46.0	324.7	32.3	318.4
2	23.1	270.0	32.3	293.6	46.0	287.3	51.7	270.0	46.0	252.7	32.3	246.4
3	23.1	198.0	32.3	221.6	46.0	215.3	51.7	198.0	46.0	180.7	32.3	174.4
4	23.1	126.0	32.3	149.0	46.0	143.3	51.7	126.0	46.0	108.7	32.3	102.4
5	23.1	54.0	32.3	77.0	46.0	71.3	51.7	54.0	46.0	36.7	32.3	30.4
6	54.7	288.0	54.7	314.0	67.3	317.5	74.6	306.0	67.3	294.5		
7	54.7	226.0	54.7	242.0	67.3	245.5	74.6	234.0	67.3	222.5		
8	54.7	154.0	54.7	170.0	67.3	173.5	74.6	162.0	67.3	150.5		
9	54.7	82.0	54.7	98.0	67.3	101.5	74.6	90.0	67.3	78.5		
10	54.7	10.0	54.7	26.0	67.3	29.5	74.6	18.0	67.3	6.5		
11	64.9	342.0	72.4	355.0	86.5	354.4	93.5	342.0	86.5	329.6	72.4	320.0
12	64.9	270.0	72.4	283.0	86.5	282.4	93.5	270.0	86.5	257.6	72.4	257.0
13	64.9	198.0	72.4	211.0	86.5	210.4	93.5	198.0	86.5	185.6	72.4	185.0
14	64.9	126.0	72.4	139.0	86.5	138.4	93.5	126.0	86.5	113.6	72.4	113.0
15	64.9	54.0	72.4	67.0	86.5	66.4	93.5	54.0	86.5	41.6	72.4	41.0
16	86.5	306.0	93.5	318.4	107.6	319.0	115.1	306.0	107.6	293.0	93.5	293.6
17	86.5	234.0	93.5	246.4	107.6	247.0	115.1	234.0	107.6	221.0	93.5	221.6
18	86.5	162.0	93.5	174.4	107.6	175.0	115.1	162.0	107.6	149.0	93.5	149.6
19	86.5	90.0	93.5	102.4	107.6	103.0	115.1	90.0	107.6	77.0	93.5	77.6
20	86.5	18.0	93.5	30.4	107.6	31.0	115.1	18.0	107.6	5.0	93.5	5.6
21	105.4	342.0	112.7	353.5	125.3	350.0	125.3	334.0	112.7	330.5		
22	105.4	270.0	112.7	281.5	125.3	278.0	125.3	262.0	112.7	258.5		
23	105.4	198.0	112.7	209.5	125.3	206.0	125.3	190.0	112.7	186.5		
24	105.4	126.0	112.7	137.5	125.3	134.0	125.3	118.0	112.7	114.5		
25	105.4	54.0	112.7	65.5	125.3	62.0	125.3	46.0	112.7	42.5		
26	128.3	306.0	134.0	323.3	147.7	329.6	156.9	306.0	147.7	282.4	134.0	288.7
27	128.3	234.0	134.0	251.3	147.7	257.6	156.9	234.0	147.7	210.4	134.0	216.7
28	128.3	162.0	134.0	179.3	147.7	185.6	156.9	162.0	147.7	138.4	134.0	144.7
29	128.3	90.0	134.0	107.3	147.7	113.6	156.9	90.0	147.7	66.4	134.0	72.7
30	128.3	18.0	134.0	35.3	147.7	41.6	156.9	18.0	147.7	354.4	134.0	0.7

Table 1: Mean angles for the ball phoswiches.

Detector	$\theta$	$\phi$	Detector	$\theta$	$\phi$	Detector	$\theta$	$\phi$
1	5.4	0.0	16	10.6	246.0	31	14.3	279.0
2	5.4	324.0	17	10.6	222.0	32	14.3	261.0
3	5.4	288.0	18	9.6	198.0	33	15.9	243.0
4	5.4	252.0	19	10.6	174.0	34	15.9	225.0
5	5.4	216.0	20	10.6	150.0	35	14.3	207.0
6	5.4	180.0	21	9.6	126.0	36	14.3	189.0
7	5.4	144.0	22	10.6	102.0	37	15.9	171.0
8	5.4	108.0	23	10.6	78.0	38	15.9	153.0
9	5.4	72.0	24	9.6	54.0	39	14.3	135.0
10	5.4	36.0	25	10.6	30.0	40	14.3	117.0
11	10.6	6.0	26	15.9	9.0	41	15.9	99.0
12	9.6	342.0	27	14.3	351.0	42	15.9	81.0
13	10.6	318.0	28	14.3	333.0	43	14.3	63.0
14	10.6	294.0	29	15.9	315.0	44	14.3	45.0
15	9.6	270.0	30	15.9	297.0	45	15.9	27.0

Table 2: Mean angles for the NSCL High Rate Array phoswiches.

Particle Type	Punch-in Energy (MeV)	Particle Type	Punch-in Energy (MeV)
p	17	Be	214
d	24	B	300
t	28	C	380
He	70	N	483
Li	140	O	593

Table 3: Energy thresholds for the ball phoswiches.

Particle Type	Punch-in Energy (MeV)	Particle Type	Punch-in Energy (MeV)	Particle Type	Punch-in Energy (MeV)
p	13	C	269	Al	877
d	17	N	341	Si	962
t	20	O	419	P	1079
He	50	F	515	S	1170
Li	99	Ne	591	Cl	1294
Be	152	Na	687	Ar	1455
B	212	Mg	767		

Table 4: Energy thresholds for the NSCL High Rate Array phoswiches.

particle Type	Punch-in Energy(MeV)	particle Type	Punch-in Energy(MeV)	particle Type	Punch-in Energy(MeV)
p	6	C	132	Al	428
d	8	N	166	Si	470
t	9.5	O	204	P	526
He	24	F	248	S	571
Li	47	Ne	285	Cl	629
Be	73	Na	334	Ar	702
B	104	Mg	375	K	736

Table 5: Energy thresholds for the Iowa Forward Array.

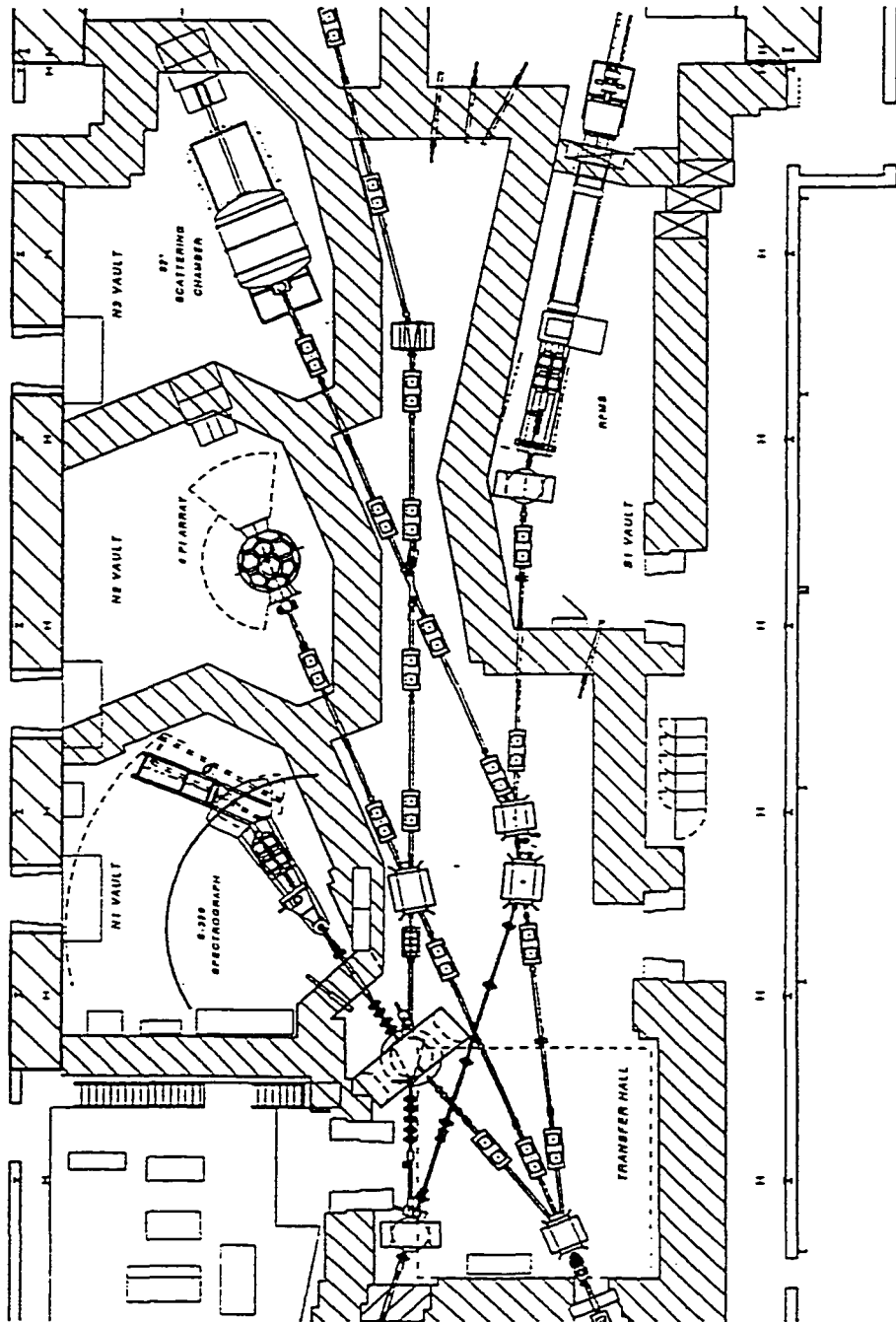


Figure 1: Map of the experimental facility in NSCL.

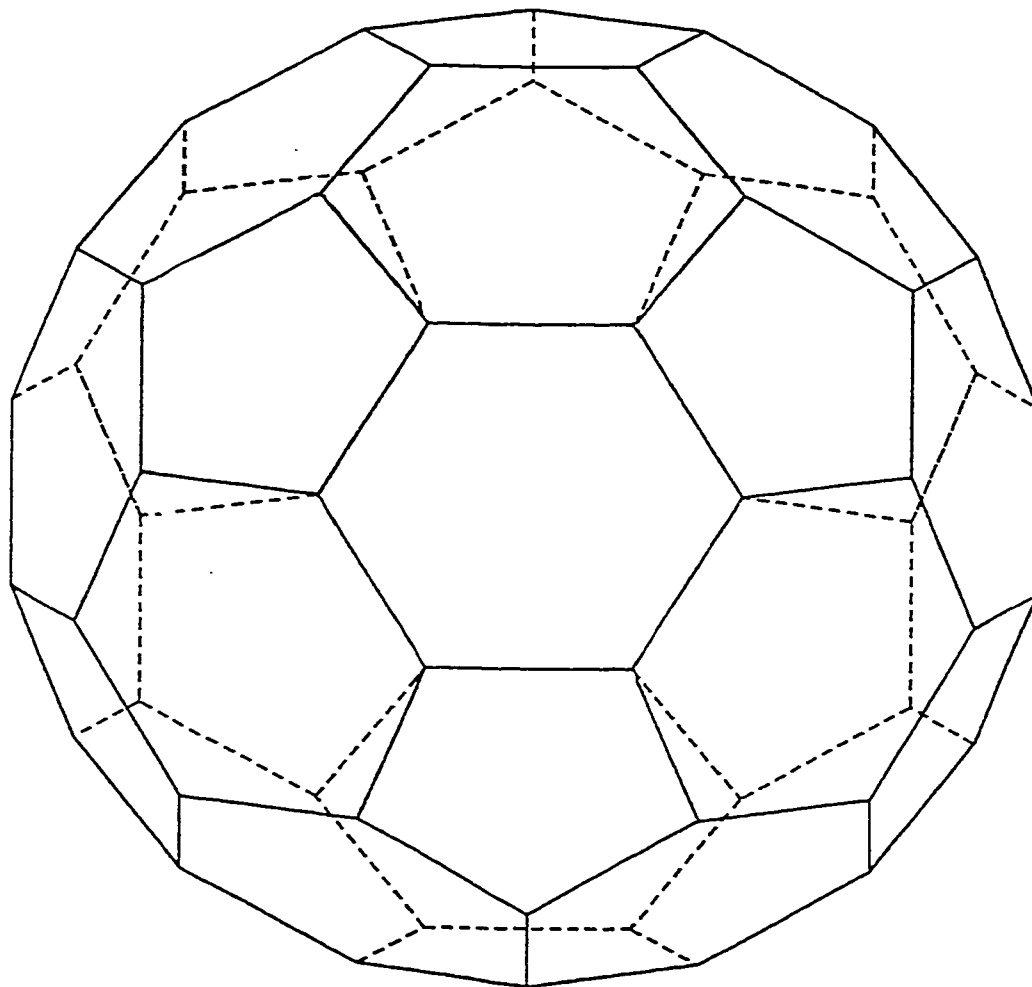


Figure 2: Mechanical drawing of the frame of the main  $4\pi$  ball.

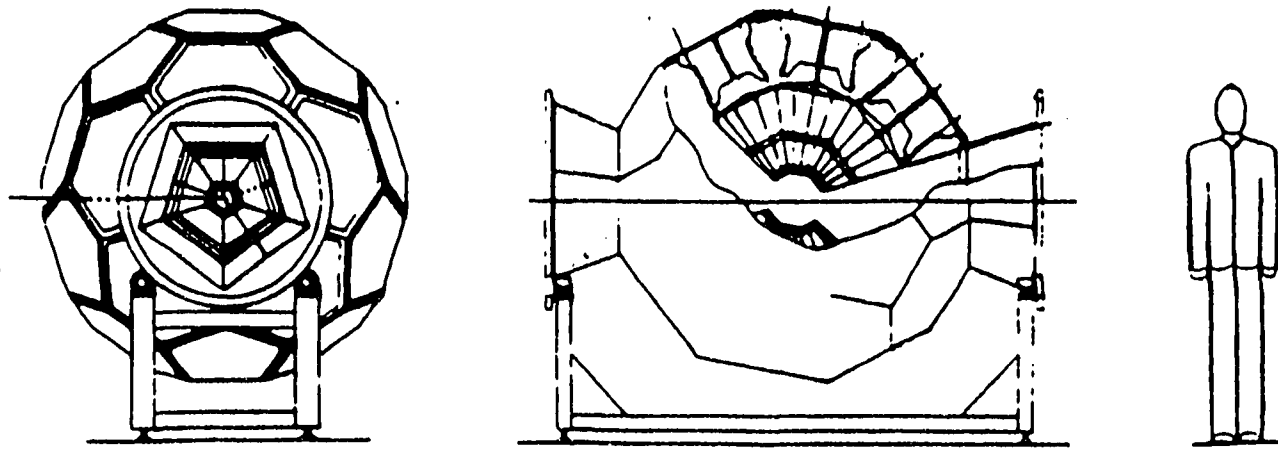


Figure 3: NSCL  $4\pi$  Array. It consists of 20 regular hexagonal modules and 12 regular pentagonal modules. Each of the hexagonal (pentagonal) modules is instrumented with six (five) light particle detectors, one Bragg curve spectrometer, and one low pressure multiwire counter.

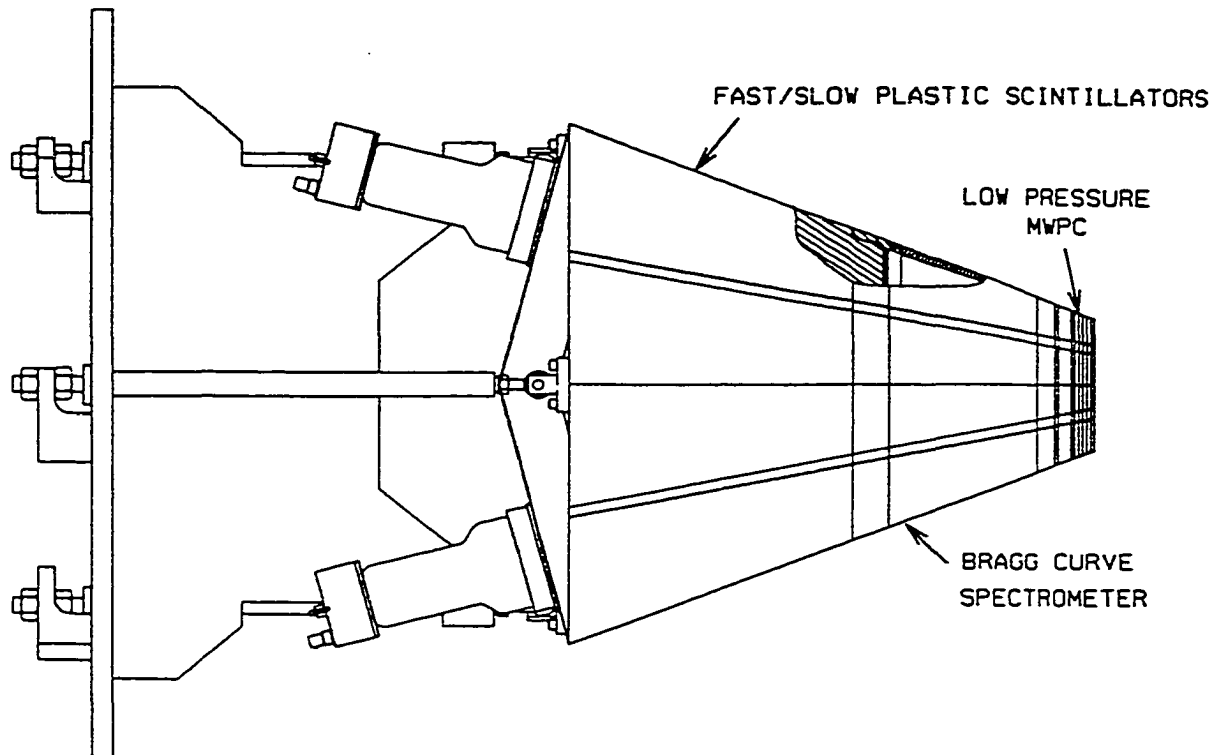


Figure 4: Side view of a hexagonal  $4\pi$  ball module, revealing three independent layers of plastic and gas detectors.

# Bragg Curve

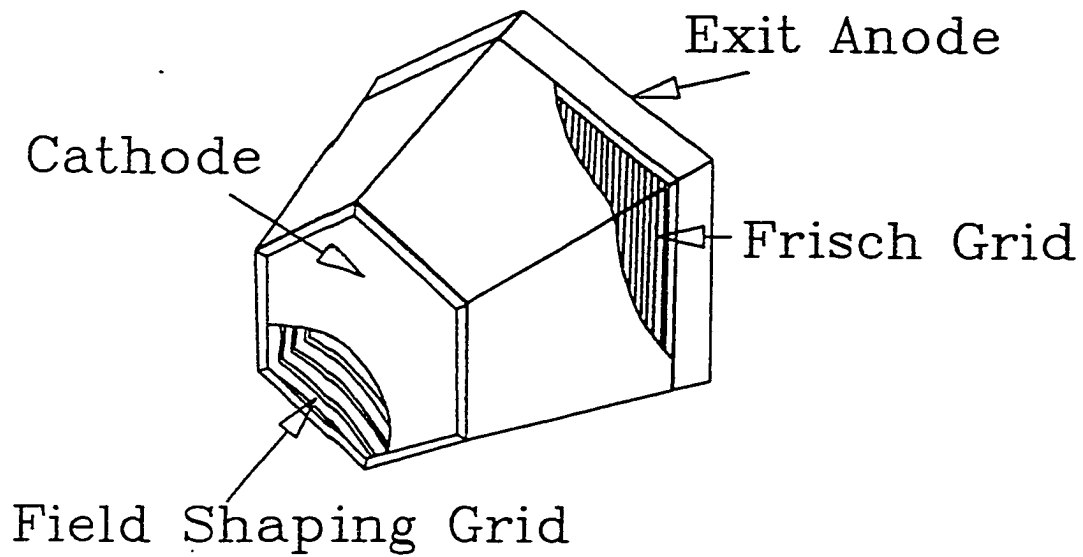


Figure 5: Schematic drawing of a Bragg Curve Counter. Cutaways show the Frisch grid and field shaping grid.

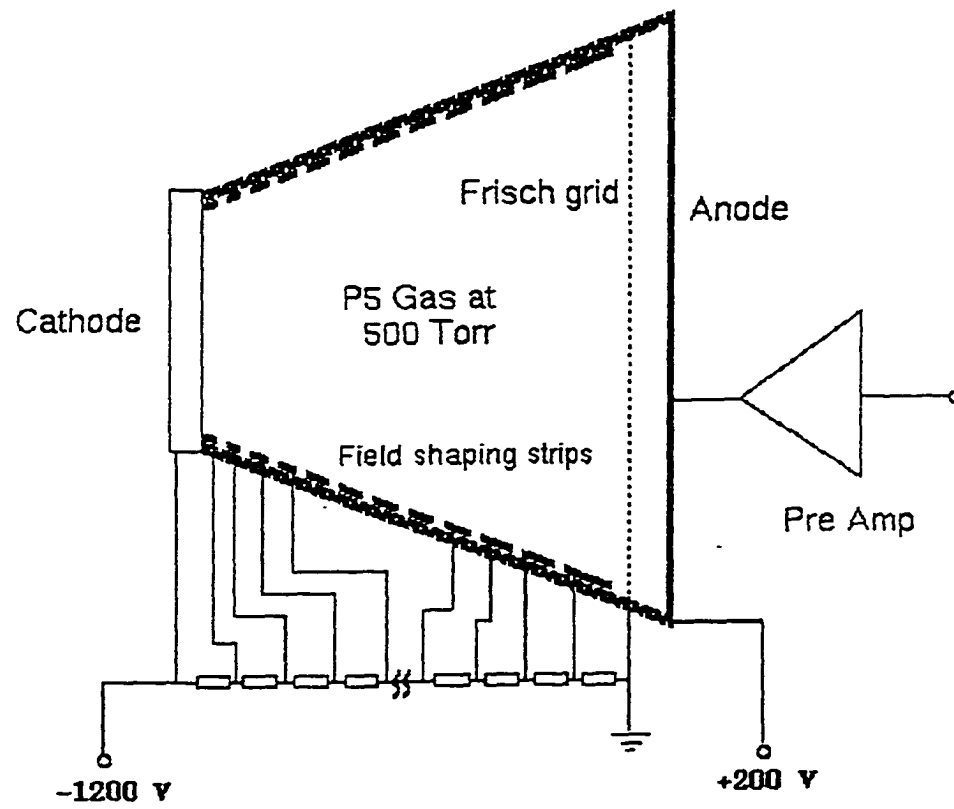


Figure 6: Schematic diagram of the MSU  $4\pi$  Bragg Curve Counter(BCC).

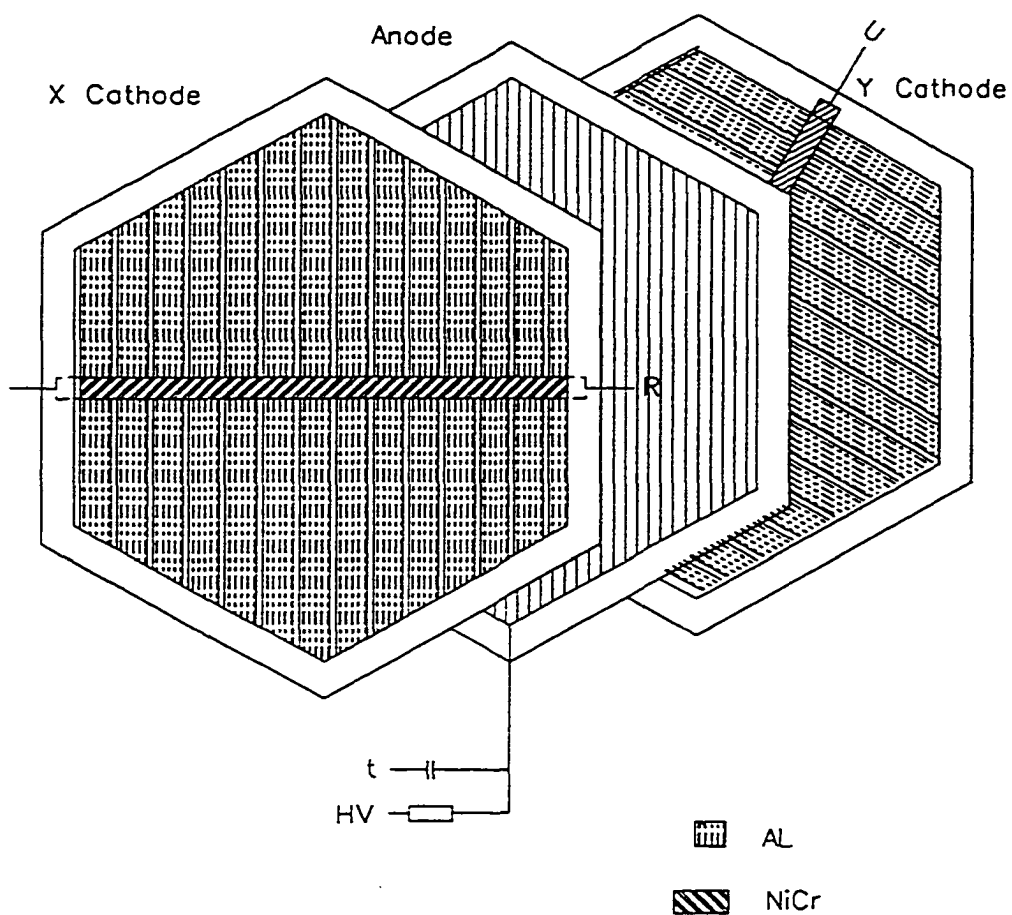


Figure 7: Exploded view of a hexagonal Multiwire Proportional Counter.

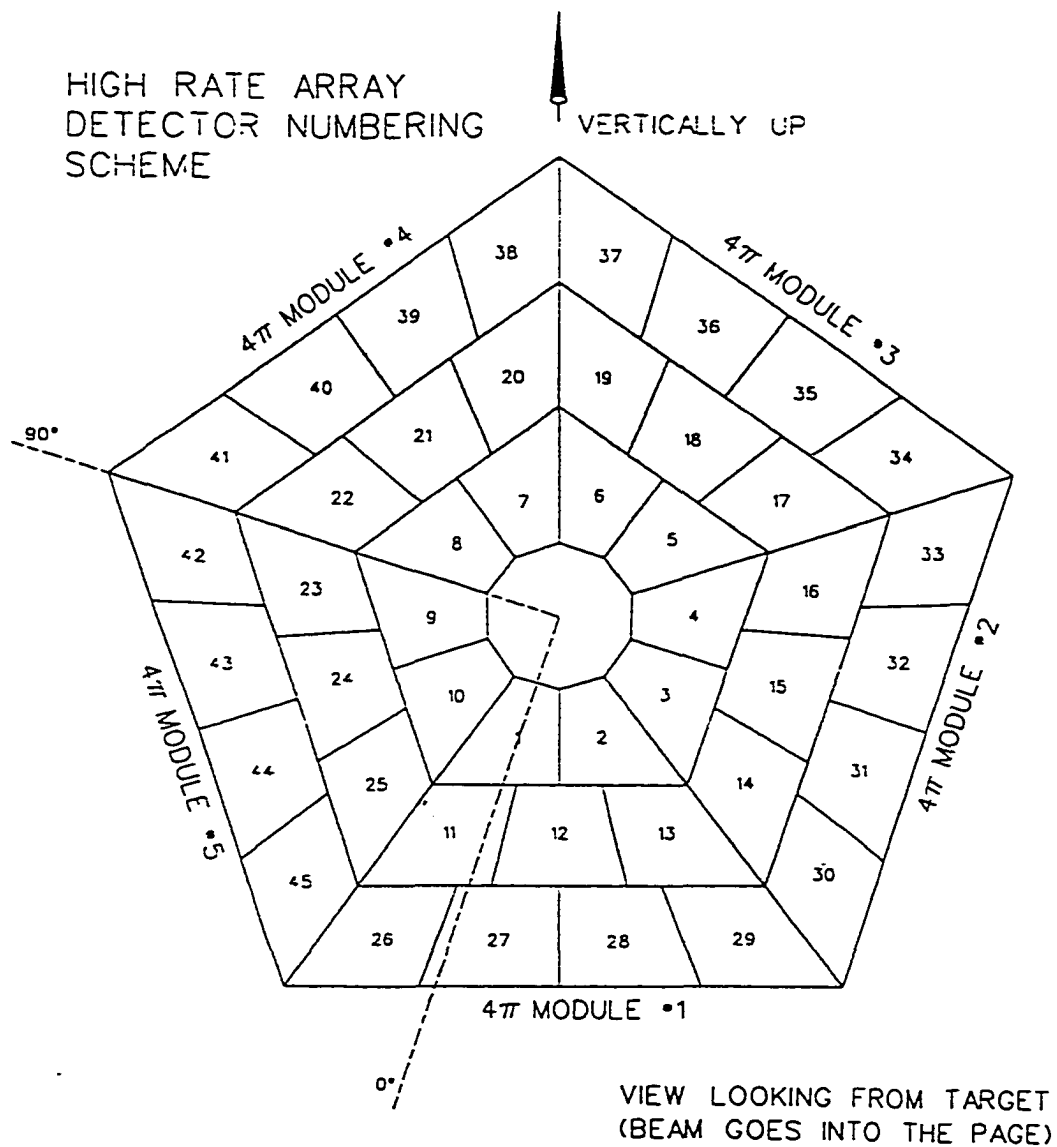


Figure 8: Arrangement of the High Rate Array detectors in the exit weldment of the ball.

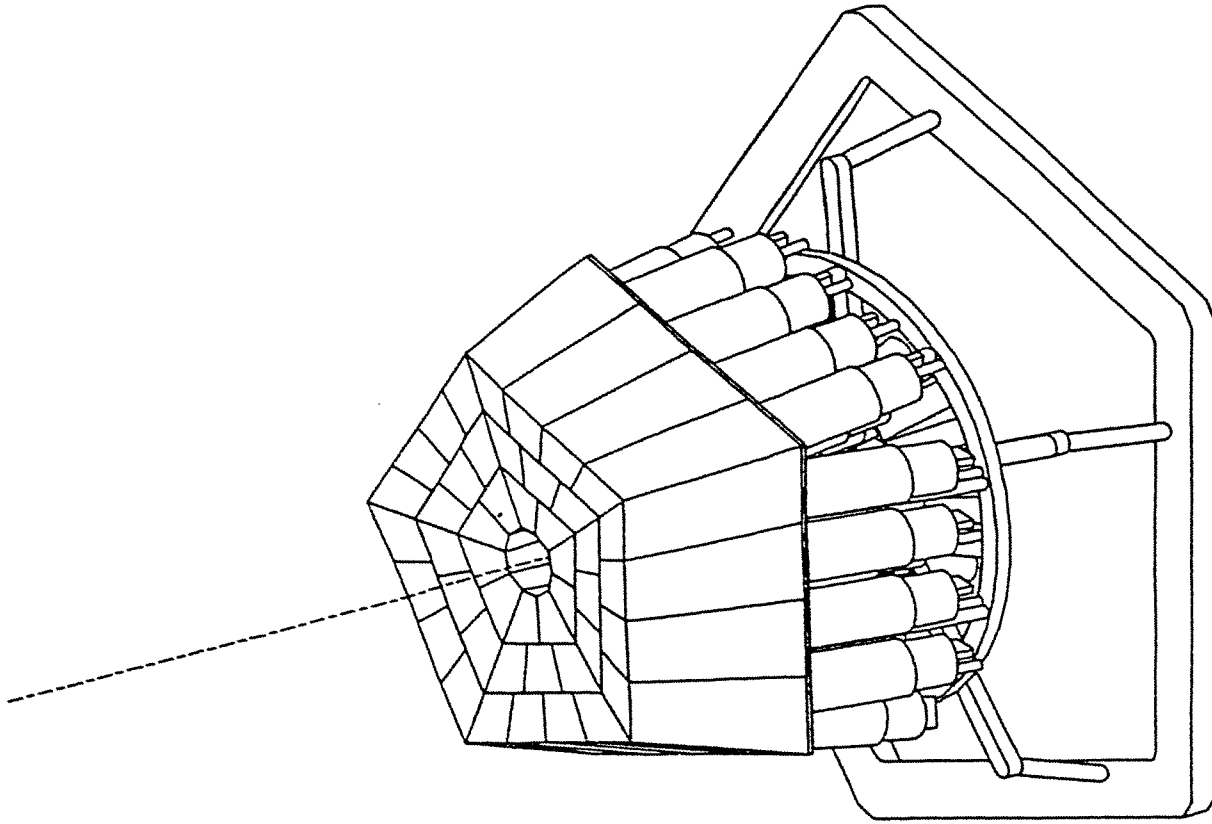


Figure 9: The High Rate Array (HRA).

Reproduced with permission of the copyright owner. Further reproduction prohibited without permission.

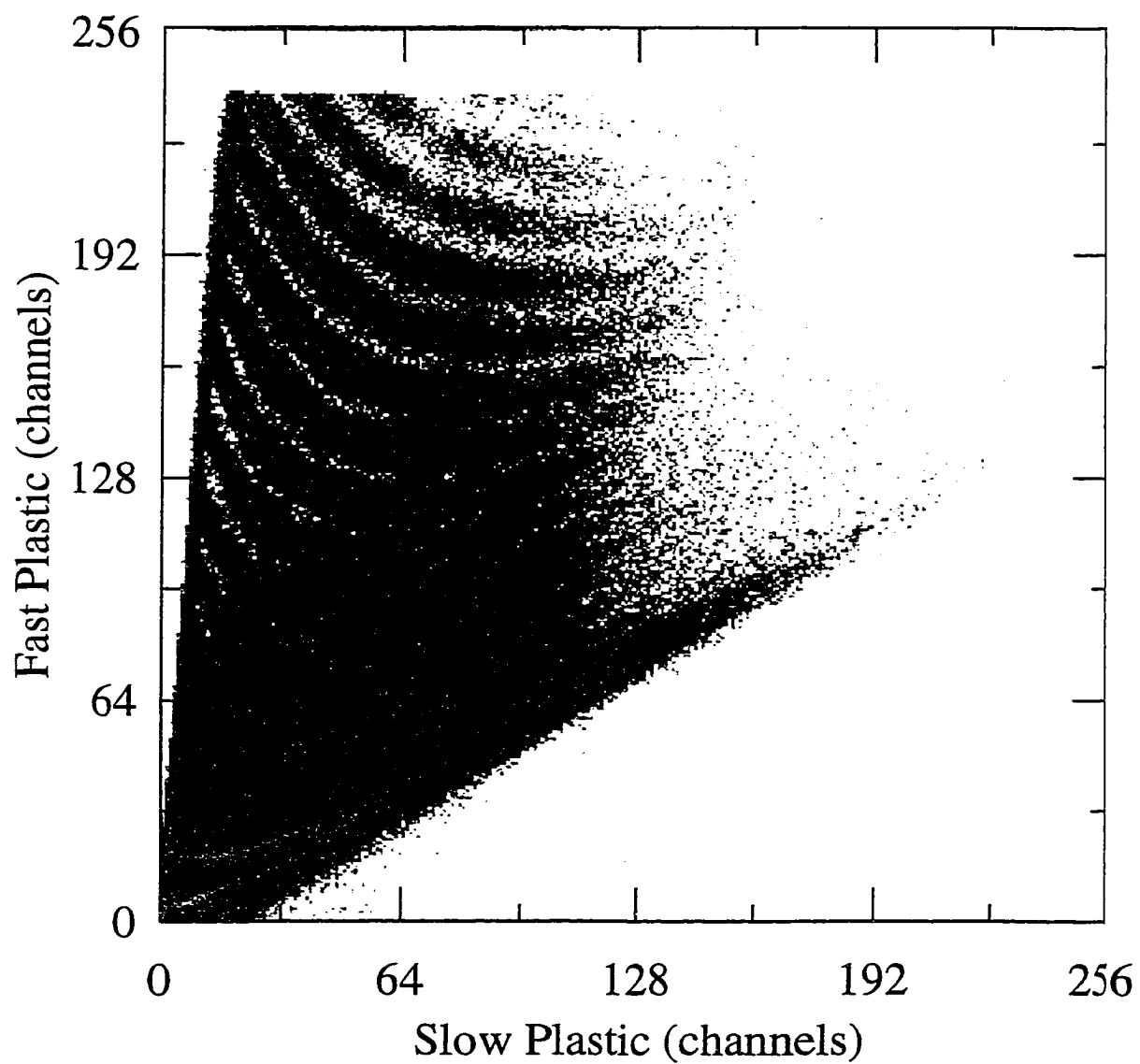


Figure 10: A typical two-dimensional histogram of the integrated signal in the fast ( $\Delta E$ ) plastic versus the integrated signal in slow ( $E$ ) plastic for an HRA detector.

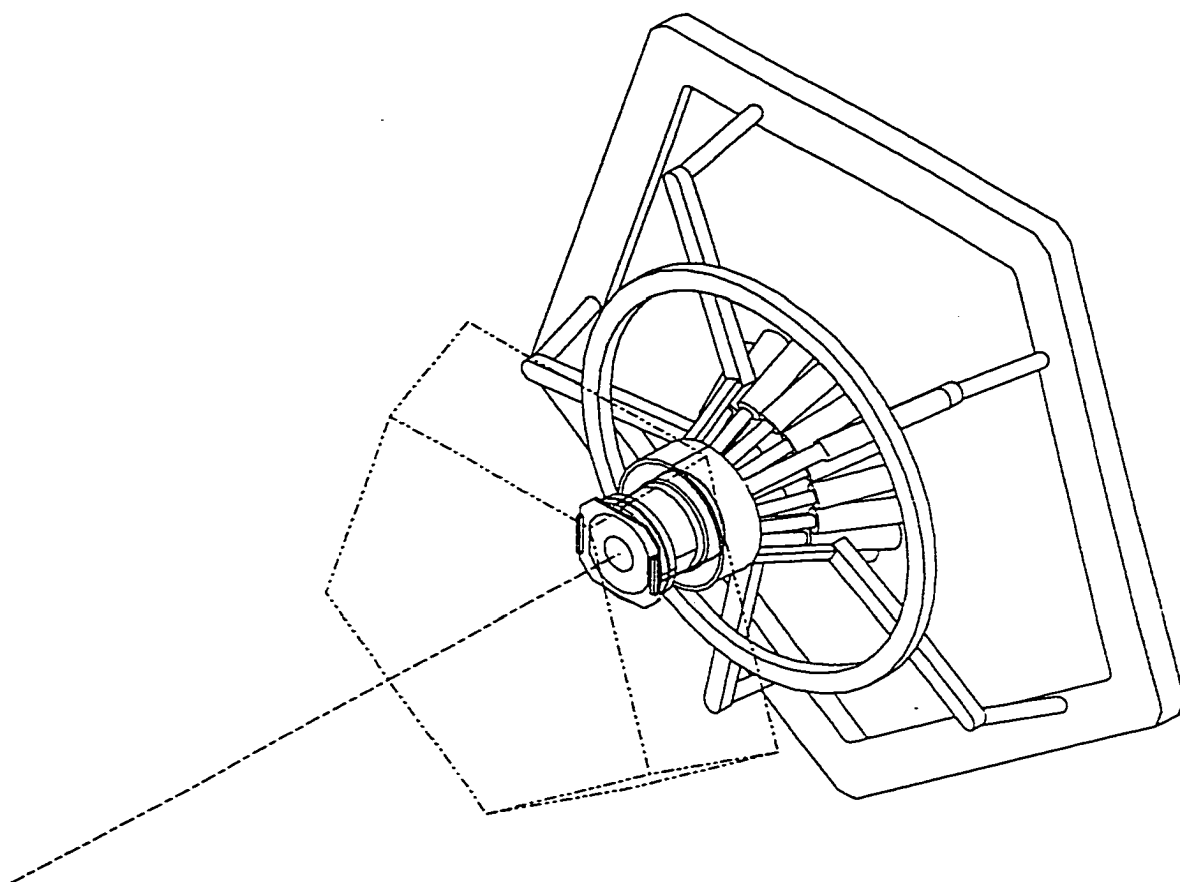


Figure 11: The Maryland Forward Array (MFA) as it attaches onto the frame of the HRA.

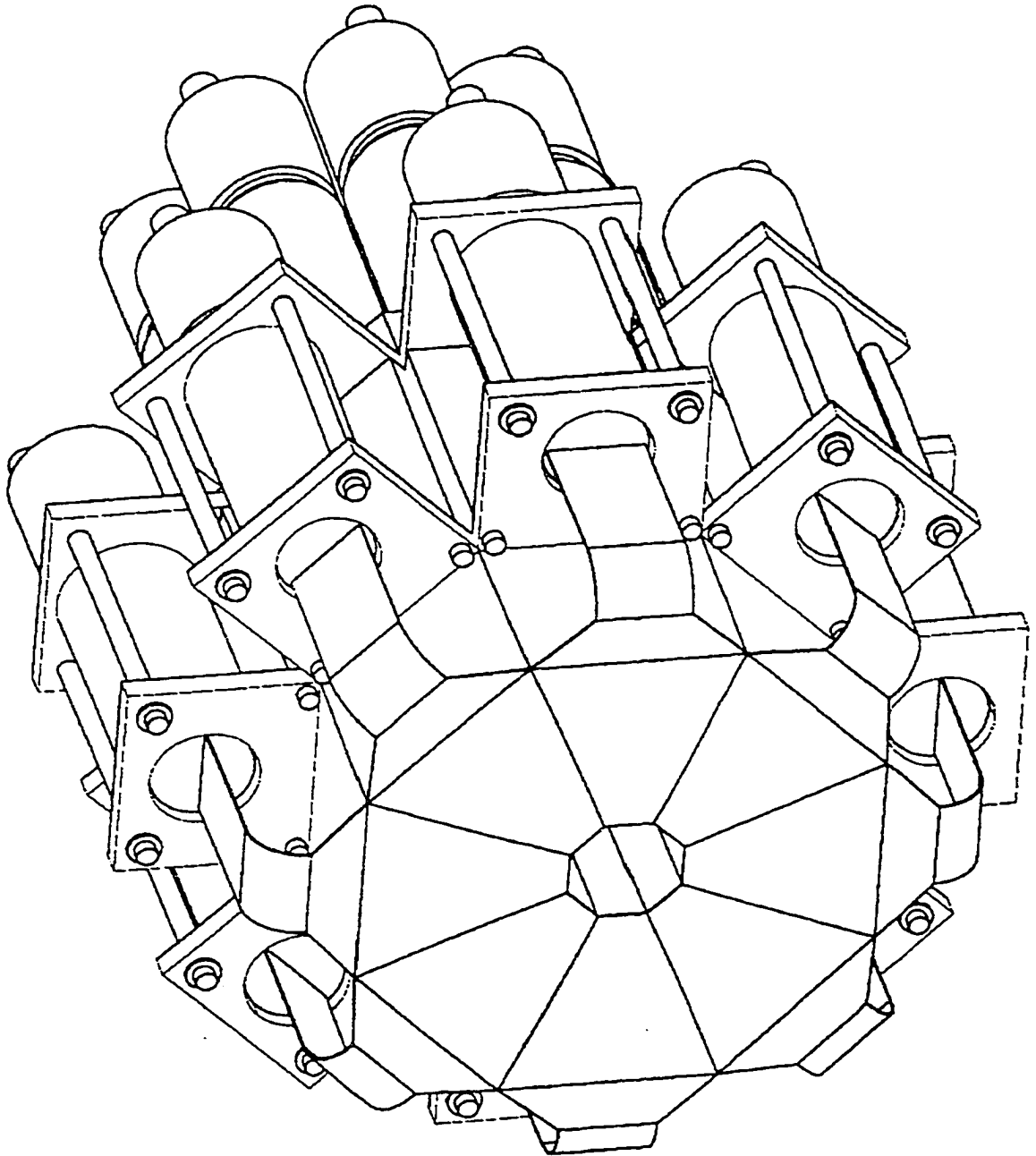


Figure 12: Assembly diagram of the ZDD, showing location of PMT's and light guides. The beam enters from the lower right.

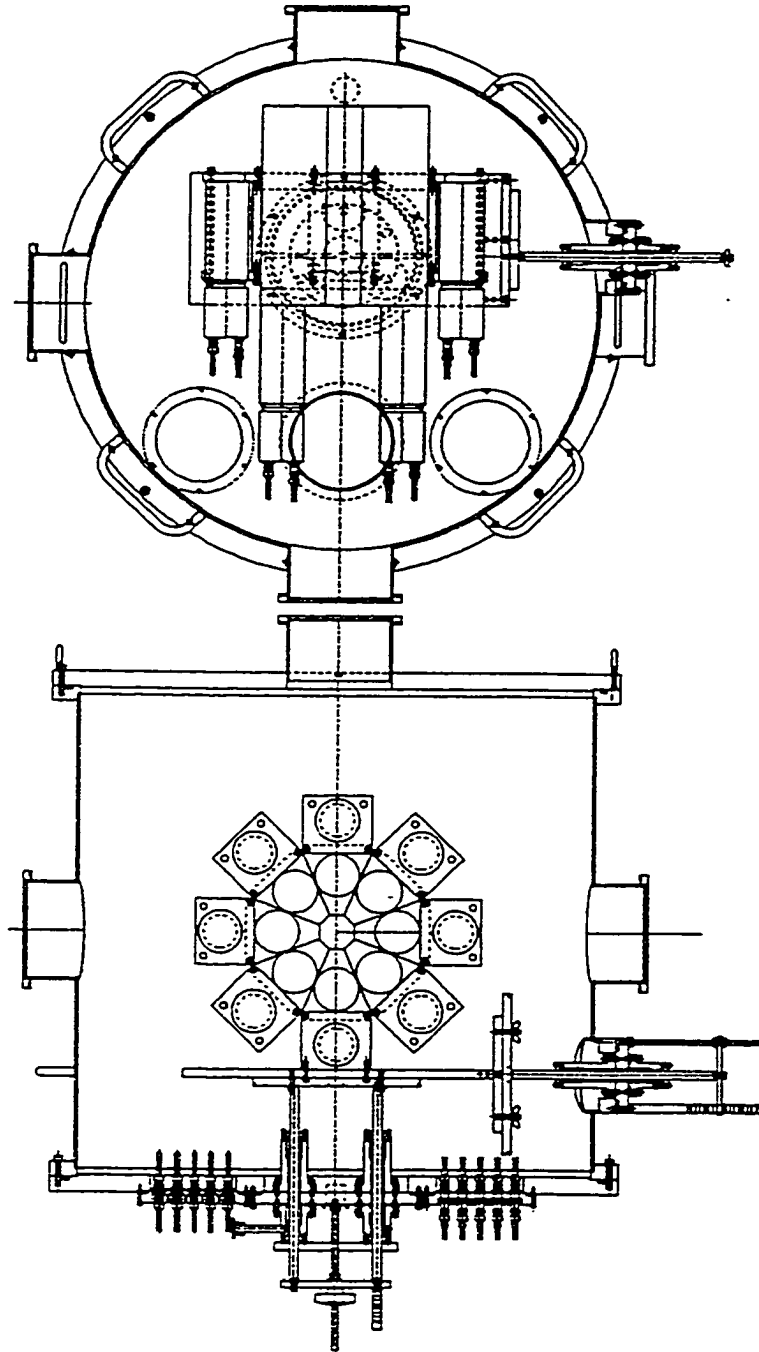


Figure 13: Mechanical drawing of the ZDD chamber. Above: Top view, with beam entering from the top of the page. Below: Rear view, looking upstream. This also shows the goniometer, used for positioning of the detector.

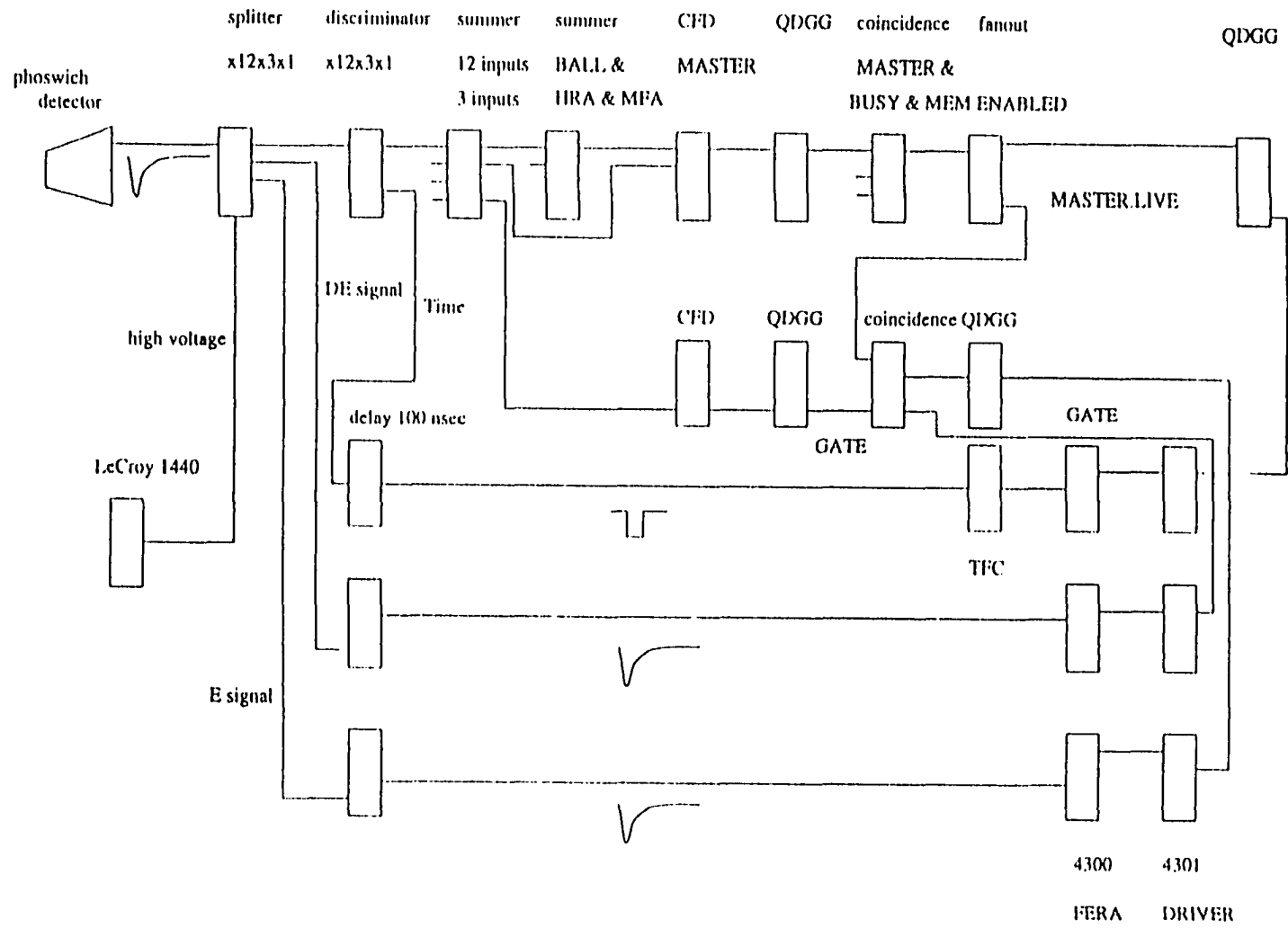


Figure 14: The ball electronics.

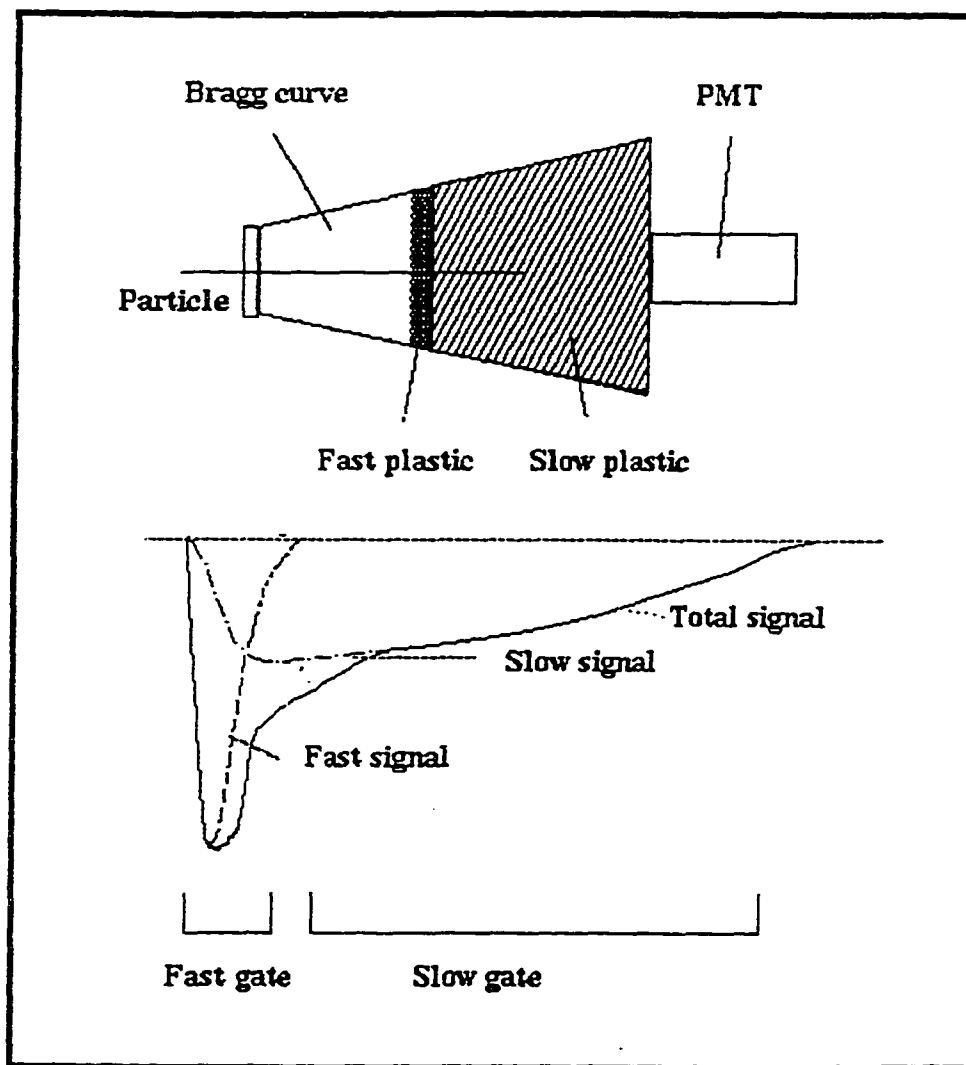


Figure 15: The signals and the gates of the fast/slow plastic telescope.

### PHOSWICH SIGNAL TIMING

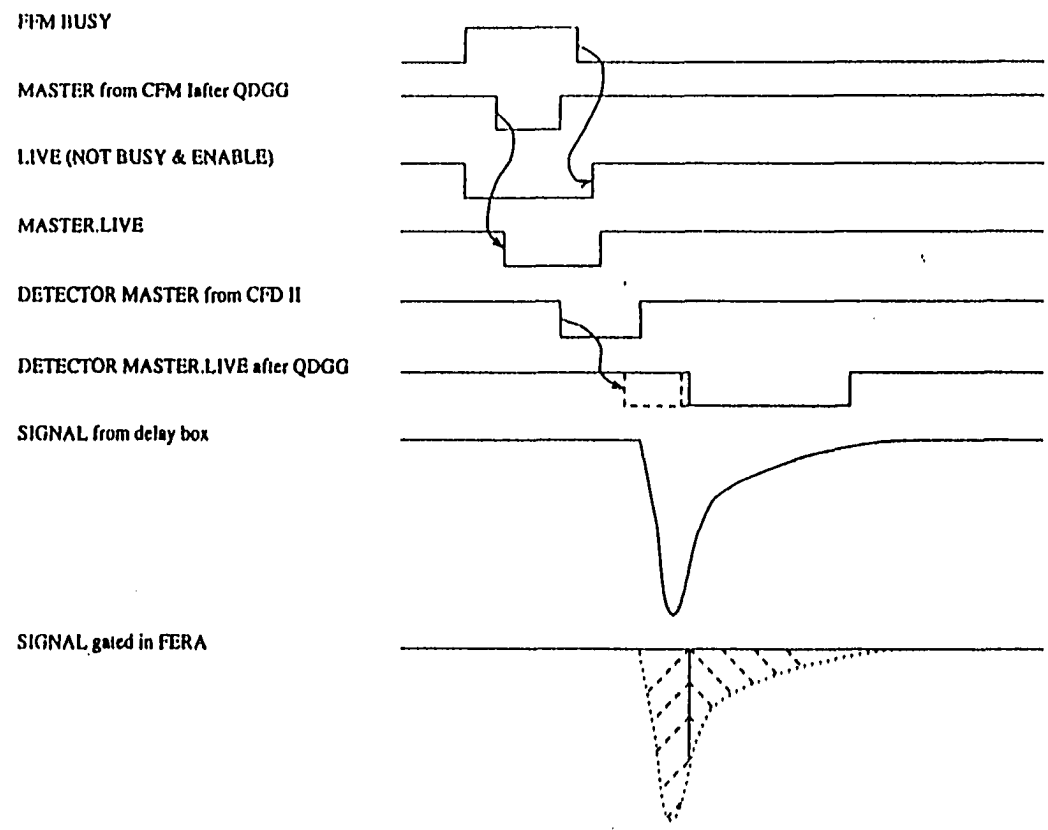


Figure 16: Phoswich timing diagram.

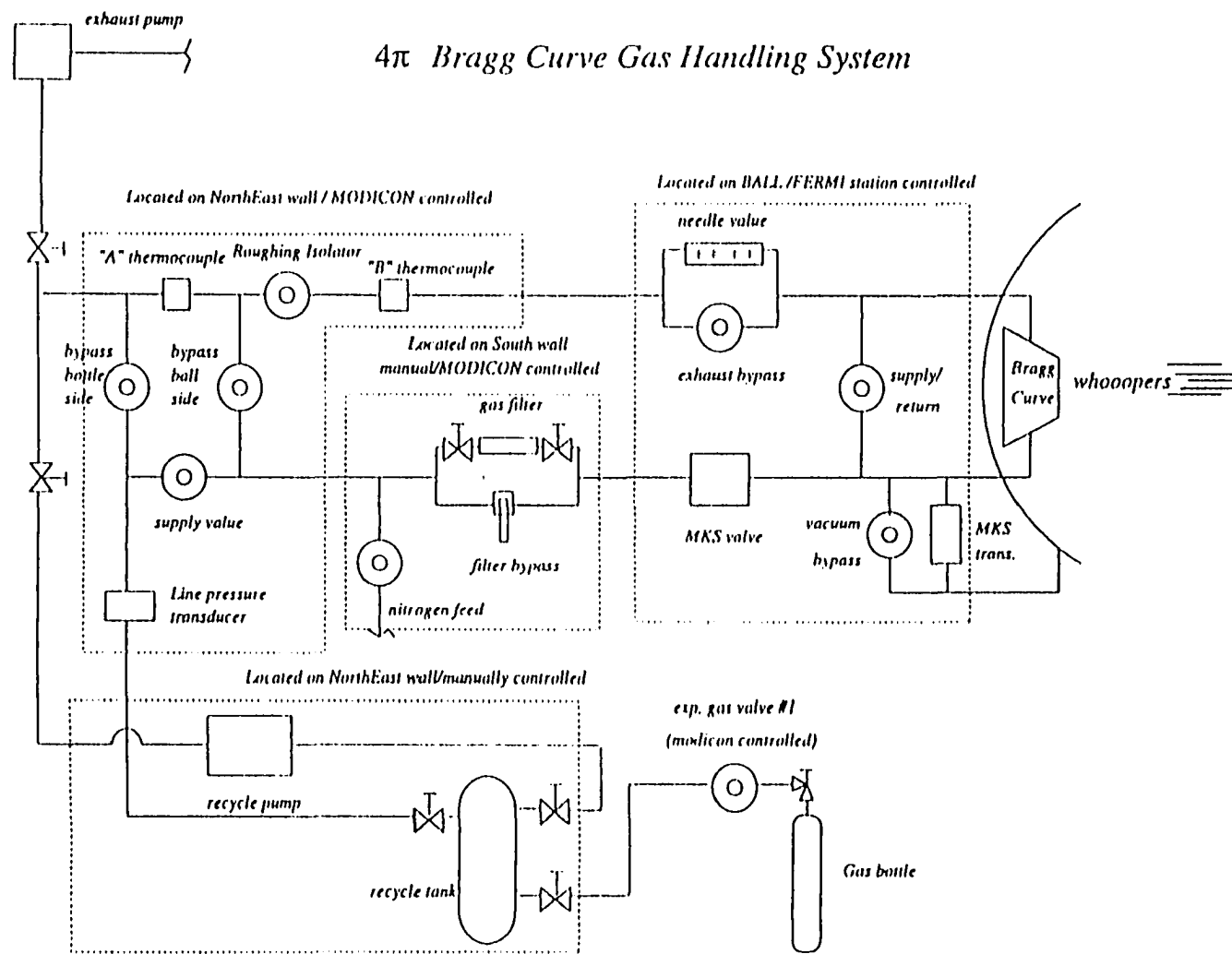


Figure 17: Bragg curve gas system.

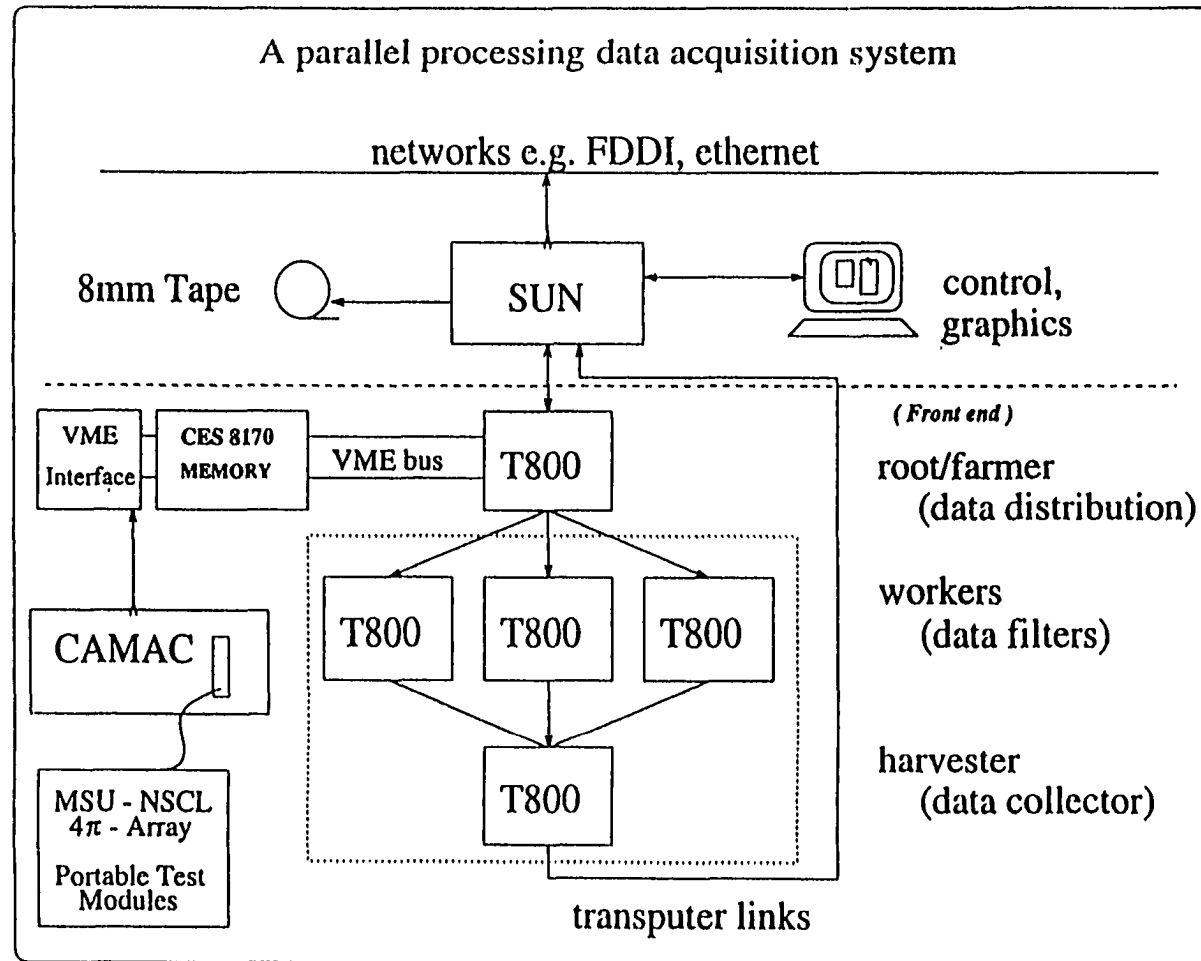


Figure 18: Front-end data acquisition system.

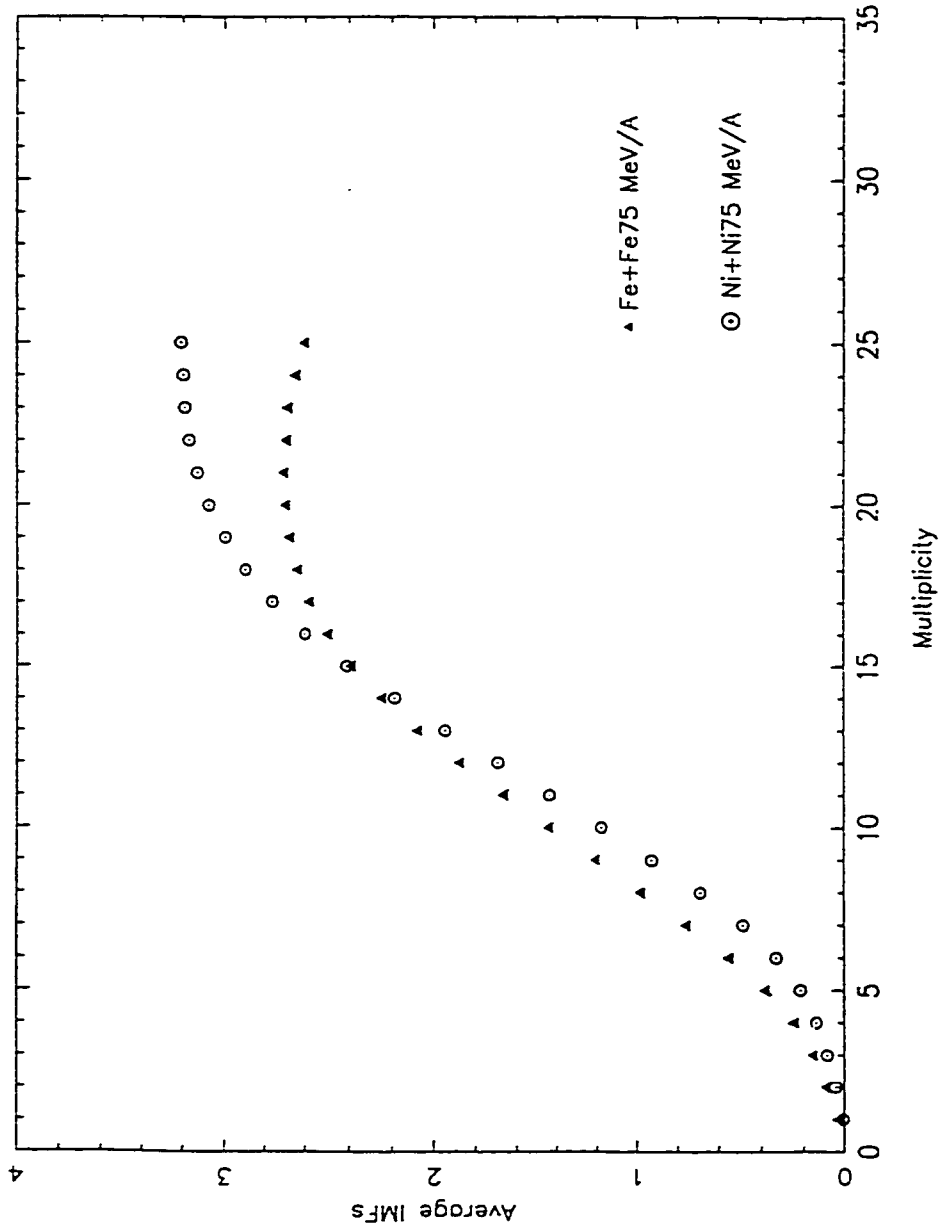


Figure 19: Average number of IMFs vs multiplicity in  $^{58}\text{Fe} + ^{58}\text{Fe}$  and  $^{58}\text{Ni} + ^{58}\text{Ni}$  at 75 A MeV.

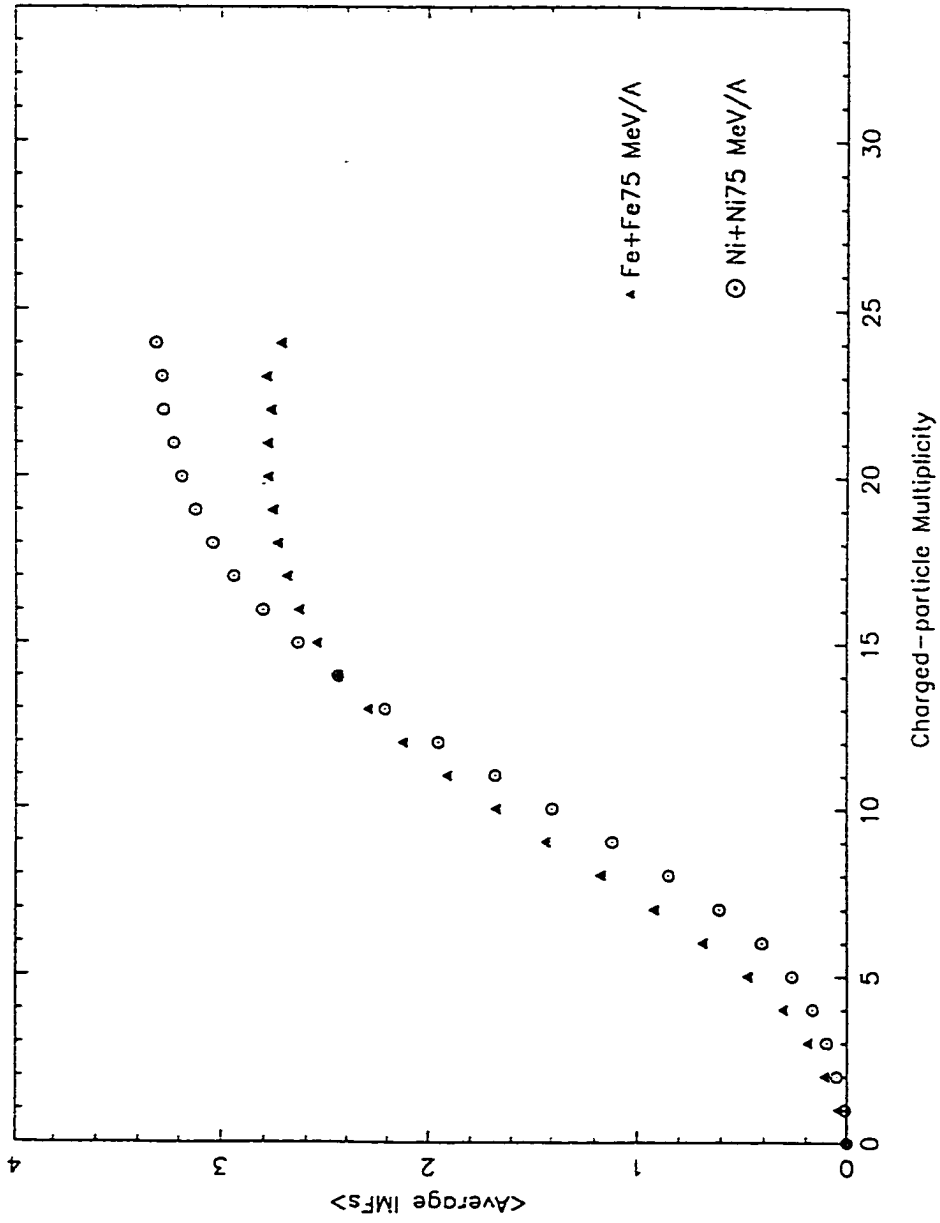


Figure 20: Average number of IMFs vs charged particle multiplicity in  $^{58}\text{Fe} + ^{58}\text{Fe}$  and  $^{58}\text{Ni} + ^{58}\text{Ni}$  at 75 A MeV.

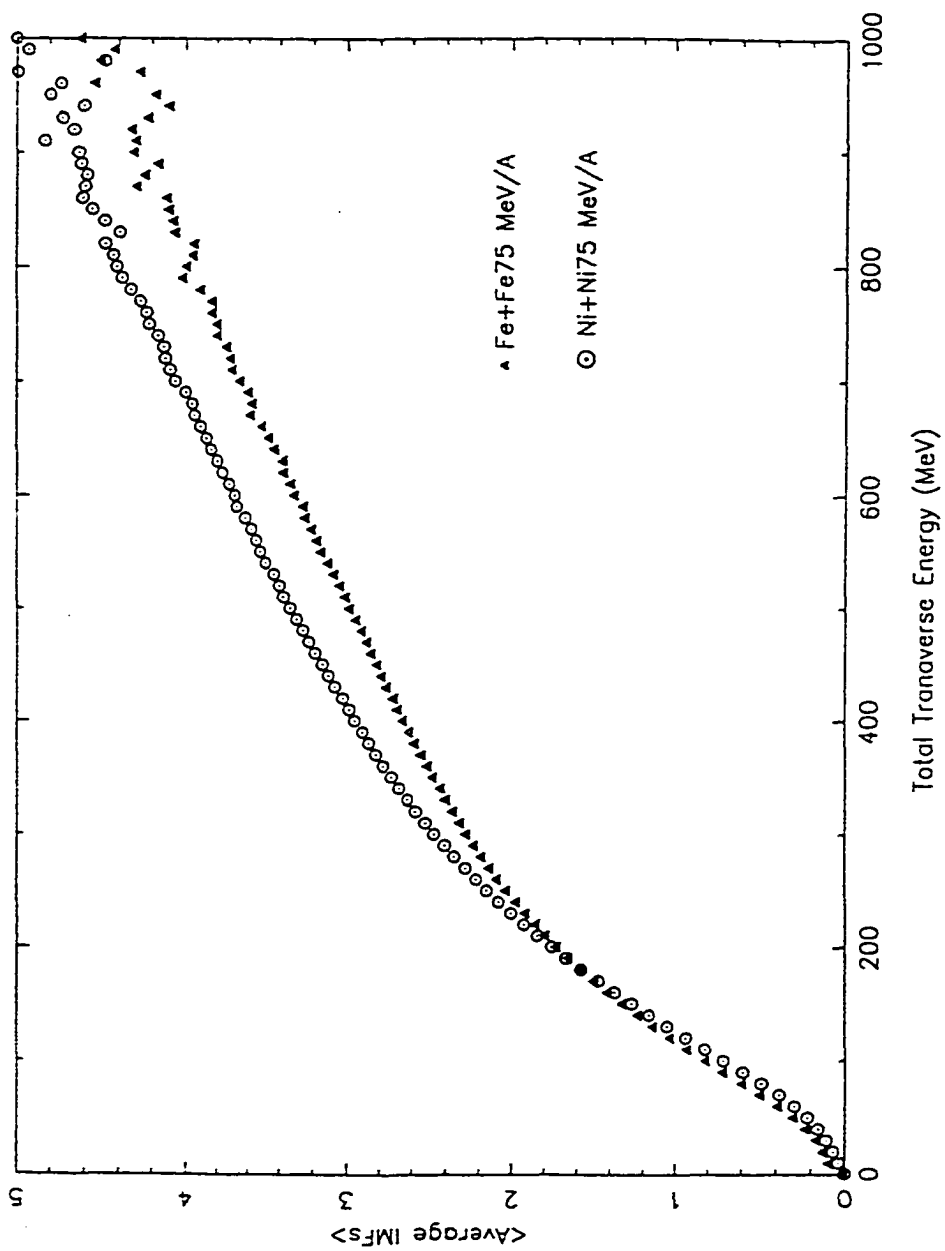


Figure 21: IMFs vs transverse energy for  $^{58}\text{Fe} + ^{58}\text{Fe}$  and  $^{58}\text{Ni} + ^{58}\text{Ni}$  at 75 A MeV.

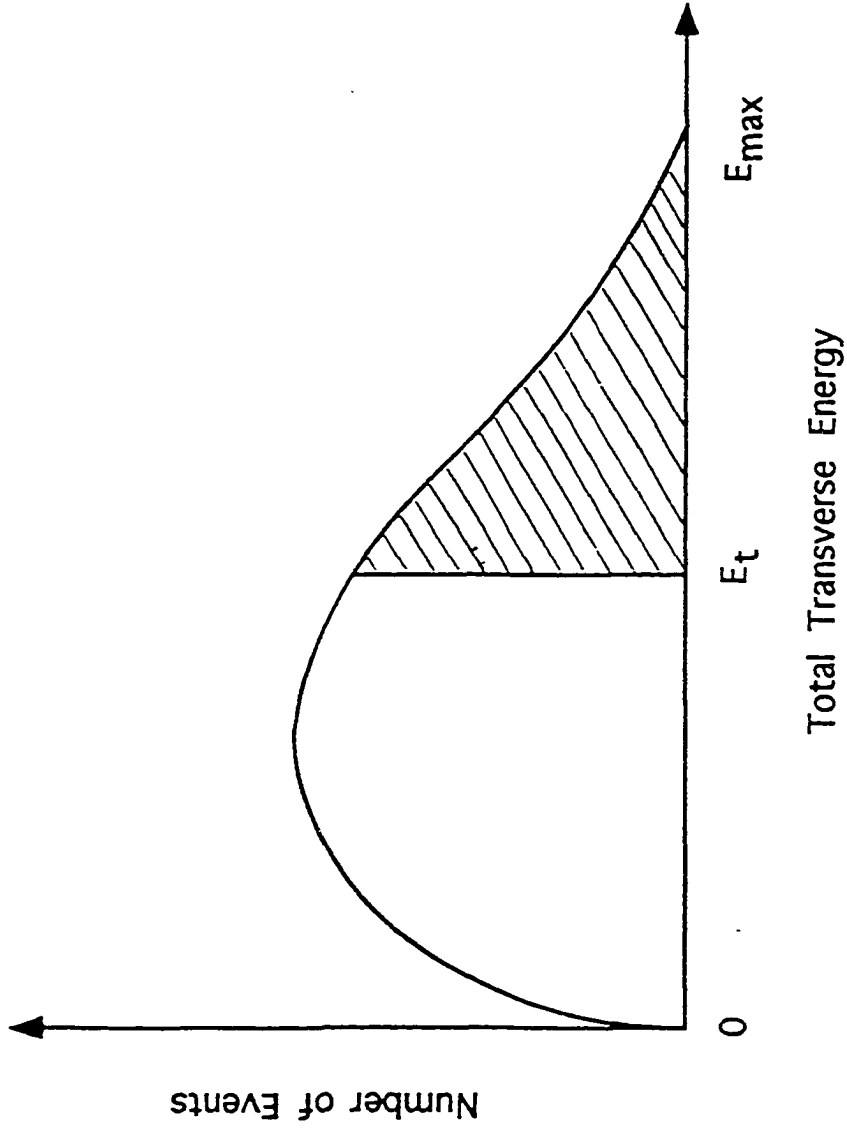


Figure 22: Calculation of impact parameter  $b$  from transverse energy spectrum.

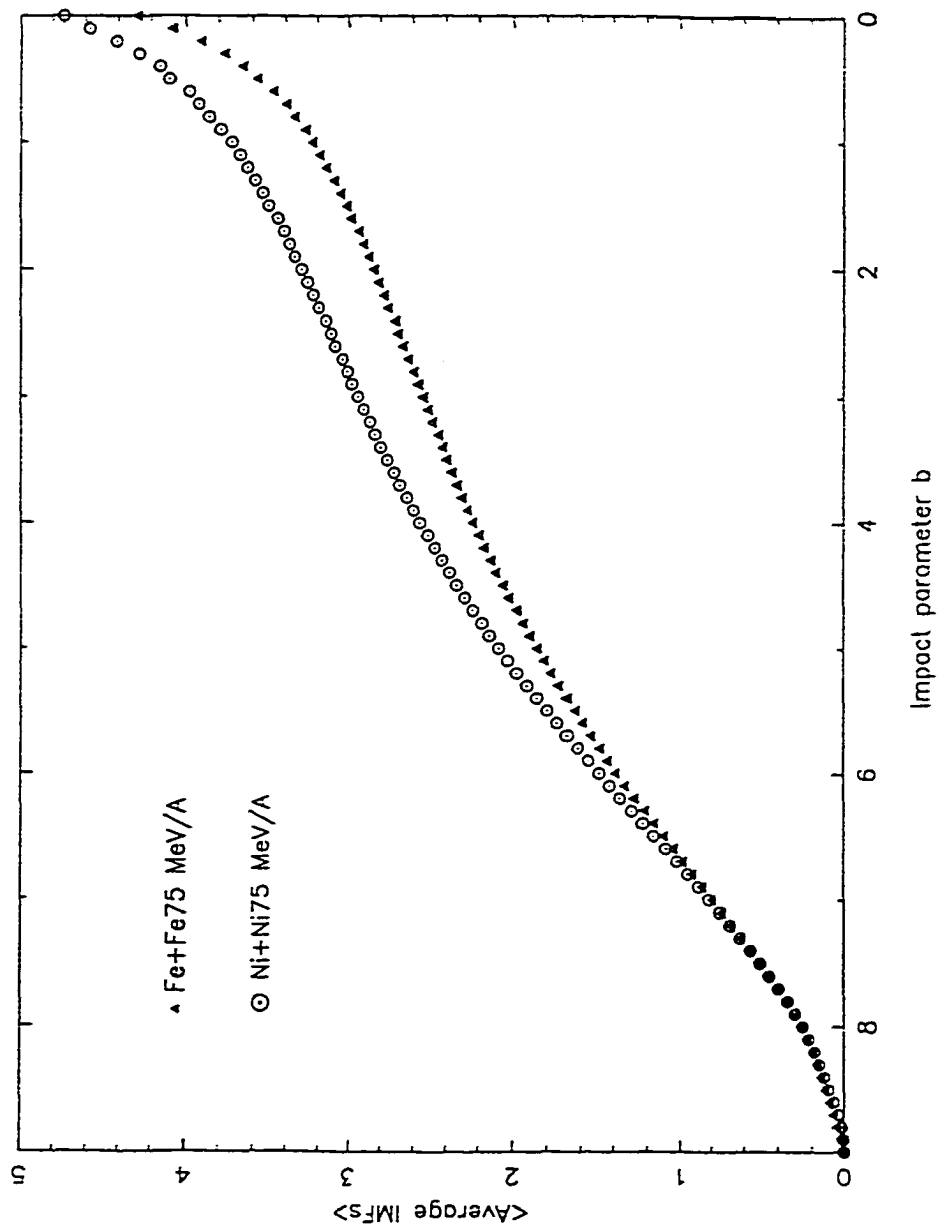


Figure 23: Average number of IMFs vs impact parameter  $b$  in  $^{58}\text{Fe} + ^{58}\text{Fe}$  and  $^{58}\text{Ni} + ^{58}\text{Ni}$  at 75 A MeV.

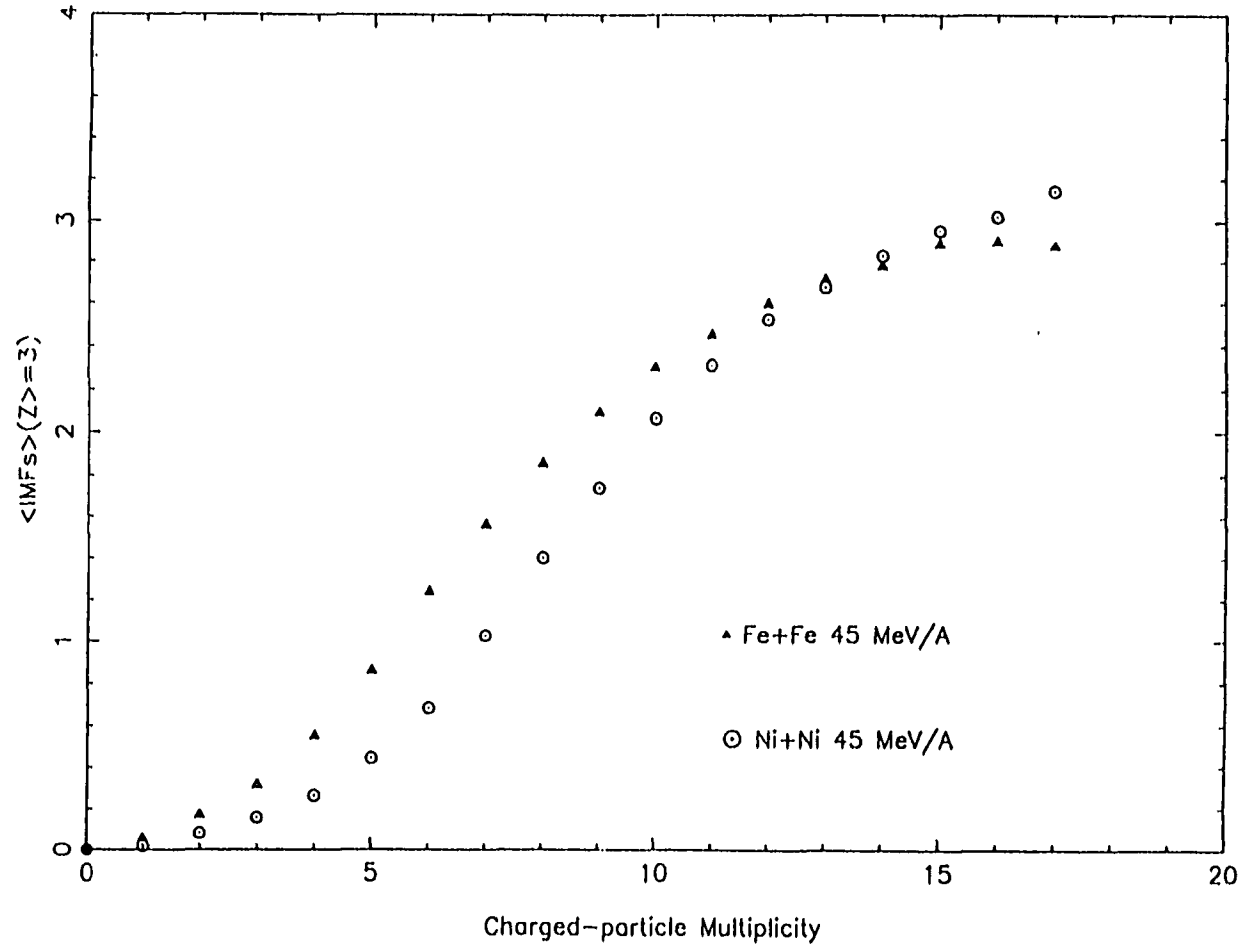


Figure 24: Average number of IMFs versus charged particle multiplicity in  $^{58}\text{Fe} + ^{58}\text{Fe}$  and  $^{58}\text{Ni} + ^{58}\text{Ni}$  at 45 A MeV with much lower statistics (130k events).

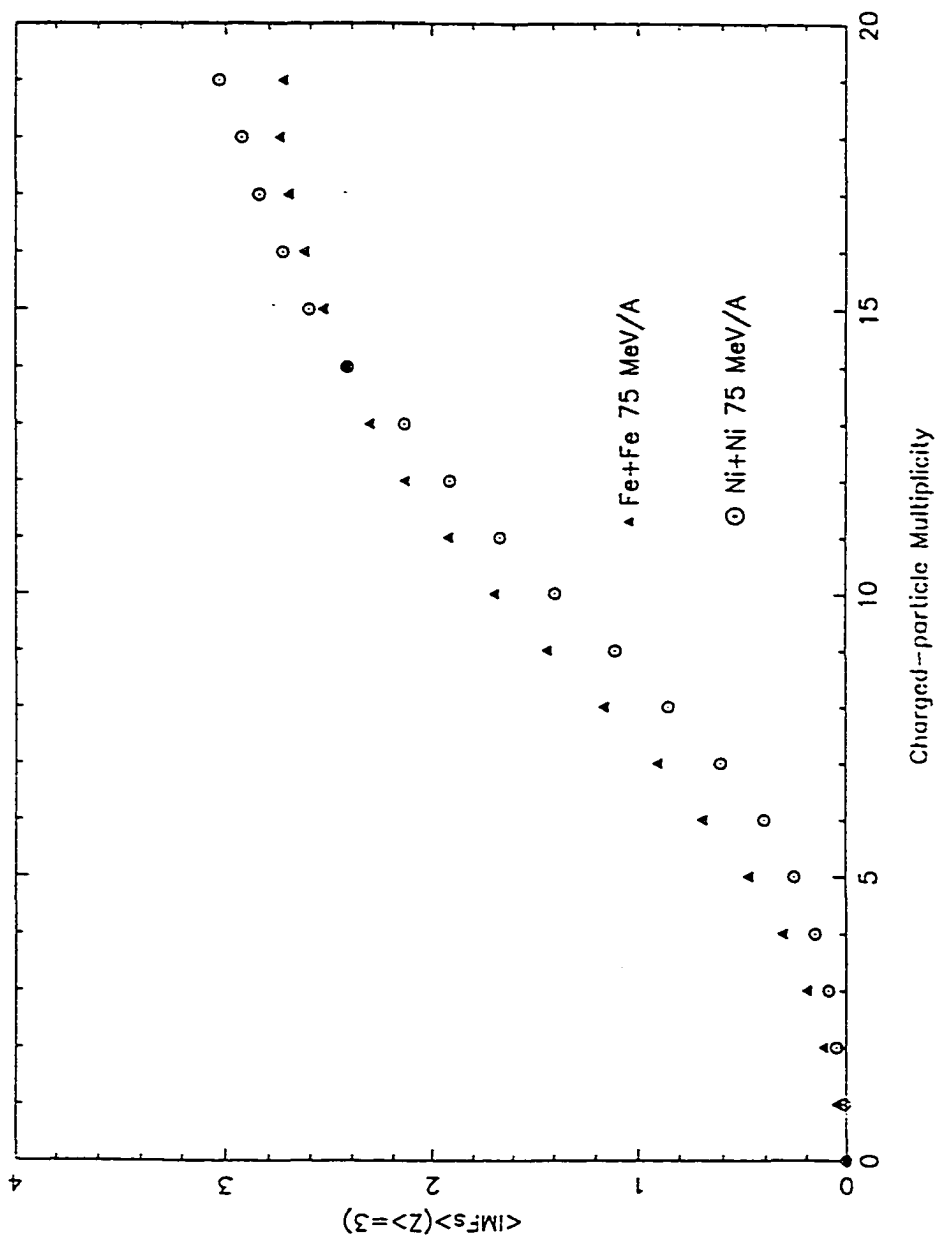


Figure 25: Average number of IMFs versus charged particle multiplicity in  $^{58}\text{Fe} + ^{58}\text{Fe}$  and  $^{58}\text{Ni} + ^{58}\text{Ni}$  at 75 A MeV with 130k events.

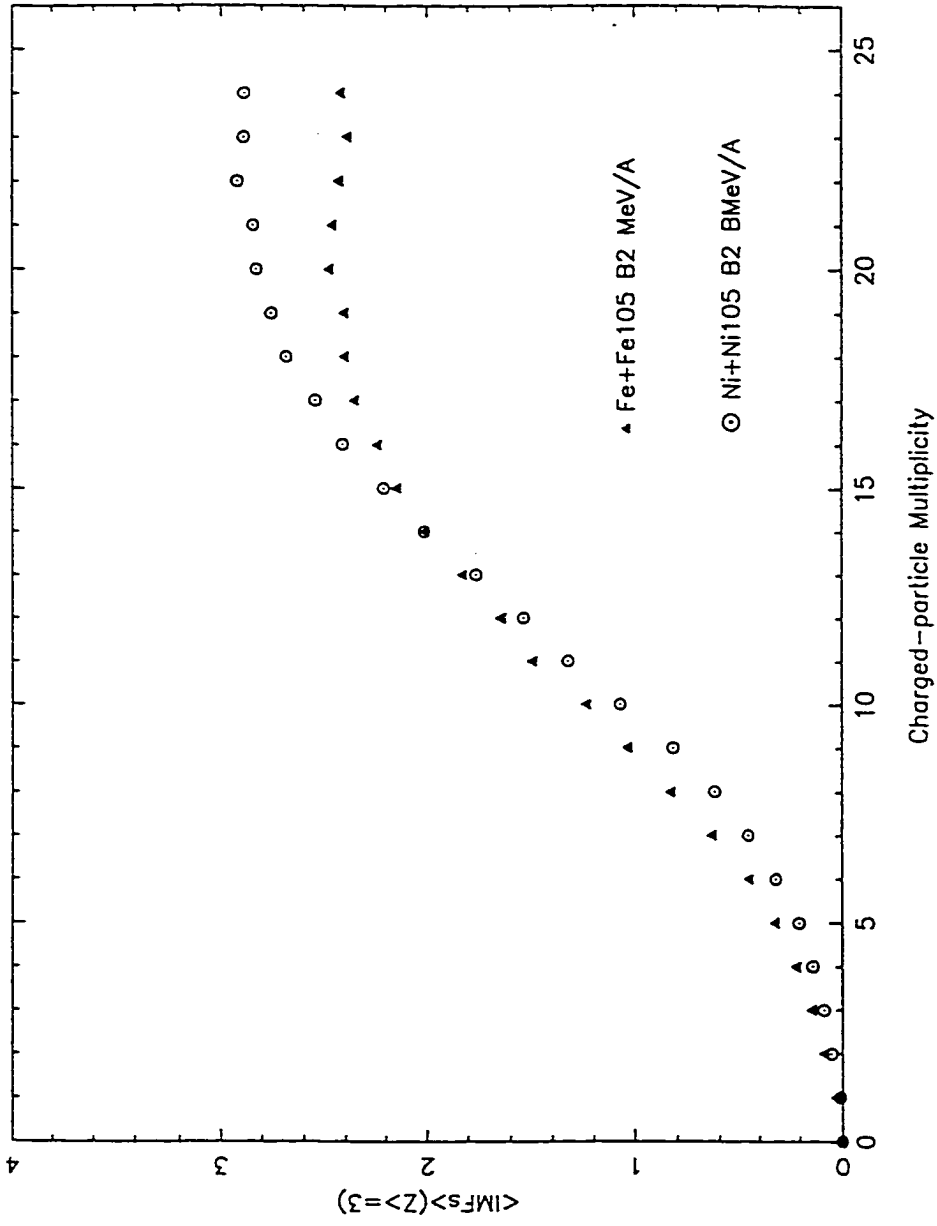


Figure 26: Average number of IMFs versus charged particle multiplicity in  $^{58}\text{Fe} + ^{58}\text{Fe}$  and  $^{58}\text{Ni} + ^{58}\text{Ni}$  at 105 A MeV with 130k events.

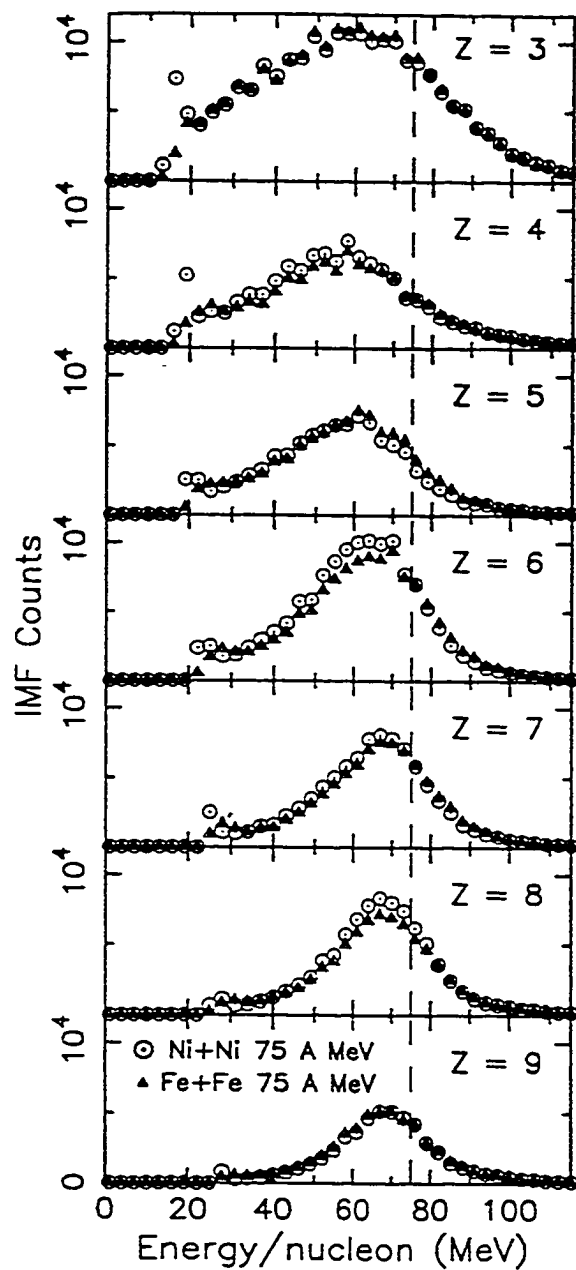


Figure 27: IMF energy spectra at  $5.4^\circ$  for 75 A MeV  $^{58}\text{Ni}+^{58}\text{Ni}$  and  $^{58}\text{Fe}+^{58}\text{Fe}$ . Beam velocity fragments have energy 75 A MeV, shown by the dashed line.

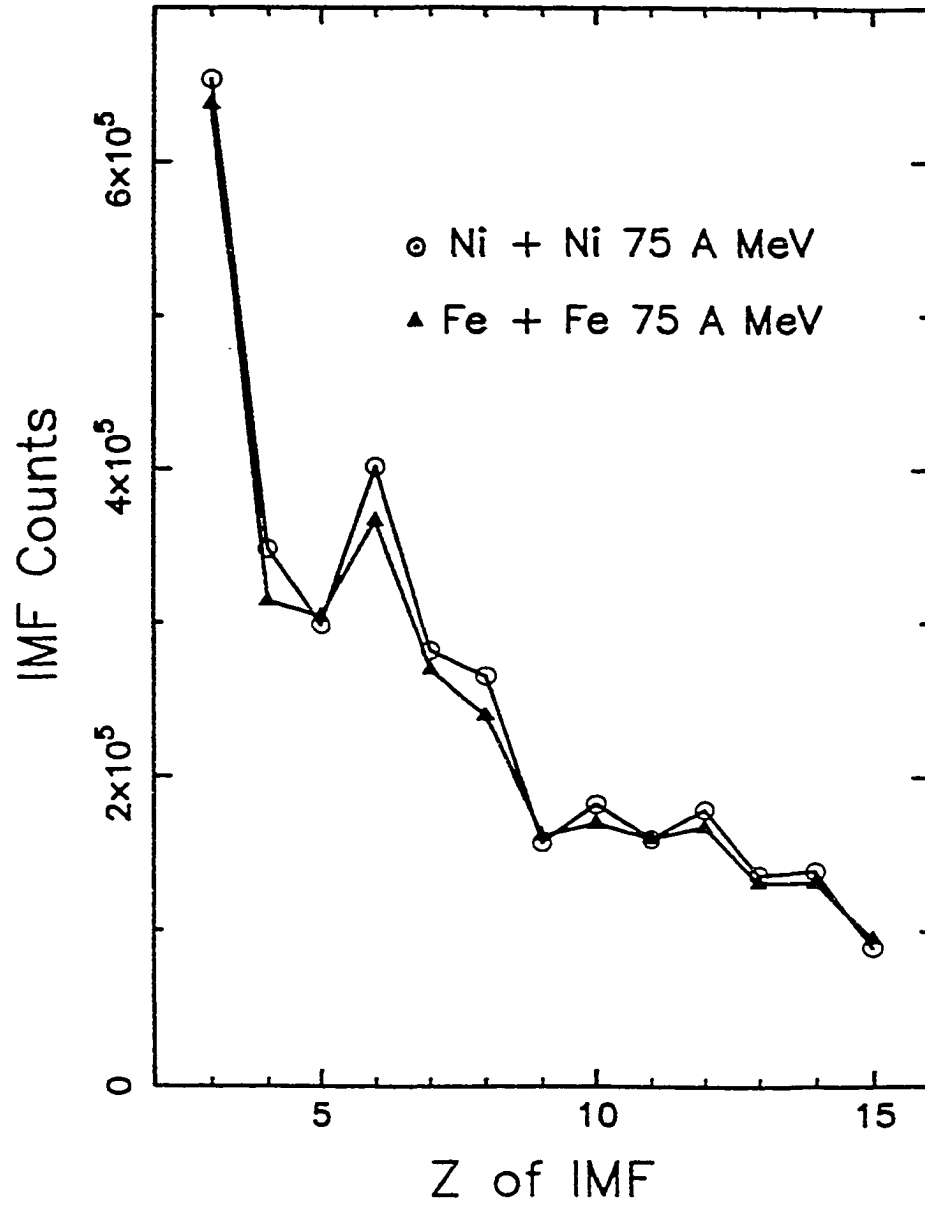


Figure 28: Number of IMFs as a function of  $Z$  for  $^{58}\text{Ni}+^{58}\text{Ni}$  and  $^{58}\text{Fe}+^{58}\text{Fe}$  obtained by integrating the energy spectra starting at 30 A MeV (see Fig. 27).

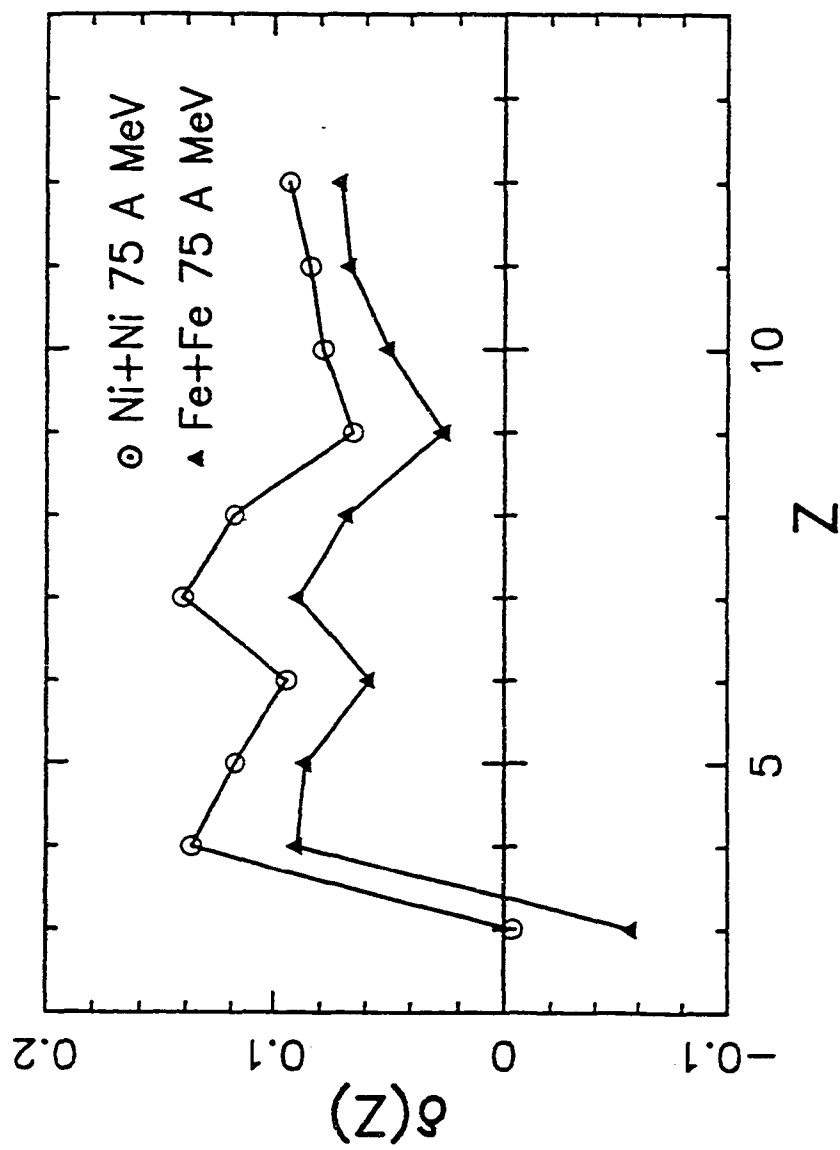


Figure 29: Excess of even- $Z$  over odd- $Z$  fragments as a function of  $Z$  calculated from the data shown in Fig. 28.  $\delta(Z)$  is defined in Eq. (4.1).

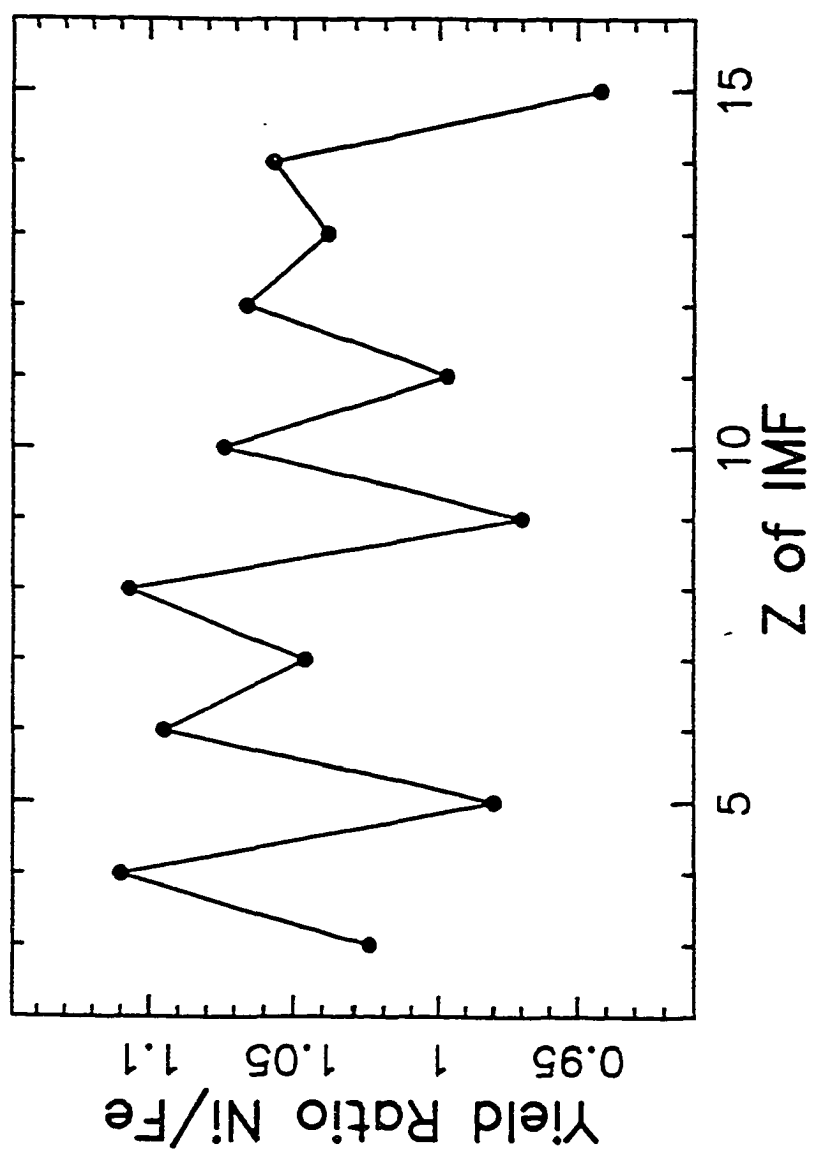


Figure 30: Yield ratios of beam-velocity fragments as a function of Z for 75 A MeV  $^{58}\text{Ni}+^{58}\text{Ni}$  and  $^{58}\text{Fe}+^{58}\text{Fe}$ .

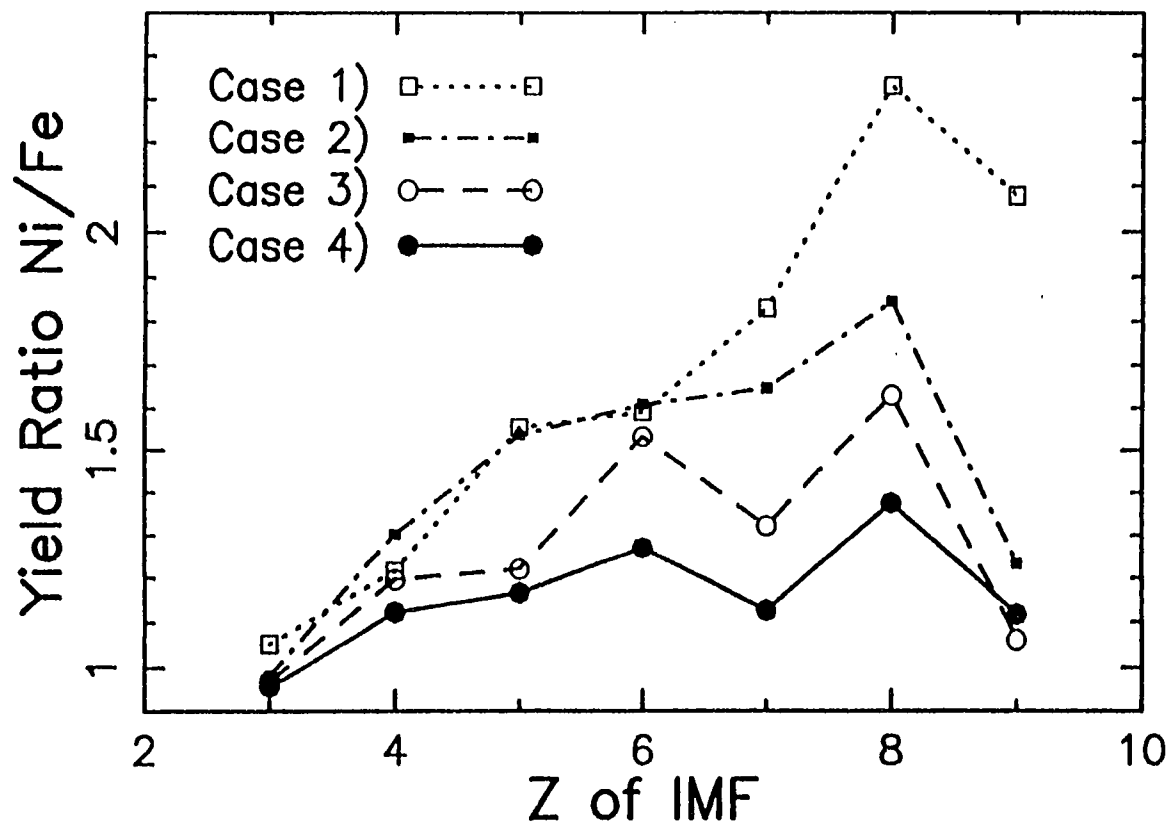


Figure 31: Yield ratios as a function of Z for sources of  $^{58}\text{Ni}$  and  $^{58}\text{Fe}$  calculated for each of four classes of emitted fragments.

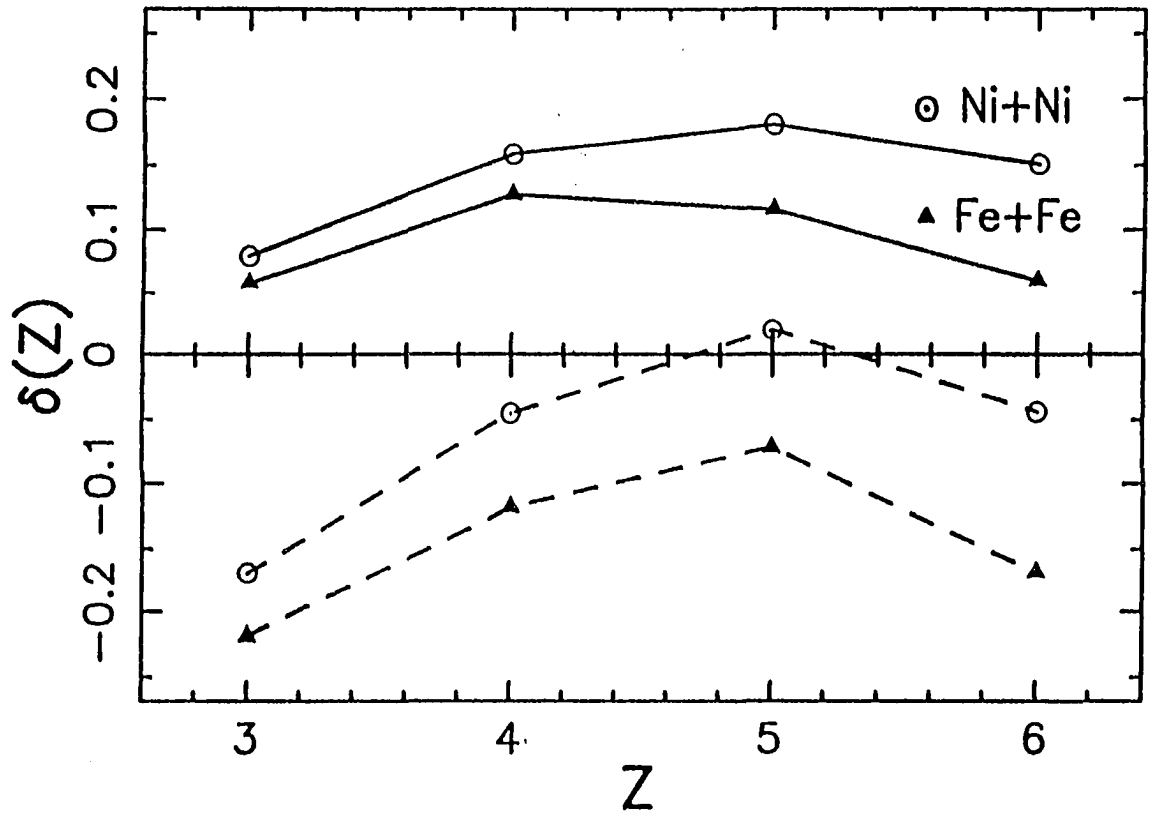


Figure 32: Excess of even- $Z$  over odd- $Z$  fragments as a function of  $Z$  shown by  $\delta(Z)$  as defined in Eq. (4.1). Solid lines are full calculations, case 4). Dashed lines are for bound states only, case 3).

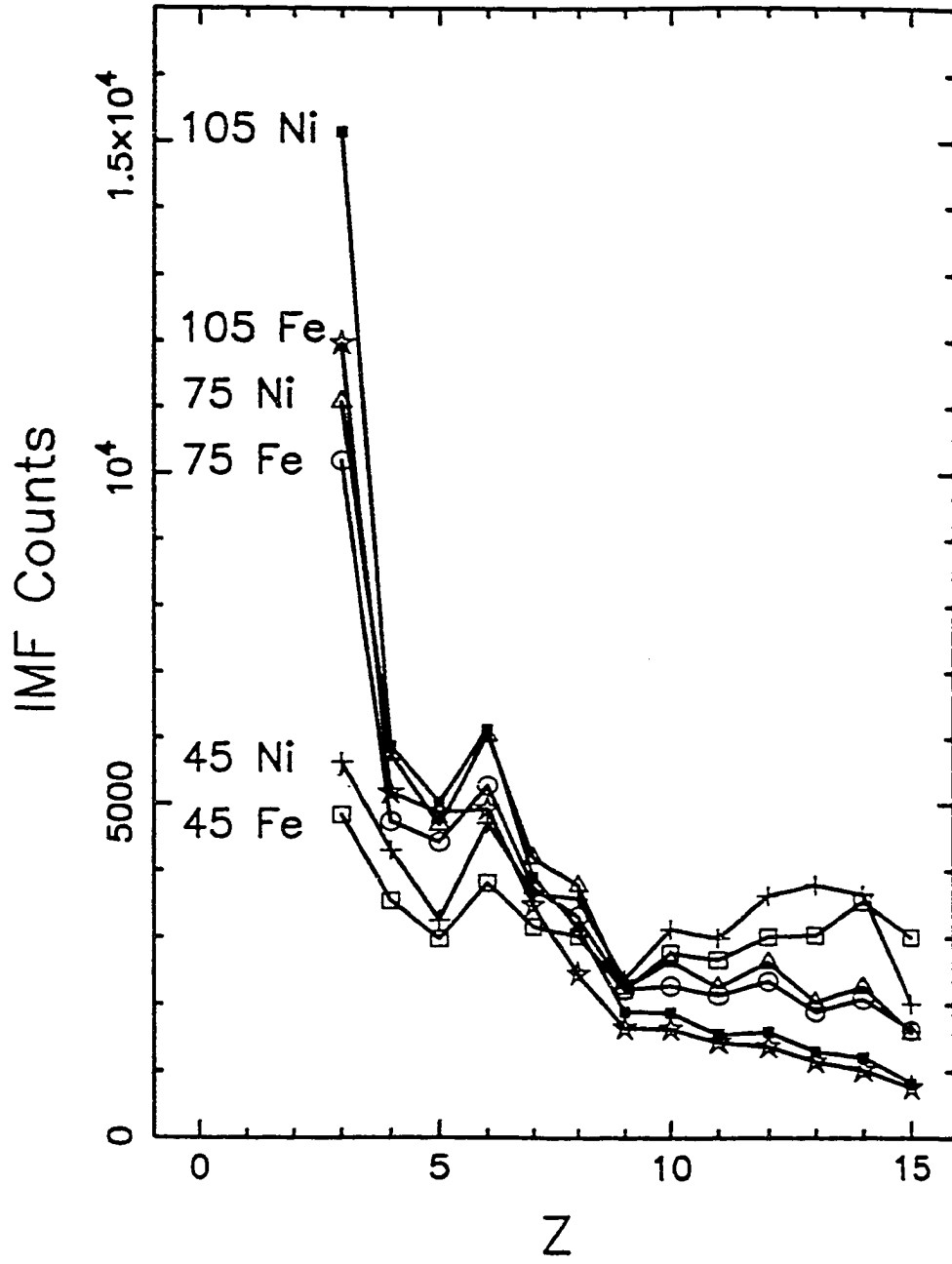


Figure 33: Odd-even effect at  $^{58}\text{Ni}+^{58}\text{Ni}$  and  $^{58}\text{Fe}+^{58}\text{Fe}$  for 45, 75, 105 A MeV.

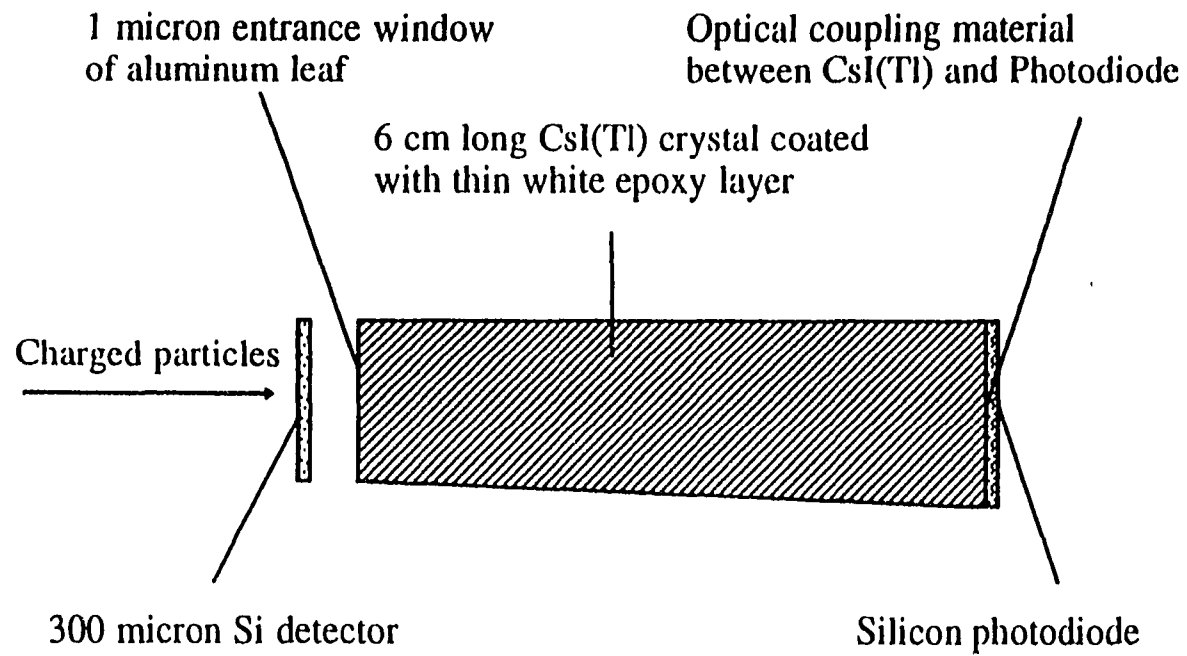


Figure 34: Individual  $\Delta E$ -E detector telescope.

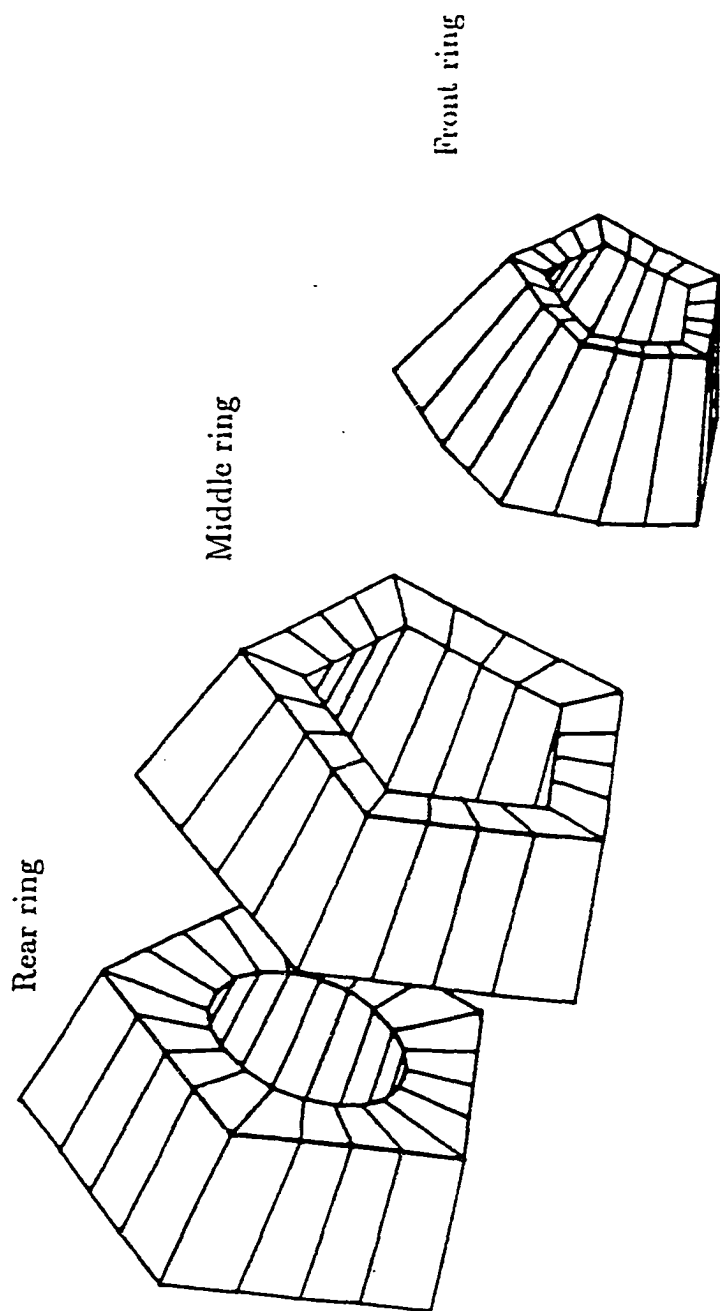


Figure 35: Arrangement of the three rings, each consisting of 20  $\text{CsI}(\text{I})$  crystals. They are front, middle and rear rings of  $\text{CsI}(\text{I})$  crystals.

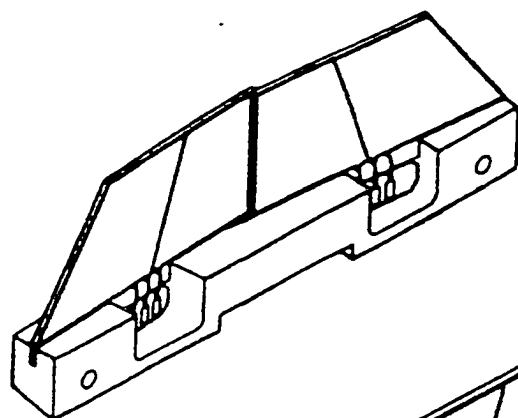
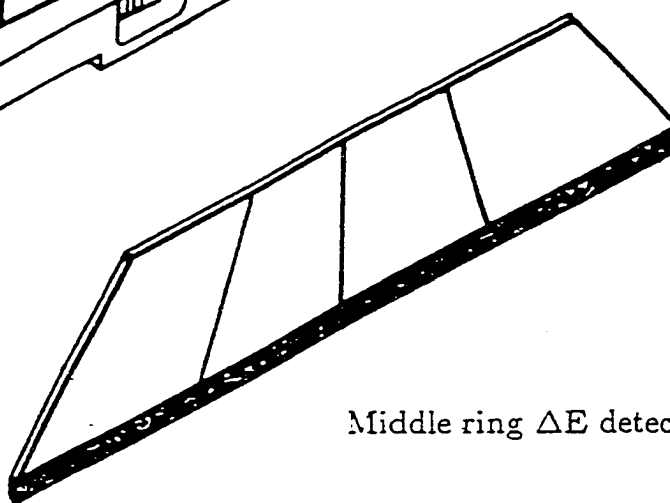
Front ring  $\Delta E$  detectorMiddle ring  $\Delta E$  detector

Figure 36: Front ring and middle ring  $\Delta E$  detectors. The arrangement of two, two-segment detectors in the mount for one side of the ring closest to the target is shown at the upper left. At the lower right, the outline of a four-segment detector for one side the middle ring is shown. The dark strip at the bottom of the detector is an extension of the guard ring structure which will be used to attach the detector to its mount.

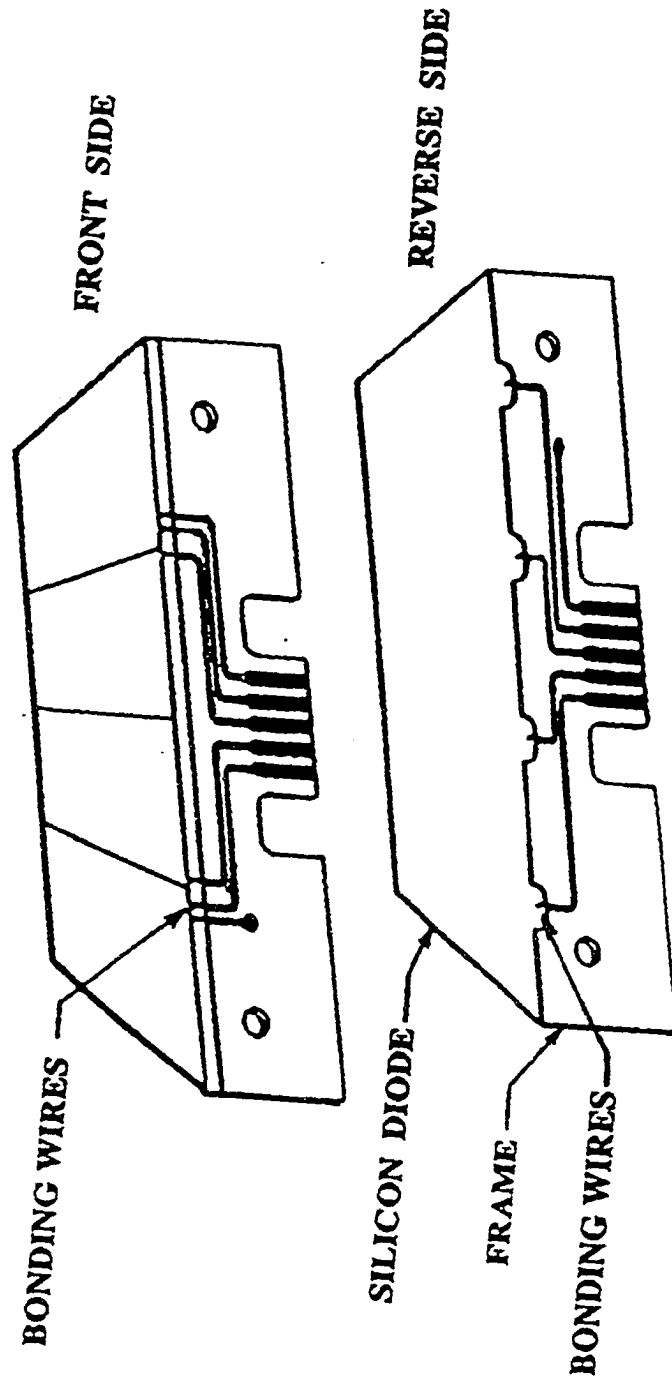


Figure 37: Middle ring  $\Delta E$  detectors showing wire connections.

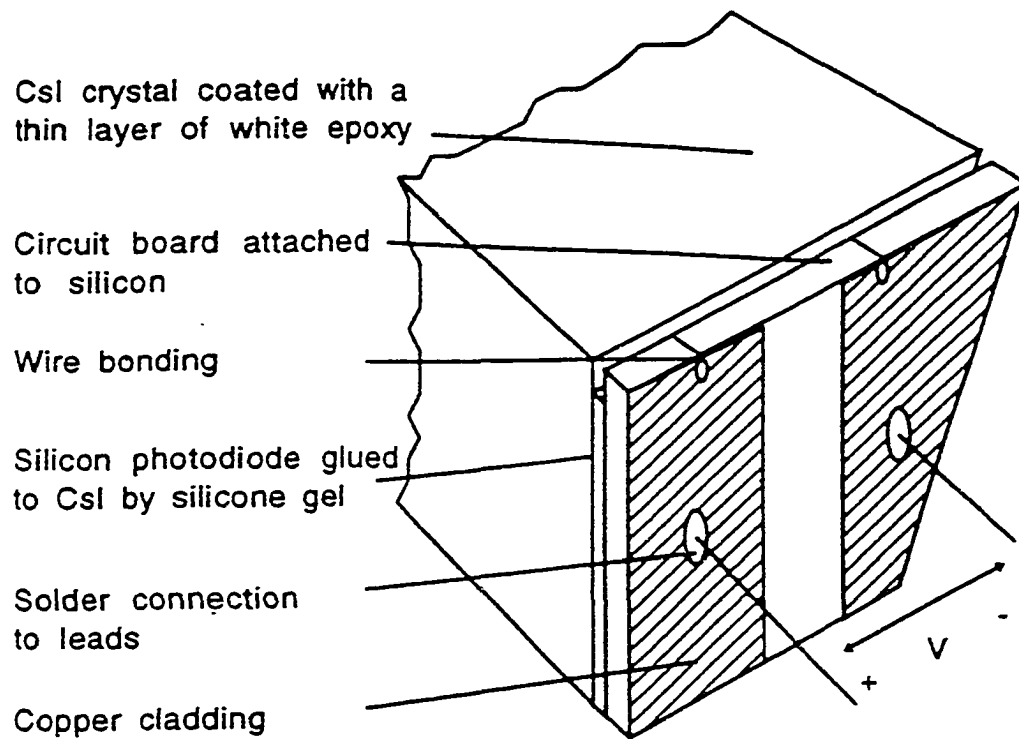


Figure 38: Diagram of attachment between photodiode and CsI(Tl). More than 90% of backside area of CsI(Tl) is covered by the photodiode.

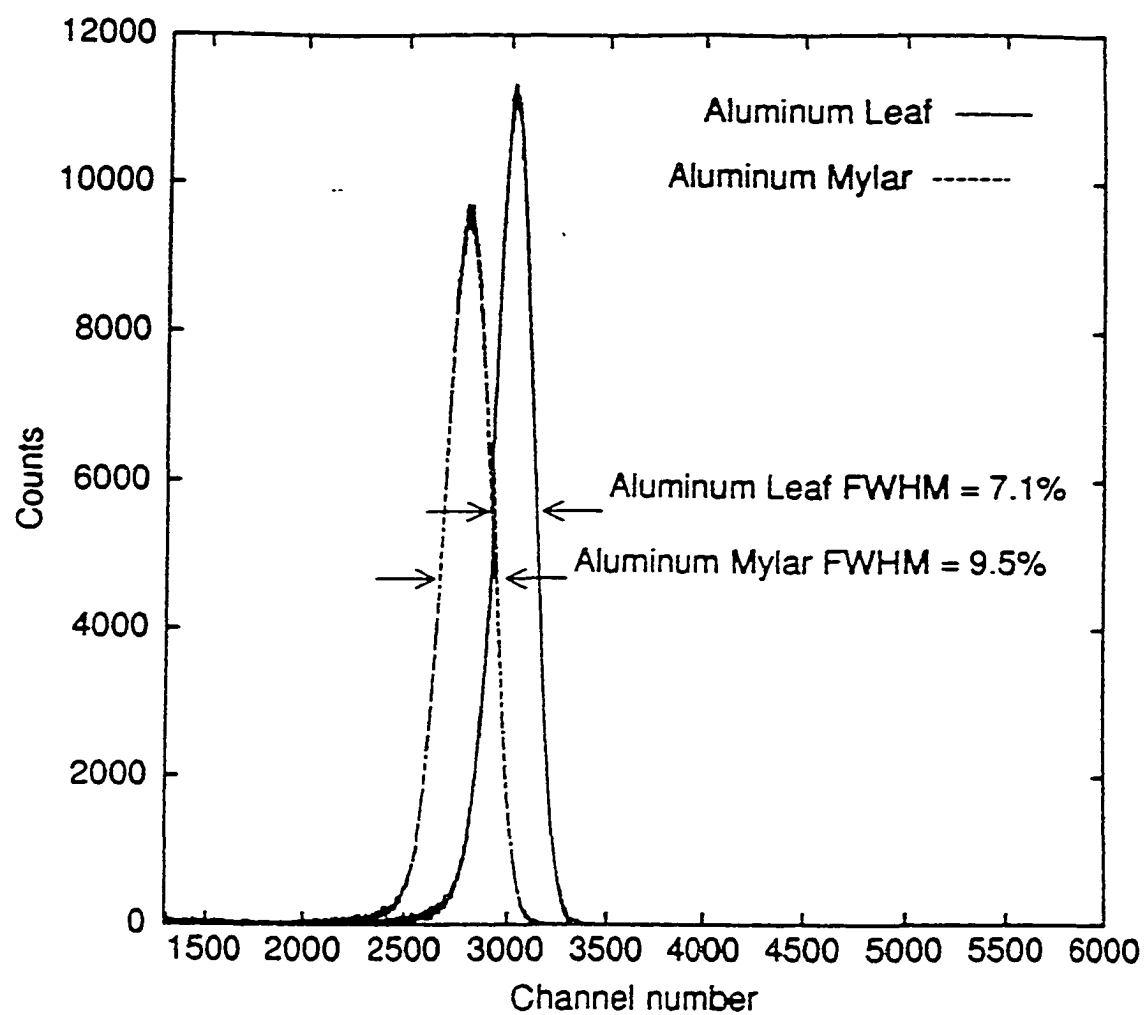


Figure 39:  $^{241}\text{Am}$   $\alpha$ -particle spectra from CsI(Tl) with entrance windows of aluminized Mylar and aluminum leaf. Aluminum leaf gives better energy resolution.

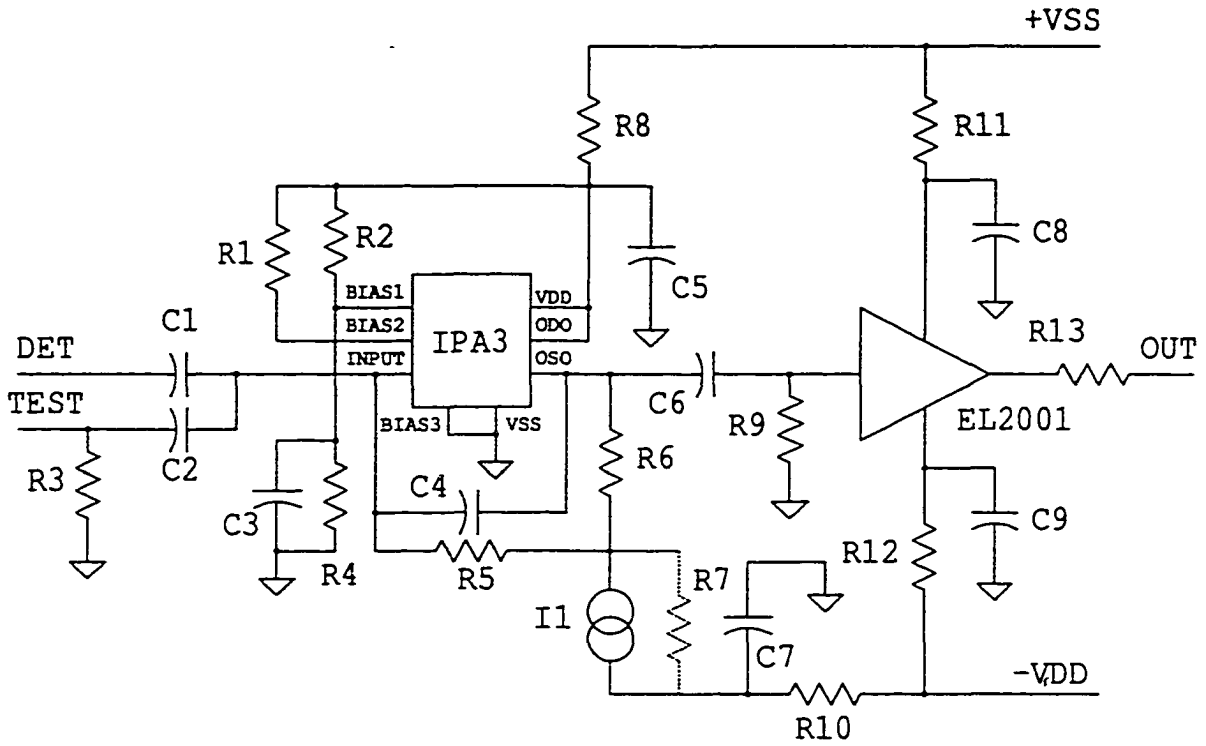


Figure 40: Schematic of the preamplifier.

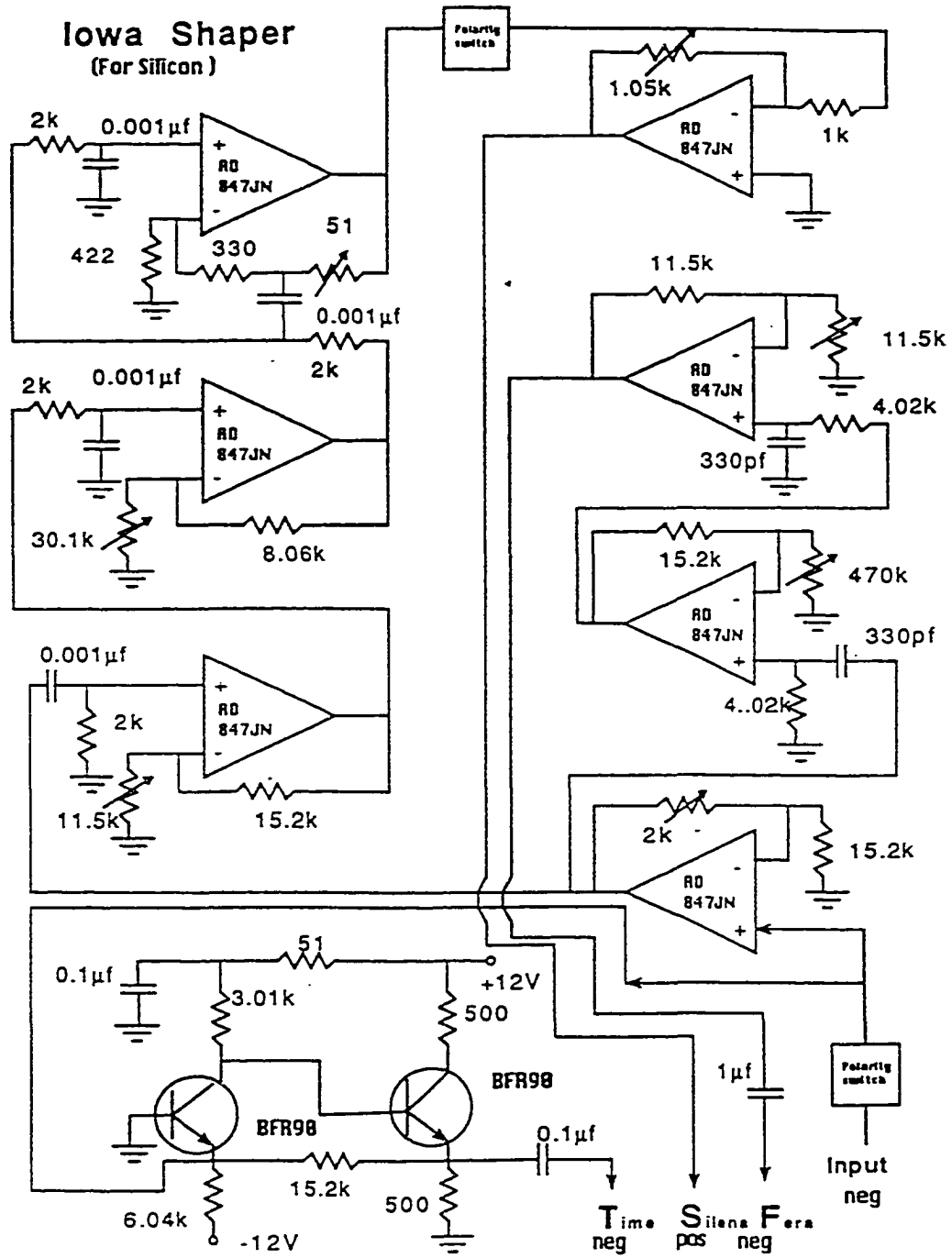


Figure 41: Schematic of the shaping amplifier.



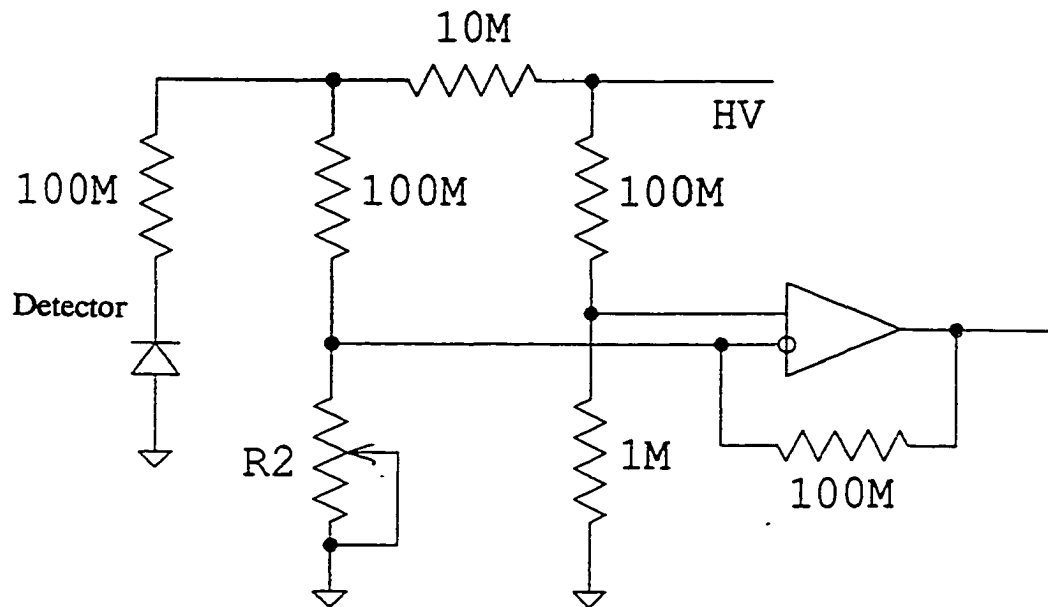


Figure 43: Schematic of the linear current to voltage converter circuit used in the power supply.



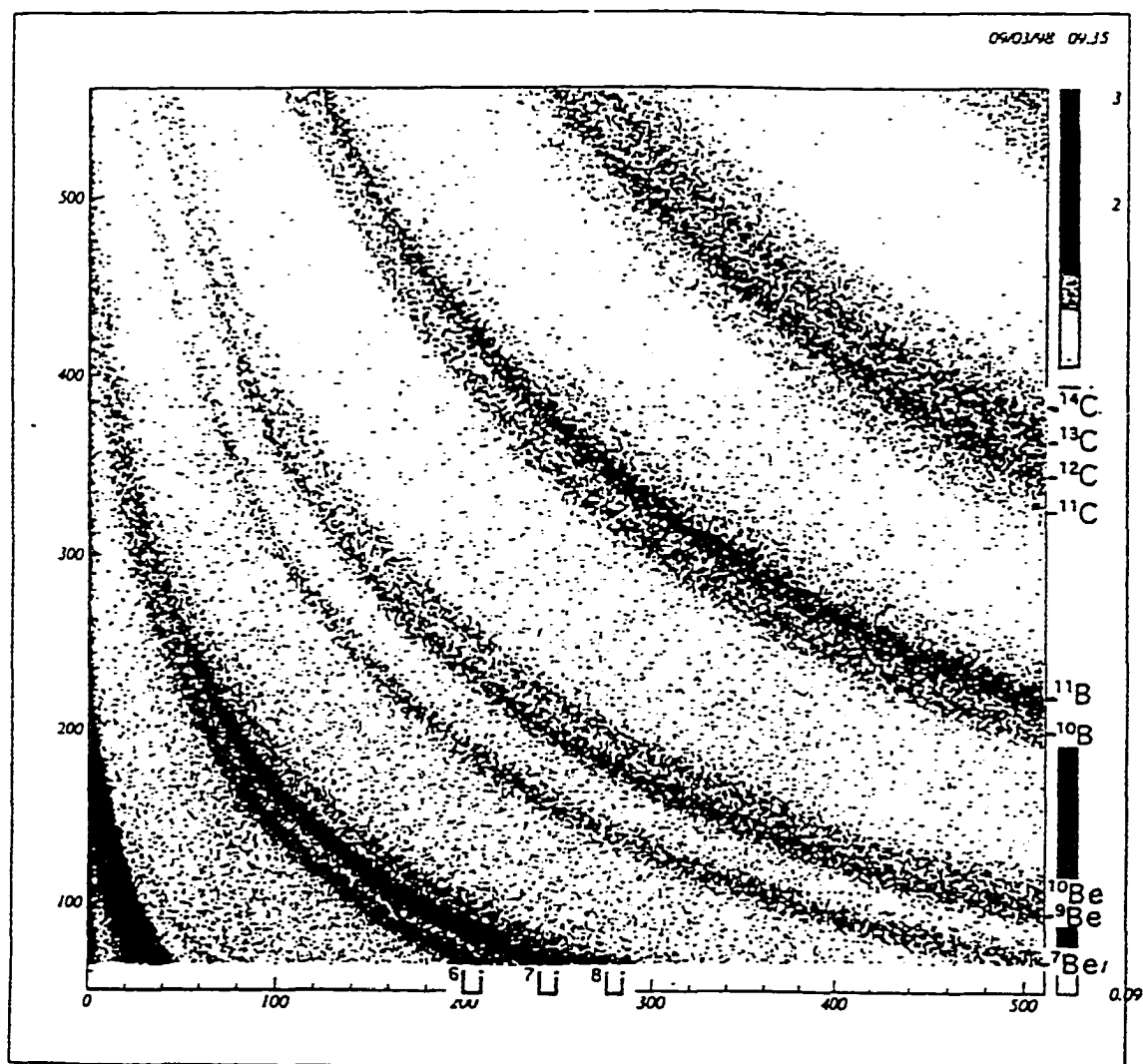


Figure 45: Z-lines obtained from the experiment of  $^{58}\text{Fe}(^{58}\text{Ni}) + ^{58}\text{Fe}(^{58}\text{Ni})$  from 5 MeV/nucleon to 105 MeV/nucleon in March 1998. Vertical axis is  $\Delta E$  and horizontal axis is  $E$ . The figure shows some of the isotope resolution. The set of three curves near the middle is  $^{7,9,10}\text{Be}$ .

## REFERENCES

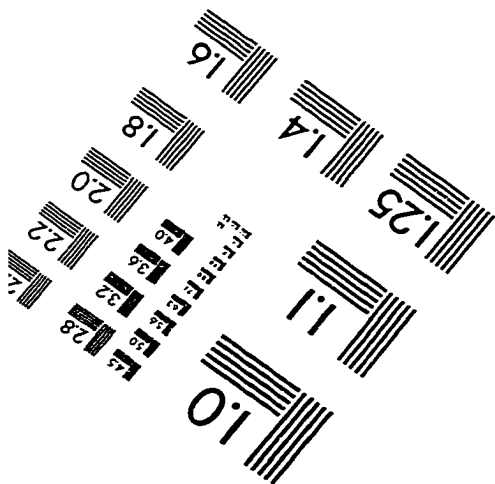
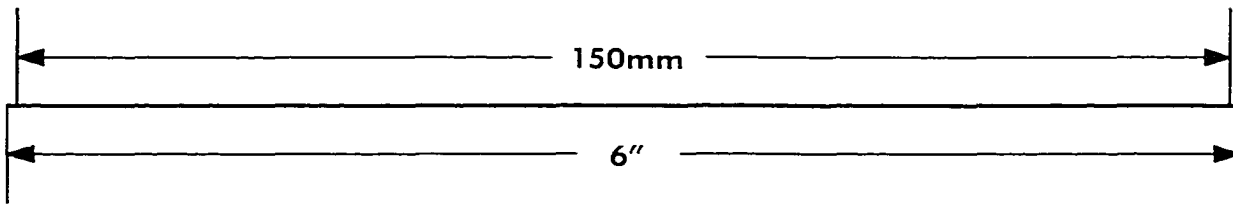
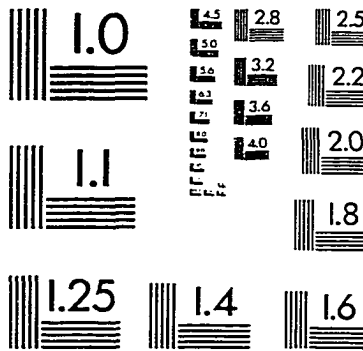
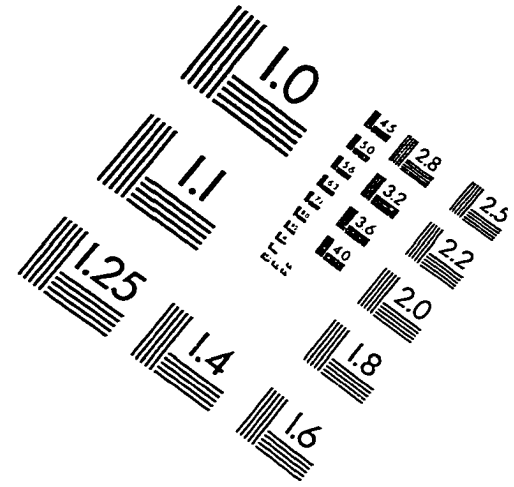
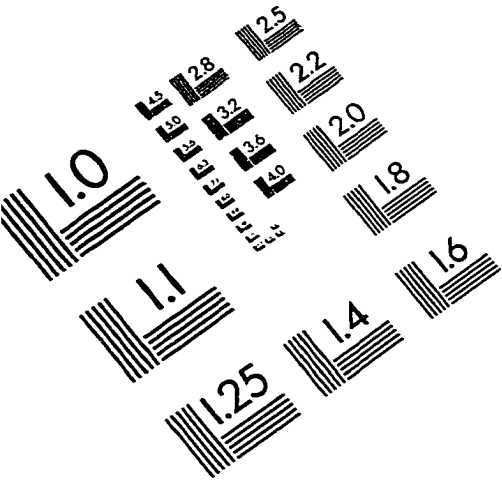
- [1] K.S. Krane, *Introductory Nuclear Physics* (New York: Wiley, 1988), p.388.
- [2] R. Pak, W. Benenson, O. Bjarki, J.A. Brown, S.A. Hannuschke, R.A. Lacey, Bao-An Li, A. Nadasen, E. Norbeck, P. Pogodin, D.E. Russ, M. Steiner, N.T.B. Stone, A.M. Vander Molen, G.D. Westfall, L.B. Yang, and S.J. Yennello, *Phys. Rev. Lett.* **78**, 1022 (1997).
- [3] R. Pak, Bao-An Li, W. Benenson, O. Bjarki, J.A. Brown, S.A. Hannuschke, R.A. Lacey, D.J. Magestro, A. Nadasen, E. Norbeck, D.E. Russ, M. Steiner, N.T.B. Stone, A.M. Vander Molen, G.D. Westfall, L.B. Yang, and S.J. Yennello, *Phys. Rev. Lett.* **78**, 1026 (1997).
- [4] E. Ramakrishnan, H. Johnston, F. Gimeno-Nogues, D. J. Rowland, R. Laforest, Y-W. Lui, S. Ferro, S. Vasal, and S. J. Yennello, *Phys. Rev. C* **57**, 1803 (1998)
- [5] G. Kortemeyer, W. Bauer, G.J. Kunde, *Phys. Rev. C* **55**, 2730 (1997).
- [6] J. F. Dempsey *et al.*, *Phys. Rev. C* **54**, 1710 (1996).
- [7] G.J. Kunde *et al.*, *Phys. Rev. Lett.* **77**, 2897 (1996).
- [8] E. Norbeck, Q.Z. Luo, Y.W. Cheng, P. Pogodin, F.D. Ingram, *Nucl. Phys. A* **607**, 105 (1996).
- [9] W. Bauer, *Prog. Part. Nucl. Phys.* **30**, 45 (1993); G.F. Bertsch and S. Das Gupta, *Phys. Rep.* **160**, 190 (1988), and references therein.
- [10] M. Colonna, G.F. Burgio, P. Chomaz, M. Di Toro and J. Randrup, *Phys. Rev. C* **47**, 1395 (1993).
- [11] L.G. Sobotka, *Phys. Rev. C* **50** R1272 (1994).
- [12] L.G. Moretto and G. J. Wozniack, *Annu. Rev. Nucl. Part. Sci.* **43**, 123 (1993).
- [13] Bao-An Li, C. M. Ko, and W. Bauer, *Int. J. Phys. E* **7**, 1 (1998).
- [14] S.J. Yennello *et al.*, *Phys. Lett. B* **321**, 15 (1994).
- [15] R. Wada *et al.*, *Phys. Rev. Lett.* **58**, 1829 (1987).
- [16] F. Deak, A. Kiss, Z. Seres, A. Galonsky, and L. Heilbronn, *Phys. Rev. C* **43**, 2432 (1991).

- [17] J. Brazychczyk, D.S. Bracken, K. Kwiatkowski, K. B. Morley, E. Renshaw, and V. E. Viola, *Phys. Rev. C* **47**, 1553 (1993).
- [18] H. Johnston *et al.*, *Phys. Lett. B* **371**, 186 (1996); *Phys. Rev. C* **56**, 1972 (1997).
- [19] L. G. Sobotka, *Phys. Rev. C* **50**, R1272 (1994).
- [20] J. Aichelin, GPeilert, A. Bohnet, A. Rosenhauer, H. Stocker, and W. Greiner, *Phys. Rev. C* **37**, 2451 (1988); J. Aichelin, *Phys. Rep.* **202**, 233 (1991).
- [21] Bao-An Li and S. J. Yennello, *Phys. Rev. C* **52**, R1746 (1995).
- [22] Yun-Wu Cheng, "Formation and Condensation of Nuclear Gas", Ph.D thesis, University of Iowa, Dec. (1996).
- [23] K. Langanke, J.A. Maruhn, S.E. Koonin, *Computational Nuclear Physics 2, Nuclear Reaction*, 115, Springer-Verlag, (1992).
- [24] W. Bauer, D. R. Dean, U. Mosel, and U. Post, in *Proceedings of the 7th High Energy Heavy Ion Study*, Report No. GSI-85-10, 1984, p. 701; W. Bauer, D. R. Dean, U. Mosel and U. Post, *Phys. Lett.* **150B**, 53 (1985); W. Bauer, U. Post, D. R. Dean and U. Mosel, *Nucl. Phys.* **A452**, 699 (1986); W. Bauer, *Phys. Rev. C* **38**, 1297 (1988); W. Bauer and A. Botvina, *ibid.* **52**, R1760 (1996).
- [25] X. Campi and J. Debois, in *Proceedings of the 23rd Bormeo Conference (Ricerca Scientifica et Educatione Permanente, Milano, 1985)*, 497; T. S. Biro, J. Knoll, and J. Richert, *Nucl. Phys.* **A459**, 692 (1986); X. Campi, *J. Phys. A* **19**, L917 (1986); J. Nemeth, M. Barranco, J. Debois and C. Ngo, *Z. Phys. A* **325**, 347 (1986); J. Debois, *Nucl. Phys.* **A466**, 724 (1987); C. Cerruti, J. Debois, R. Boisgard, C. Ngo, J. Natowitz, and J. Nemeth, *ibid.* **A476**, 74 (1988); S. Das Gupta, C. Gale, and K. Haglin, *Phys. Lett. B* **302**, 372 (1993).
- [26] G.D. Westfall, J.E. Yurkon, J. Van Der Plicht, Z.M. Koenig, B.V. Jacak, R. Fox, G.M. Crawley, M.R. Maier and B.E. Hasselquist, *Nucl. Instr. Meth.* **A238**, 347 (1985).
- [27] C.R. Gruhn *et al.*, *Nucl. Instr. Meth.* **196**, 33 (1982).
- [28] A. Breskin, *Nucl. Instr. Meth.* **196**, 11 (1982).
- [29] R. Pak *et al.*, *National Superconducting Cyclotron Laboratory, Annual Report*, p.244 (1993).
- [30] W.J. Llope *et al.*, *National Superconducting Cyclotron Laboratory, Annual Report*, p.236 (1992).
- [31] N.T.B. Stone *et al.*, *National Superconducting Cyclotron Laboratory, Annual Report*, p.181 (1994).
- [32] A. Vander Molen *et al.*, *IEEE Trans. Nuc. Sci.*, **36**, 1559 (1989).

- [33] D. Stauffer, Phys. Rep. **54**, 1 (1979); J. W. Essam, Rep. Prog. Phys. **43**, 883 (1980).
- [34] A. Coniglio, H.E. Stanley, and W. Klein, Phys. Rev. Lett. **42**, 518 (1979); D.W. Hermann and D. Stauffer, Z. Phys. B **44**, 339 (1981).
- [35] J. Cugnon and D. L'Hôte, Nucl. Phys. **A397**, 519 (1983).
- [36] P. Danielewicz, G. Odyniec, Phys. Lett. **157B**, 146 (1985).
- [37] C. Cavata *et al.*, Phys. Rev. C **42**, 1760 (1990).
- [38] L. Phair *et al.*, Nucl. Phys. **A548**, 489 (1992).
- [39] B. L. Tracy, J. Chaumont, R. Klapisch, J. M. Nitschke, A. M. Poskanzer, E. Roeckl, and C. Thibault, Phys. Rev. C **5**, 222 (1972).
- [40] R. Hentzschel, H. R. Faust, H. O.Denschlag, B. D. Wilkins, and J. Gindler, Nucl. Phys. **A571**, 427 (1994).
- [41] Sl. Cavallaro *et al.*, Phys. Rev. C **57**, 731 (1998).
- [42] C. Zeitlin, L Heilbronn, J. Miller, S. E. Rademacher, T. Borak, T. R. Carter, K. A. Frankel, W. Schimmerling, and C. E. Stronach, Phys. Rev. C **56**, 388 (1997).
- [43] J. R. Cummings, W. R. Binns, T. L. Garrard, M. H. Israel, J. Klarmann, E. C. Stone, and C. J. Waddington, Phys. Rev. C **42**, 2508 (1990).
- [44] W. R. Webber, J. C. Kish, and D. A. Schrier, Phys. Rev. C **41**, 533 (1990).
- [45] C. N. Knott, *et al.*, Phys. Rev. C **53**, 347 (1996).
- [46] S. J. Yennello *et al.*, Phys. Rev. C **48**, 1092 (1993).
- [47] Al. H. Raduta and Ad. R. Raduta, Phys. Rev. C **55**, 1344 (1997).
- [48] T. Li *et al.*, Phys. Rev. Lett. **70**, 1924 (1993).
- [49] P. Pawłowski *et al.*, Phys. Rev. C **57**, 1771 (1998).
- [50] J. Reinhold, J. Friese, H. J. Körner, R. Schneider, K. Zeitehack, H. Geissel, A. Magel, G. Münzenberg and K. Sümmerer, Phys. Rev. C **58**, 247 (1998).
- [51] C. Williams *et al.*, Phys. Rev. C **55**, R2132 (1997).
- [52] G. D. Westfall *et al.*, Nucl. Instr. and Meth, **A238**, 347 (1985).
- [53] R. Pak *et al.*, Phys. Rev. Lett. **78**, 1022 (1997); R. Pak *et al.*, Phys. Rev. Lett. **78**, 1026 (1997).

- [54] S. Steinhäuser *et al.*, Nucl. Phys. **A634**, 89 (1998).
- [55] W.A.Friedman, Phys. Rev. C **42**, 667 (1990).
- [56] E. Norbeck, L.B. Yang, P. Pogodin, D. Swan, Nucl. Instr. and Meth, **A360**, 642 (1995).
- [57] L.B. Yang, M.S. Thesis, Department of Physics, University of Iowa, May, (1995).
- [58] E. Norbeck, T.P. Dubbs, and L.G. Sobotka, Nucl. Instr. and Meth, **A262**, 546 (1987).
- [59] P. Horowitz, *The Art of Electronics* (Cambridge University Press, 1989), p.272.
- [60] P.W. Nicholson, *Nuclear Electronics* (New York: Wiley, 1974), p.140.

# IMAGE EVALUATION TEST TARGET (QA-3)



APPLIED IMAGE, Inc  
1653 East Main Street  
Rochester, NY 14609 USA  
Phone: 716/482-0300  
Fax: 716/288-5989

© 1993, Applied Image, Inc., All Rights Reserved

